UNIVERSITÀ DEGLI STUDI DI PALERMO

Dottorato di Ricerca in Energia e Tecnologie dell'Informazione
Dipartimento di Energia, Ingegneria dell'Informazione e Modelli Matematici
S.S.D.: ING-IND/31

Modelling of Pulsed Electro Acoustic Method for Space Charge Detection on Single and Multilayer Dielectrics

STUDENTE
ING. ANTONINO IMBURGIA

COORDINATORE
PROF. MAURIZIO CELLURA

TUTOR
PROF.SSA ELEONORA RIVA SANSEVERINO

CO-TUTOR
PROF. PIETRO ROMANO

TUTOR INDUSTRIALE
ING. ROBERTO CANDELA

CICLO: XXX
ANNO DI CONSEGUIMENTO DEL TITOLO: 2018

PRYSMIAN
CABLES & SYSTEMS

A Pietro

Preface

This industrial Ph.D. thesis was developed within the framework of the research project proposed and financially supported by Prysmian S.p.A..

The project was focused on the study of the PEA method for space charge measurement in dielectric materials employed for HVDC cables.

The research activity was mainly developed at the L.E.PR.E. laboratory of the Department of Energy, Information Engineering and Mathematical models, DEIM, of the University of Palermo, in which a great experience has been acquired in the use of the PEA cell for flat specimens and its related acquisition, calibration and deconvolution software.

During PhD research activity, for almost six months, the research has been carried out at the University of Southampton (UK), under the prestigious supervision of Prof. George Chen, which is one of the most world experts in the field of space charge measurements.

After the acquired experience on space charge measurements in flat samples, the PEA cell for cable specimens has been also studied and measurements over mini cables and full-size cables have been performed within the Prysmian HV laboratory, in Milan.

Finally, a further experience of two weeks has been carried out in the HV laboratory of the University of Technology, in Toyohashi, Japan. In that occasion, a further study over the PEA cell for cable specimens, combined with experimental tests, has been carried out, under the supervision of Prof. Naohiro Hozumi.

Table of contents

3. Modeling of the PEA cell 55

4. Simulation of the PEA cell 87

Introduction

In the last decades, the High Voltage Direct Current (HVDC) transmission has been more and more widely used, thanks to the advantages provided by the Direct Current (DC) over the Alternating Current (AC). In particular, by using HDVC systems, the costs of transmission are less, there is no reactive power flow and skin effect, while audible noise is reduced, etc….

As regard the cables used in HVDC systems, initially, mass-impregnated (MI) and oil-filled (OF) cables were employed. However, with these cables there were several disadvantages, e.g. the limited operating temperature for the MI cable and the limited length for the OF cable. Because in the High Voltage Alternating Current (HVAC) systems, the cross-linked polyethylene (XLPE) cables have had a great success, thanks to the advantages of insulating material (e.g. high dielectric strength, electrical resistivity and good mechanical and thermal properties), the cables industry worldwide has begun to use XLPE also for HVDC cables. In this way, the problems related to the use of MI and OF cables were overcome. Unfortunately the use of XLPE, as insulating material in HVDC systems, promotes the space charge accumulation phenomenon, which means a trapped of electrons or ions in the dielectric material bulk. The main effect of this phenomenon is the distortion of the original Laplacian electric field distribution, which could cause extremely high local electric fields. This in turn may cause the insulating material to degrade and this fact can lead to electrical breakdowns and electrostatic discharges.

Based on the above, during the years, the space charge phenomenon started to be widely studied from researchers all over the world and thus different space charge measurements techniques have been developed. In particular, the Pulsed Electro Acoustic (PEA) method has had great success, thanks to the ease of implementation and robustness of the measuring cell.

This technique, based on propagation of acoustic waves, is subjected to reflections phenomenon. In particular, if some components of the PEA cell are not properly sized, the PEA cell output signal may be affected by false signals due to wave reflections. In this case, the output charge profile is not clear and therefore the real accumulated charge may be mis-interpreted. For these reasons, in this thesis, a model able to simulate the generation, propagation and reflection of acoustic waves within the PEA cell has been developed in Matlab-Simulink environment.

Considering that an acoustic wave is described by its pressure and velocity, because of the analogies voltage-force (or pressure) and current-velocity, it has been possible to employ electrical quantities in order to simulate the behavior of acoustic waves. Furthermore, each PEA cell component can be described by electrical parameters and therefore the behavior of acoustic waves within the PEA cell has been simulated as the behavior of voltage and current waves in electrical lossy transmission lines.

In this work, simulations have been carried out for different cases. In particular, the case in which the PEA cell is properly sized and other cases in which the thickness of the ground electrode and absorber are incorrectly sized have been considered.

In the first case, the PEA cell output signal is characterized by the peaks due to the accumulated surface charges. For the other two cases, the simulation results show that the reflected wave within ground electrode and absorber anticipate the acoustic wave due to the main signal. Therefore, the output charge profile is affected by reflections.

Moreover, a further layer of dielectric material has been inserted into the model with the aim to simulate the behavior of acoustic waves within the PEA cell in case of a two layers specimen. In this case it was found that the thicknesses of both ground electrode and absorber must be greater as compared to that calculated for a single layer specimen.

The developed model, for both one and two layers specimens, has been validated by making a comparison between simulation and experimental results. As regard experimental tests, a PEA cell available at the TDHVL (Tony Davis High Voltage Laboratory) at the University of Southampton has been used, as well as the PEA cell of the LEPRE laboratory (Laboratorio di Elettrotecnica e di Prove Elettriche) at the DEIM (Department of Energy, Information engineering and Mathematical models) of the University of Palermo.

In the proposed thesis, the work has been organized as follows.

In Chapter 1, the state of the art of the space charge measurement systems, which have been developed or used in the last two decades, is reported.

In Chapter 2, the working principle of the PEA cell is widely described, as well as the theoretical analysis of the generation, transmission and reflection of acoustic waves within the PEA cell. In the final part of this chapter, the basis of the PEA cell output signal process, such as deconvolution and calibration techniques, is given as well.

In Chapter 3, the developed model and all the related equations are reported and described, as well as, the Leach’s impedance-type transducer model used to simulate the piezoelectric sensor. In addition, an example of dynamic simulation, useful to better understand the waves behavior within the PEA cell, is also given.

In Chapter 4, simulations are made for a single layer specimen and the model validation is carried out by comparing simulated and experimental results.

In Chapter 5, instead, the multi-layers specimen modeling issue is treated. In particular, the Maxwell-Wagner theory, useful to calculate the interfacial charge in dielectric/dielectric interface, is described. Also in this case, the study of waves behavior within the PEA cell, and thus the relationships useful to properly size the components, are provided.

Finally, in Chapters 6, the recommendations are given, while in Chapter 7, the overall conclusions of the thesis are drawn.

Chapter 1

Review of space charge measurement systems

This chapter deals the state of the art of space charge measurement techniques and it is based on the works of the author et al. entitled “*Review of Acoustic Methods for Space Charge Measurement*” [1], “*Review of Space Charge Measurement Systems: Acoustic, Thermal and Optical Methods*” [2], and “*Review of Thermal Methods for Space Charge Measurement*” [3].

The first measurement of space charge distributions in dielectric materials goes back more than fifteen years ago and was highly destructive as it was necessary to cut the material mechanically and then visualize the trapped internal charge.

In the following years the research has focused in the development of non-destructive methods. In particular, the techniques were divided into three main groups in relation to the physical principle on which they are based, such as acoustic, thermal and optical methods. Of these groups, methods based on acoustic and the thermal phenomena have been largely used also in industrial applications, while, the methods based on optical phenomena haven not had much success due to the complexity of the measuring cell. For these reasons, a more detailed description will be given for acoustic and thermal methods, in particular for the Pulsed Electro Acoustic (PEA) technique and for the Thermal Step Method (TSM) belonging to the groups of acoustic and thermal methods, respectively. These two techniques have had the greater success for measures of space charge on a flat specimens but also on a full-size cables. During the years, their measuring cell has been modified in order to make measurements on samples with different shapes and sizes.

In the following sections will be described the main space charge measurement methods belonging to the three groups above mentioned, which have been developed or used in the last two decades. For each of them, the principles of operation, the different configurations, the main applications, the thicknesses analyzed and the spatial resolution will be also reported and discussed.

1.1. Thermal group

The main methods belonging to this group are the Thermal Pulse Method (TPM), the Thermal Step Method (TSM) and the Laser Intensity Modulation Method (LIMM). The main difference between these categories consists in the modality of application of the thermal gradient to the sample. More in detail, this gradient can either be a thermal pulse from a flash of light or a thermal step by using a thermal diffuser or a sinusoidal modulated heating by means of a laser beam. In the TPM case, the output signal is a voltage response related to the charge and polarization distribution and to the temperature change.

In the TSM and LIMM methods, instead, the output signal is a current response. In the first method, the current is connected to the electric field and to the thermal step. In the second method, this current is related to the temperature, characteristics of material, and accumulated space charge [4].

These methods have in common a satisfactory value of spatial resolution, which can be further improved through greater accuracy in measurements over the surface and internal temperature of the sample [5,6].

1.1.1. The Thermal Pulse Method

The TPM has been introduced in 1976 by Collins [7, 8] and its principle of operation is reported in Figure 1.1. This method is based on a thermal pulse generated by a flash of light (8 μs of duration), which acts on one of the double-metalized surfaces of the sample. A thermal transient is then generated over the sample, and an electrical signal carrying information on the space charge distribution inside the sample itself is taken as output.

The system response *ΔV(t)* depends on the distribution of space charge *ρ(x)* and polarization *P(x)*. In addition, as shown in equation 1.1, *ΔV(t)* depends also on the characteristic parameters of the insulating material, such as the coefficient of thermal expansion α_x, the dielectric constant ε_r, its temperature coefficient α_ε and, finally, the coefficient of permanent polarization α_p.

$$\Delta V(t) = \frac{1}{\varepsilon_r \varepsilon_0} \int_0^d \left\{ \left[A\,\rho(x) - B\,\frac{dP(x)}{dx} \right] \int_0^x \Delta T(x')dx' \right\} dx \qquad (1.1)$$

Where $A = \alpha_x - \alpha_\varepsilon$, $B = \alpha_p - \alpha_x - \alpha_\varepsilon$ and *d* is the sample thickness.

However, the TPM has not been widely used because of the difficult interpretation of the signal for the determination of the real distribution of space charge. In order to solve this issue, several signal processing techniques have been developed and presented in literature, from Collins [8] through Mopsik [9] and Zheng [10].

The TPM was mainly adopted in the past years, for example, to measure the space charge distribution in a silicon dioxide of 1 μm thickness by using a short laser pulse (70 ps) [11]. In recent years, instead, the method was used in order to tested a metal oxide-semiconductor

(MOS) structure with thickness of several hundreds of nanometers [12], but also to perform 2D and 3D measurements [13,14].

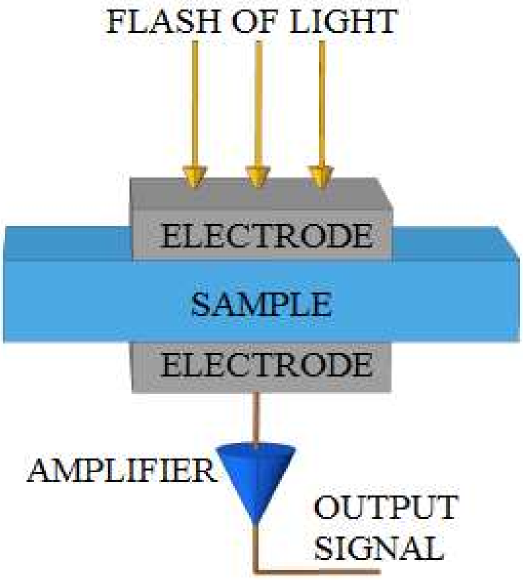

Figure 1.1. *Working principle of the TPM technique.*

1.1.2. The Thermal Step Method

The thermal step method has been conceived in 1988 by Toureille [15] and its principle of operation is based on the application of a thermal step to the ends of the related sample in order to measure the current response due to the thermal expansion of the sample itself. More in detail, a thermal diffuser provides a heat step, which creates a thermal wave. This wave will diffuse through the thickness of the dielectric, which determines either an expansion or a contraction of the material, a variation of the insulation permittivity and causing a temporary and reversible displacement of the space charge located within the sample. This displacement will be, then, reflected on the electrodes, determining a variation of the induced charge and, consequently, a current between the electrodes. The value of this current *I(t)* read by a pico-ammeter (pA) is related to the distribution of both the electric field and the space charge [16]. This setup is called TSM in short-circuit condition, and the scheme is shown in Figure 1.2.
The expression of *I(t)* is reported in the following equation:

$$I(t) = -\alpha C \int_0^d E(x) \frac{\partial \Delta T(x,t)}{\partial t} dx \tag{1.2}$$

where $\alpha = \alpha_x - \alpha_\varepsilon$ (in which α_x is the coefficient of thermal expansion and α_ε is the temperature coefficient of the insulating material).While, the term C is the capacitance of the sample before the application of the thermal step, d is the sample thickness, $E(x)$ is the electric field at the abscissa x and ΔT the temperature step. Once $E(x)$ and the dielectric constant of the material ε are known, from Poisson's equation (see equation (1.3)) the distribution of the space charge can be determined.

For this purpose, the adoption of the deconvolution technique is needed, e.g., the "Fourier series" or the "process of successive derivatives" that allows the reduction of the deconvolution calculation time or the "technique of the inverse matrix" that reduces not only the calculation time but also the related error [17].

$$\rho = \varepsilon \frac{\partial E(x)}{\partial x} \tag{1.3}$$

Initially, the TSM has been applied for 2-20 mm insulation thicknesses with 150 μm of resolution. However, by means of a faster heating, thin insulations in the range of 10-100 μm with a resolution in the order of tenths of a micrometer can be investigated [18].

The TSM can be also applied to the field of micro and nano electronics. However, this method can be destructive when the investigation concerns layers of material with thicknesses below micrometers [19]. In order to overcome this problem, the thermal step technique is joined to the capacitance-voltage technique, which is accurately proposed in [20]. More in particular, Dagher et al. [21] brought the resolution to values between 22 nm (in polymeric materials) and 50 nm (in silicon dioxide) by using an optical instrumentation with laser pulse of the order of femtoseconds. The signal to noise ratio was low, so the method needed further investigations.

An important work has been also carried out by Stancu et al.,[22] which analyses the space charge behavior in a low density polyethylene (LDPE) disks of 0.5 mm thickness, with and without water trees. Experimental results have shown that the presence of water trees increases the accumulation of the space charges.

The proposed method has several significant advantages with respect to other thermal techniques. This is due to the nondestructive nature of the TSM, which is achieved by choosing the value of the maximum temperature imposed by the thermal step equal to the room temperature.

A drawback of the proposed technique is related to the thermal contact between the radiator and the sample, which could cause, if imperfect, temperature fluctuations and, therefore, attenuation or delay of the current response [23].

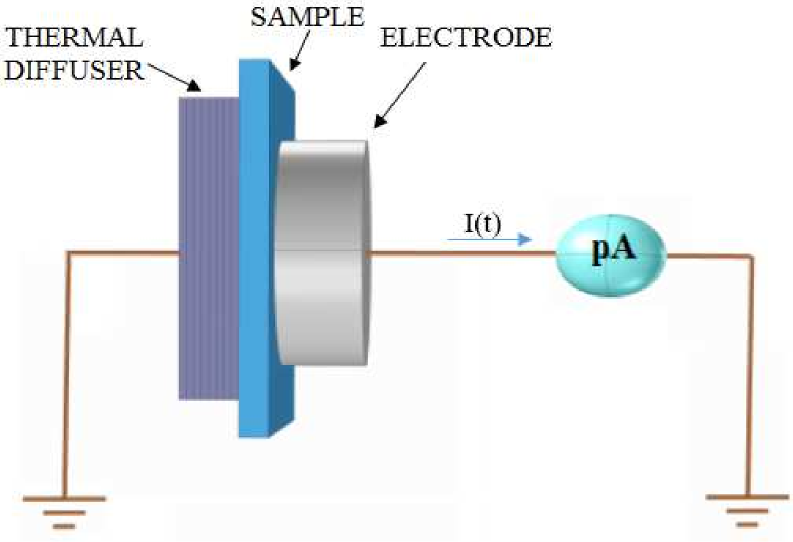

__Figure 1.2.__ Working principle of the TSM in short-circuit condition.

1.1.3. The Thermal Step Method Under Applied DC Field

In year 2000 Agnel et al. developed a work finalized to perform space charge measurements under the application of a DC electric field [24]. However, the scheme of Figure 1.2 was not completely suitable for the measurements under electric field, because of the use of the current amplifier. In detail, the current amplifier must not be in contact with the high voltage, and also if a setup with the current amplifier placed between the sample (submitted to high voltage) and ground is used, the conduction and the polarization currents are likely to mask the thermal step current.

To overcome this challenge, a compensation sample (with the same dimensions of the sample under test) in front of the specimen was placed, obtaining the so called "double capacitor" configuration, which is represented in Figure 1.3 [25].

In order to measure space charge distribution, the testing procedure requires two steps: first, the high voltage is applied to the middle electrode, thus the two sample constitute two identical capacitances placed in parallel with respect to the high voltage source. In this way the same amount of charge is accumulated on both samples, while the pA is short circuited. Second, during the measurement, the high voltage generator is disconnected in order to avoid the carriage of charges through the electrodes, compromising the correct measurement.

The thermal step current is then measured by exciting thermally the specimen under test, while the pA is connected to the compensation sample. In this way the two samples are in series with each other and with the pA, therefore the short-circuit condition (as in the general case of the TSM described in the previous paragraph) are fulfilled.

The space charge, in this case, can be assessed in the same manner described for the classic TSM.

The expression of the thermal step current *I(t)* is given by:

$$I(t) = -\alpha C_2 \int_0^d E(x) \frac{\partial \Delta T(x,t)}{\partial t} dx \tag{1.4}$$

where C_2 is the capacitance seen by the current amplifier. In particular, during the measurement, in which the two samples are in series, the value assumed by C_2 is equal to $C/2$.

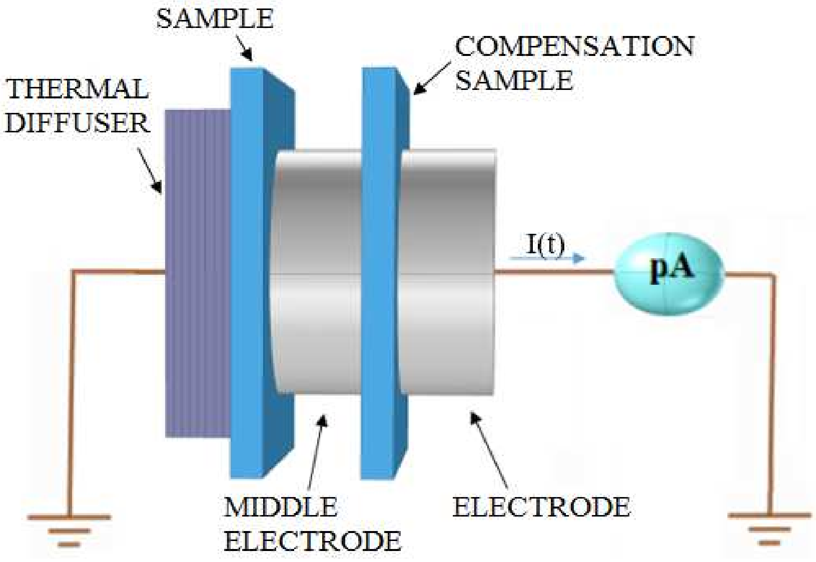

Figure 1.3. *Working principle of the TSM with double capacitor.*

In 2014, Laurentie et al. proposed the "contactless" configuration in order to measure both the space charge inside the dielectric and the surface charge. In this configuration the upper face of the specimen is isolated from the upper electrode through a thin layer of air, avoiding disturbances. The diagram and explanation of the method are provided in [26]. The spatial resolution, which decreases when the distance between the space charge inside the sample and the electrode in contact with the thermal diffuser increases, is comprised between 50 and 100 µm for a polyethylene terephthalate (PET) sample of thickness of 100 µm.

In order to evaluate the influence of the electric field gradient and temperature in the charges distribution, space charge profiles were carried out in 0.5 mm of a XLPE sample, under different DC electrical stress (from 2 to 60 kV/mm) and temperatures (from 70 to 90°C). The obtained results have shown that the space charge accumulation grows with the increase of both electric field and temperature [27].

1.1.4. The Thermal Step Method for cables

The thermal step method can also be applied to power cables by using two possible techniques:

- The Outer Cooling Technique, OCT.
- The Inner Heating Technique, IHT.

The principle of operation of both techniques does not differ from the TSM described in the preceding paragraphs. In this case the differences consist in the electrodes that are replaced by the core of cable and outer semicon, while the thermal diffuser is disposed around the cable under test. The test setup is shown in Figure 1.4, and the expression of the output signal *I(t)* is similar to that of the flat sample configuration (equation (1.2)), in which the integral one is extended to the inner and outer rays of the cable insulation, r_0 and r_i, respectively, as reported in the equation (1.5) [28, 29].

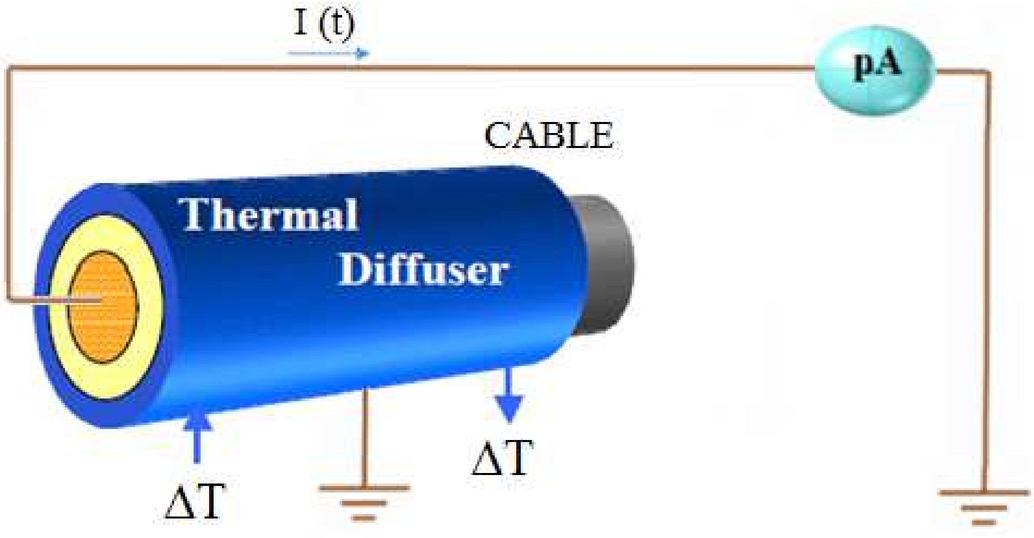

Figure 1.4. *Application of the TSM to cable sample.*

$$I(t) = -\alpha C \int_{r_0}^{r_i} E(r) \frac{\partial \Delta T(r,t)}{\partial t} dx \qquad (1.5)$$

The work in reference [29] shows how to determine the electric field and the space charge profiles. In addition, the work [30] demonstrates that the resolution of the method is in the order of millimeters and typically smaller than 20 mm. As well as for the flat specimens discussed in Paragraph 1.1.2, a similar experiment was done in order to evaluate the effect of water trees on space charge accumulation in 50 cm and 70 m long cable specimens [31]. The smaller sample has been tested by using the OCT (a thermal step of −30°C), while the longer one was studied using IHT. The presence of water trees, as for flat specimens, results in a greater accumulation of charge for both samples.

The described method has been also developed for onsite applications, by using power DC/DC converters for the control of high currents circulating in the inductor wrapped on the cable [32]. The TSM has been applied by Mazzanti et al. to the cables during both pre-qualification and type tests [33]. The same article reports the most relevant problems related to this method. A relevant challenge for this method can be identified by the significant space occupied by the measurement setup, which is also composed by an additional cable (namely “compensation cable”), identical to the cable under test and connected to its terminals. This is made in order to avoid the problems related to the current amplifier, as described in Paragraph 1.1.3.

Another problem consists in the test procedure, because before the space charges measurement the DC source must be disconnected, while the cold liquid must begin to flow. This fact involves longer times between two subsequent measurements, when compared to other techniques, such as the Pulsed Electro Acoustic (PEA) method (this method will be described later).

1.1.5. Alternative Thermal Wave Method

The Alternative Thermal Wave Method (ATWM) was developed by Reboul et al. in 2001 for measurements on thin dielectrics located in power capacitors [34]. The main difference compared to the TSM is that employed to have a better resolution using a thermal excitation over a long period of time rather than a single stimulus. As a matter of fact, the thermal excitation brought by the radiating electrode does not give sufficient resolving power for the space charge measurement in thin dielectric films (due to a high number of information lost during the beginning of the transient current). The resolving power can be improved by using a long periodic thermal excitation [35]. With this method, a resolution of a few μm is obtained, and a wide range of thicknesses from 50 μm up to 3 mm can be analyzed. The ATWM is used in order to measure the space charge profiles, while another technique, called Thermal Stimulated Discharge Current (TSDC), can be used to study the injection, transport, and trapping of charges. By considering this aspect, in [35] these two techniques have been applied simultaneously in order to carry out a complete study of space charge behavior. In 2011, the ATWM was improved in terms of accuracy by applying two simultaneous thermal waves in both surfaces of the specimen [36].

1.1.6. Laser Intensity Modulation Method

The Laser Intensity Modulation Method (LIMM) was invented by Lang and Das-Gupta during the mid-1980s [37, 38].

Generally, in the LIMM method the metalized surfaces of a specimen are heated by using a laser with modulated sinusoidal intensity in time, as shown in Figure1.5. Therefore, a non-uniform distribution of the temperature is produced along the thickness of the sample. The laser beam is absorbed by the electrode, and its sinusoidal modulation causes a sinusoidal fluctuation of the temperature in the electrode. Consequentially, a temperature wave is diffused within the sample and attenuated and delayed in phase. In this way, an unevenly distributed thermal force is displayed over the sample. Therefore, the interaction between this force and the space charge generates a sinusoidal pyroelectric current, which is amplified and subsequently processed.

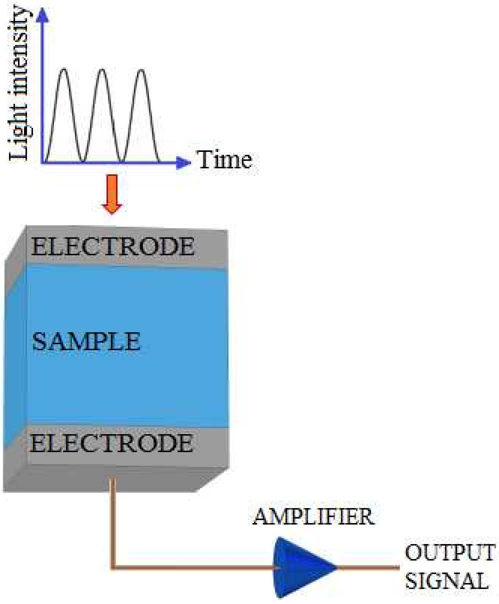

Figure 1.5. *Working principle of the LIMM technique.*

The sinusoidal pyroelectric current *I(t)* can be written by the following expression:

$$I(t) = \frac{S}{d}\int_0^x G(x)\frac{\partial \Delta T(x,t)}{\partial t}dx \tag{1.6}$$

where *T* is the temperature and *G(x)* the distribution function, while *S* and *d* are the area and the thickness of the sample, respectively.

As well as for the methods previously described, several deconvolution techniques have been developed during the years, finalized to determine both the space charge and the polarization distributions [39, 40]. In particular, in the LIMM technique the mathematical processes to follow are more complex due to an ill-posed problem with multiple solutions that resides in this method.

This technique has been applied to many application fields, from measurements in the dielectric used in spatial applications [41, 42] to measurements in XLPE specimens [40, 41], with a resolution between 1 and 2 µm.

1.1.7. Focused Laser Intensity Modulation Method

In order to carry out 3D measurements starting from the LIMM method, Marty-Dessus et al. developed the Focused Laser Intensity Modulation Method, also named Focused LIMM (FLIMM) [45]. The principle of operation has remained unchanged with respect to the LIMM technique. However, as shown in Figure 1.6, which schematically represents the test setup of this method, the three dimensional distributions of the space charge are obtained by moving the laser beam generated by the laser diode in the two directions z-y.

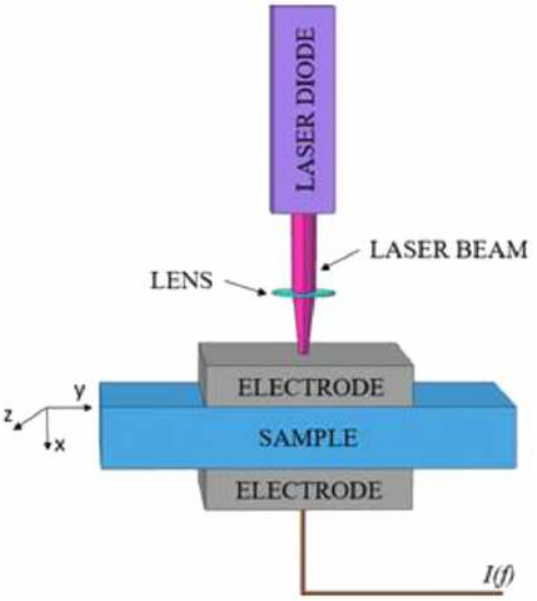

Figure 1.6. *Working principle of the FLIMM technique.*

The measure along the x-direction, which corresponds to the thickness direction, depends on the laser beam modulation frequency. The output current signal of the system, $I(f)$, is given by the following equation:

$$I(f) = \frac{A}{L} j2\pi * f \int_0^L k(x) T(x,f) dx \tag{1.7}$$

where A is the cross-sectional area of laser beam, L is the specimen thickness, T is the temperature, and k is the generalized pyroelectric coefficient.

In [46] the proposed method was compared with the TPT in order to determine the three-dimensional polarization distributions in poly (vinylidenefluoride-trifluoroethylene) (PVDF-TrFE) film. The carried out tests have shown that the TPT gives very good and fast results, while the FLIMM was characterized with a better lateral resolution.

The FLIMM technique was used for thicknesses up to µm and resolutions in the lateral direction and in the axial direction of few µm and ~1 µm, respectively [47, 48]. The range of these parameters was depending on both the amplitude of the laser beam and the mathematical method used.

Marty-Dessus and other researchers have recently modified the FLIMM method by creating an air gap between the upper measuring electrode and the related sample [49]. Their first experiment has involved the 2D and 3D cartography of the space charge carried out in polar PVDF (Polyvinylidenefluoride) and electron irradiated PTFE (Polytetrafluoroethylene) samples.

1.2. Acoustic group

The most important methods belonging to this group are the Pulsed ElectroAcoustic (PEA) method and the Pressure Wave Propagation (PWP) method. The latter includes the Piezoelectric Induced Pressure Wave Propagation method (PIPWP or Piezo-PWP) and the Laser Intensity Pressure Pulse (LIPP) method. While, the PEA method was the most widely used and changed over the years. The working principle of the different configurations of the PEA method remains the same, the mainly differences are in the measuring cells, which have been modified in order to carry out tests for flat specimen (also in 2 and 3 dimensions), for cables, in situ (Portable PEA) or for measure simultaneously both the space charges inside the dielectric and the surface charges (Open Upper Electrode).

All acoustic methods use the same physical principle based on the propagation through the sample of acoustic waves. The pressure waves are generated in different ways for different methods. Considering a single wave, it starts from the inside of the sample in the case of the PEA method, while it starts from the outside of the sample in the case of the PWP method. In each case the pressure pulse propagates as shown in Figure 1.7, in which a sample of perfect insulating material, with thickness d and relative permittivity ε_r, interposed between two metallic electrodes (A and B) is considered.

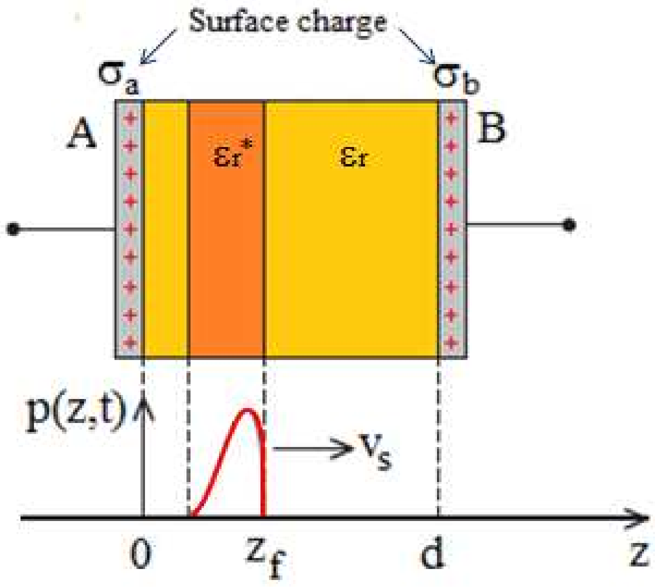

Figure 1.7. *Propagation of the pressure wave.*

The wavefront Z_f of the pressure wave, generated by the vibration of the transducer or of the charges, travels through the sample at the speed of sound v_S. The mechanical perturbation, caused by this wave of pressure, acts on the atomic structure of the material causing a compression and then the displacement of the charges trapped in its inner space and the variation of the relative permittivity ε_r. Depending on the space charge distribution and pressure wave characteristics, a variation in the induced charge to the electrodes placed at the ends of the specimen is generated. Depending on the circuit conditions, open or closed, a variation of voltage or current will be generated as output, as shown in equations (1.8) and (1.9), respectively.

$$V(t) = X_s G_{\varepsilon_r} \int_0^{z_f} E(z,0) p(z,t)\, dz \tag{1.8}$$

$$I(t) = X_s C_0 G_{\varepsilon_r} \int_0^{z_f} E(z,0) \frac{\partial p(z,t)}{\partial t}\, dz \tag{1.9}$$

Where X_s is the compressibility of the sample, C_0 is the capacitance of noncompressed sample and G_{ε_r} is the ratio between the relative permittivity of the non-compressed (orange fraction of Figure 1.7, ε_r) and the compressed (yellow fraction of Figure 1.7, ε_r^*) parts of the sample. While, Z_f is the abscissa of the wavefront ($Z_f = v_s\, t$), $E(z,0)$ is the profile of the electric field within the sample at the instant when the compression is applied (time t = 0) and, finally, $p(z,t)$ is the pressure profile.

Analyzing the evolution over time of the voltage or current, it is possible to finally get information on the distribution of space charge within the sample. In the PEA method, the output signal is a voltage, while, in the PIPWP and LIPP methods the output is a current signal [4].

1.2.1. The Pulsed Electro Acoustic method

The PEA method was developed by Takada in 1987 [50]. The working operation is based on the one-dimension Coulomb force law and the principle diagram for a flat specimen is shown in Figure 1.8. It consists essentially of a high voltage direct current generator V_{dc}, which is used in order to create a constant electric field within the sample and then allow the accumulation of the space charges. These charges subjected to the pulse voltage $e_p(t)$ will move slightly, this movement generates pressure waves that reach the piezoelectric sensor (generally based on a 9 μm thick polyvinylidene fluoride, PVDF) which allows the conversion from an acoustic signal to a voltage signal proportional to the space charges. The absorber is used in order to avoid reflections and the amplifier to increase the amplification of the signal. Finally, the output voltage signal *V(t)*, viewed in the oscilloscope, is sent to the computer to be processed [4, 51]. The output signal of the system, in frequency domain, is expressed as the following equation:

$$V(f) = S(f)\left[\frac{\sigma(0)}{v_s \Delta\tau} + R(f) + \frac{\sigma(d)}{v_s \Delta\tau} \exp\left(-\frac{i2\pi f d}{v_s}\right)\right] \tag{1.10}$$

where *S(f)* is the system response function that depends on the properties of the transducer and amplifier, while the terms in square brackets represent the pressure wave. In which, the first component is the surface charge at the ground electrode (that corresponds to the electrode in the right side of Figure 1.8, near the transducer), the second component is the accumulated charge in the sample and the third component is the surface charge at the upper electrode. The sampling time is denoted by $\Delta\tau$, while v_s is the speed of sound of the sample with thickness from *0* to *d*. More mathematical details will be given in the following chapters in which the PEA method is widely described and discussed.

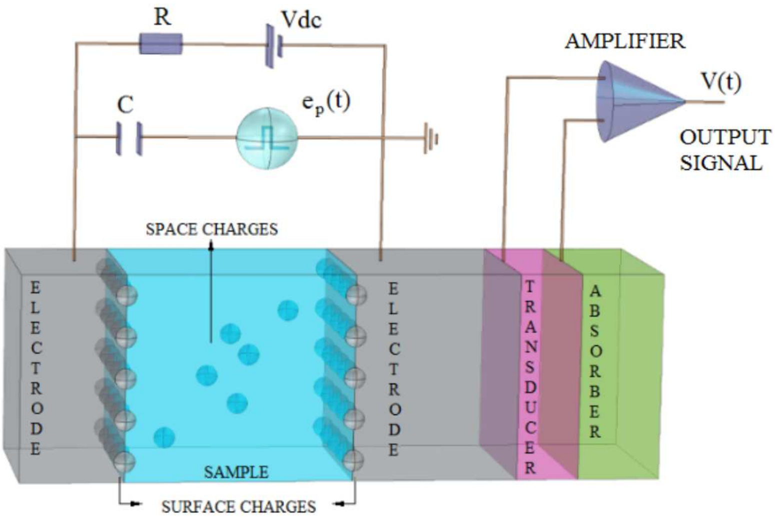

Figure 1.8. *Working principle of the PEA method*.

During the years many experiments have been done in different materials with thickness ranges between 27 mm and 25 µm. As regards the spatial resolution of the method, Kumaoka et al. brought the value of this parameter in the range between 1.6 µm and 3 µm for samples of thickness 25 - 100 µm, by using a pulse voltage of 100 V with the pulse width of 0.6 ns [52].

In order to test specimens at a normal operating conditions temperature, Kitajima et al. introduced a band heater around the upper part of the PEA cell, while on the lower electrode has been inserted a thermocouple as temperature sensor. A change was also made on the transducer, by replacing the PVDF (which is fine if the thermal gradient is low) with the lithium niobate ($LiNbO_3$) crystal, as the latter turns out to have a stable output signal to high temperatures, making the measure more accurate [53].

When the PEA method is used, both for flat specimens and for other type of tests discussed in the next paragraph, an important aspect concerns the material homogeneity. Indeed, if a material is not acoustically uniform, the acoustic wave generated from the charge can be distorted. Interesting studies have been made by Wadamori et al [54] in which they proposed a numerical model for estimating the effect of acoustic mismatching in a sample on the output of PEA signals. Whereas Holè et al. in [55-57] analyzed the case of complex geometries and the case in which filler particles are present inside the sample. In these works, it was found that if the diameter of the filler particles is larger than the smaller resolution of the measurement system, the output signal is distorted.

1.2.2. Three-Dimensional PEA

Three-Dimensional measures can be carried out when investigating small areas, such as voids or tree defects. For this purpose Imaizumi et al. developed the 3D PEA system, with a principle similar to the classic PEA and the difference of having a piezoelectric transducer and a detecting electrode with small dimensions. To carry out measures in 3D, in this first application, it was necessary to move the specimens along the coordinates x and y, to have as output the distribution of space charge along x, y, and z. In this way the method could not be easily used because it was necessary to move the sample, since the area where the measure was carried out was rather limited [58].

In 2001, Maeno improved the measurement system by introducing a numerical control on the detector’s position in order to measure the 3D distribution in a more practical and fast way. This new method is called "Acoustic lens method" and a diagram showing the principle is presented in Figure 1.9. In this case the sample remained still, while the detector constituted by the transducer and the acoustic lens moved along the lateral directions x and y. Only the pressure wave generated in the small focused area by the lens reaches the sensor. To obtain the complete 3D space charge distribution it is necessary to move this detector, acquire the new values, and then put them in sequence [59, 60].

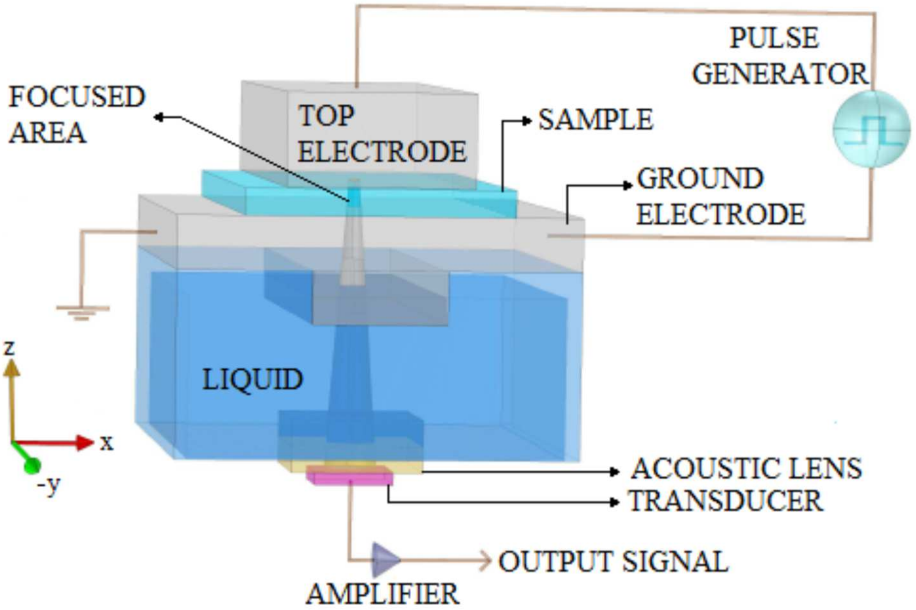

Figure 1.9. *Working principle of the Acoustic Lens method.*

The attained resolution was 12 μm in the thickness direction, and 0.5 mm in the lateral direction. Considering that both the transducer and the acoustic lens are in a shielded box placed under the ground electrode, the acoustic waves reached the sensor going through a liquid within the shielded box. It was found that the use of mercury as liquid, prevented the waves reflections from taking place in the interfaces electrode/liquid and liquid/lens. Mercury, indeed, shows acoustic impedance similar to that of aluminum constituting the cell components [60, 61].

In a recent work undertaken by Maeno et al. on samples of thickness between 250 and 750 μm, the resolution in the vertical direction is 16 μm, while in the lateral direction the resolution improves considerably to a value of 100 μm [62].

Unlike the classic PEA, in the 3D system, the output waveform has the main peak preceded by a broad signal, due to the use of acoustic lens.

The 3D PEA system is not suitable for observing space charge dynamics that change rapidly because it takes a long time to scan a small portion of material. Therefore it is widely used for monitoring long time ageing phenomena such as ion migration, for example in a printed circuit boards [63-65].

1.2.3. Two-Dimensional PEA

To evaluate the transient behavior of the space charge, a system for real-time measurement is needed. For this purpose, Fukuma et al. developed a 2D space charge measurement system. Such system was acting both in lateral direction and in the thickness direction, using the principle of the PEA method but with a greater number of acoustic sensors. The diagram showing the working principle is shown in Figure 1.10 and the method is called “multi-dimensional space charge measurement system” or “multi-sensor PEA system” [66]. During the experiments, the ten PVDF sensors were stuck to the bottom electrode, and spaced 3 mm from each other so that individual signals from the sensors were detected at the same time in which the coaxial switch was acting. The same data could be processed later. The system, with a resolution in the lateral direction of 3 mm was employed to measure both in 2D and in 3D depending on the sensors position: 2D, if they are located in line; 3D, if they are located in the nodes of a grid [59].

The number of sensors is limited by the analog to digital converter, which is more expensive in relation to the number of available channels. To make a less expensive system, either 2D or 3D, the Scanning Sensor Type (SST) was developed. It used an analog switch and a single channel A/D converter [67]. A detailed explanation, a description of the components used and the layout of the test system are reported in the same article. In [66-68] materials of different thickness between 100 and 300 μm were tested, obtaining a resolution of 15 μm in the thickness direction and 1.5 mm in the lateral direction for sensors placed at 1.5 mm (because the lateral resolution depends on the distance between the sensors).

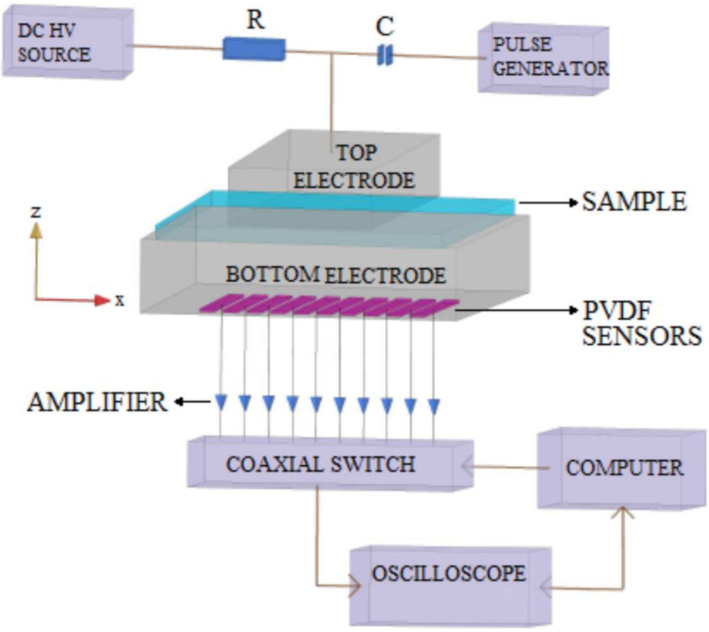

Figure 1.10. *Working principle of the Multi-dimensional space charge measurement system.*

1.2.4. Open Upper Electrode

Dielectric materials used in spacecrafts are subject to special environmental conditions. However in these cases the surface charge should also be considered. Given that the upper electrode is in contact with the specimen in the classic configuration of the PEA method, it is difficult to measure the surface charge. To measure the surface charge it is necessary to create a floating potential both on the surface as well as on the electrode. The electric field is then applied through the floating electrode, both to the bulk and to the surface of the specimen. In this way, the acoustic signals are generated both for the surface charges and for the space charges.

For this purpose, in 2004 [69] a new configuration of the PEA cell called "*Open Upper Electrode*" was developed, in which the top electrode remains detached from the sample. A detailed diagram showing the cell setup is shown in Figure 1.11 [70], and substantially there are no significant differences as compared to the traditional PEA. In ordinary PEA, also the sample pressed by the upper electrode remained in close contact with the electrodes. In this experimental setup, on the contrary, it was difficult to press the specimen because the upper electrode was not in touch with it. High viscosity silicone oil and other materials were thus used to improve the contact between the upper electrode and the sample. In this set-up, besides, is present a motor, which is used to move the upper electrode in the irradiation or measurement position.

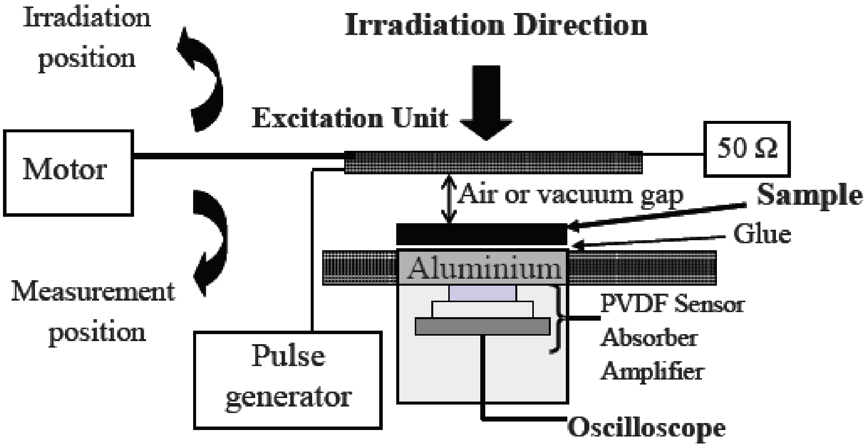

Figure 1.11. *Working principle of the Open PEA [70].*

In order to adapt the voltage pulse to the sample (and find a good compromise between applied voltage and sensitivity of the charge detection), the work in [70] proposes a gap of 1 mm between the electrode and the sample.

In [71-72] a new set-up called "*Open Ring Electrode*" (ORE) was proposed. Such setup, differently from the Open PEA, allowed carrying out the measure without stopping the electronic bombardment. In this way it was possible to perform measures during the irradiation. The tested samples had a thickness ranging between 189 μm and 500 μm with a resolution of a few micrometers.

1.2.5. Portable PEA

In 2002, Maeno created a portable space charge measurement system. Unlike the complete measuring system that is too large to be transported, the developed system improved the waveform of the voltage pulse so as to directly observe the profile of the space charge on the oscilloscope without the need to process the signal via PC [73]. The goal of the author was to match the waveform of pressure that arrived to the piezoelectric transducer directly with the space charge profile. The resolution of this measuring system was not very different from that of the classic PEA and was approximately equal to 10 μm for samples with thickness of 500 μm. The mathematical processes and details of the method that lead to the point of avoiding the deconvolution and so to the use of the PC are described in [73]. In the same work, there is also the diagram of the wiring and the description of the new pulse generator used, which differs from that of the traditional PEA primarily due to the fact that it provides a voltage pulse of a much smaller width.

The test ground includes the oscilloscope, a battery pack, the new pulse generator and a kind of pincer, which is nothing more that the mini-PEA cell, as reported in Figure 1.12 [59].

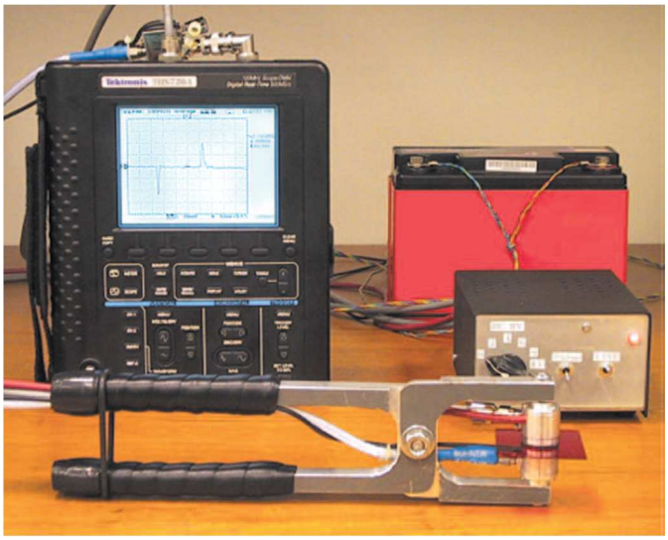

Figure 1.12. *Test ground of the Portable PEA [59].*

There is a problem in the construction of the upper electrode, because to avoid partial discharge this electrode is filled with epoxy resin. This implies that, if a fault occurs, the electrode will be changed entirely. With the suitable variations shown in [59], it is possible to use the mini-PEA cell also to carry out measures within the irradiation chamber. In this case the system was called "*Mountable PEA*" and different experimental tests are reported in [59, 61, 74].

A limitation of the portable PEA system is due to the fact that only the surface charge near the electrodes can be observed. This is because the electric field gradient is very low (about 12 kV/mm) to allow the formation of space charges within the sample.

1.2.6. PEA for cables

The application of the PEA method for coaxial geometries was performed by Fukunama in 1990 [75].

The principle of generation, propagation and reception of the acoustic wave remained the same to that of the PEA for flat specimens. The differences consist in the shape of the electrodes, in the features of the pulse generator and in the signal process.

To perform measurements in cables it is necessary to remove a part of the outer tape in order to have access to the external semiconductor layer and apply the pulse voltage $e_p(t)$ between ground and measuring point (at the centre of an exposed section of the external semicon) through two circular aluminum electrodes, as shown in Figure 1.13 [76-77].

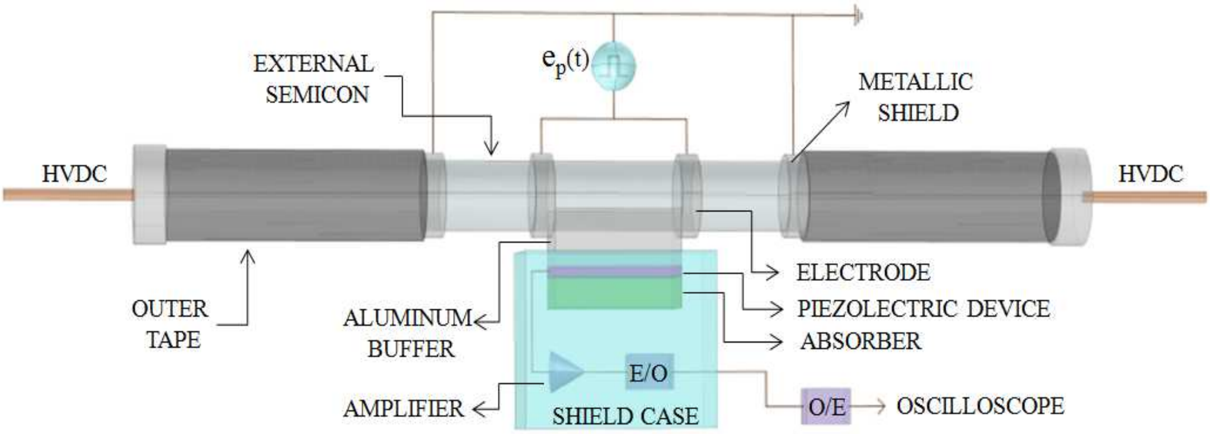

Figure 1.13. *Measuring set-up of the PEA method for cables.*

To prevent the change of the electrode dimensions for the analysis of cables with different sections, it is possible to use the floating ground electrode (an electrode of variable size). This type of cell has allowed the measurements of insulation thicknesses between 3.5 and 20 mm [78-83] with a resolution for the latter value approximated to tenths of a millimeter. The low value of the latter parameter was not a main problem, since the thicknesses analyzed were of considerable size.

The tests under temperature gradient, proposed by Wang in 1995, are carried out by using a current transformer which is used to circulate a certain current on the cable in order to bring it to the desired temperature, by exploiting the Joule effect [84].

The measures under thermal gradient, as well as for the power cables, have also been used for mini-cables. The measurement set up did not differ from the previous one and the scheme is shown in [85]. In this work, and in others found in literature [86-88], the type of insulation is always XLPE, while the thickness was approximately 1.5 mm.

Among the PEA developments, carried out by Montanari *et al.*, it is possible to find the system called "*Ultra-Fast space charge measurements*", used in the case in which the small charge quantities going through the cable insulations for a very small period of time, could be measured [89-91]. This arrangement is similar to the PEA system for cables, but it improved the acquisition speed by using last generation instruments. Moreover, the voltage pulse given by the pulse generator would have amplitude of 1500 V, duration 50 ns and 4 kHz repetition frequency [91].

As regards the disadvantages, there are several problems related to the application of the PEA method at cables geometries. Due to the greater complexity of the signal processing and in order to get an accurate space charge profile, it is necessary to consider the divergence of the voltage pulse and of acoustic wave across the insulation. The latter is also highly attenuated and distorted due to the high thicknesses of insulations under test [81]. Further problems reside in the measurement set-up, as it is very large and thus needs a lot of space, in particular for cable under test and terminations. In addition, the grounding system requires particular care in order to avoid spurious signals in the output waveform. Furthermore, in the PEA system there is a low signal-to-noise ratio combined with the frequency response of transducer and amplifier [33]. Ultimately, the PEA method is destructive for full-size cables since the outer tape and screen along the measuring area must be removed.

1.3. Pressure Wave Propagation Method

The PWP method, with principle of operation based on the propagation of a pressure wave within the sample, was conceived by Laurenceau in 1976 [92] and later developed by Alquié [93-95]. There are several configurations of this technique in relation to how the pressure wave is generated. The most employed ones used a piezoelectric transducer or a laser. If the transducer is used, the developed techniques are the "Piezoelectric Induced Pressure Wave Propagation method", PIPWP, also called “Piezo-PWP”, the "Piezoelectrically Induced Pressure Pulse", PIPP, and "Piezoelectrically Induced Pressure Step”, PIPS. This last technique developed by W. Eisenmenger et al. [96-98] together with the "Laser Induced Pressure Pulse method", LIPP, introduced in 1981 by G. M. Sessler et al. [99] in which the laser is used, laid the foundations for the development of these methods.

1.3.1. The PIPWP configuration

The PIPWP configuration, shown in Figure 1.14, uses the same components of the PEA cell (see Figure 1.8). Here, unlike the PEA method, a voltage pulse $e_p(t)$ is applied to a piezoelectric transducer in order to generates a pressure pulse. The latter propagates on the dielectric, perturbing the space charges with a consequent change of surface charges on the electrodes. From the measurement of the displacement current *i(t)*, due to the charge variation over time, it is possible to determine the distribution of space charge in the specimen with resolution that varies from 2 to 5% for the range of thicknesses between 100 and 1000 μm [100-101].

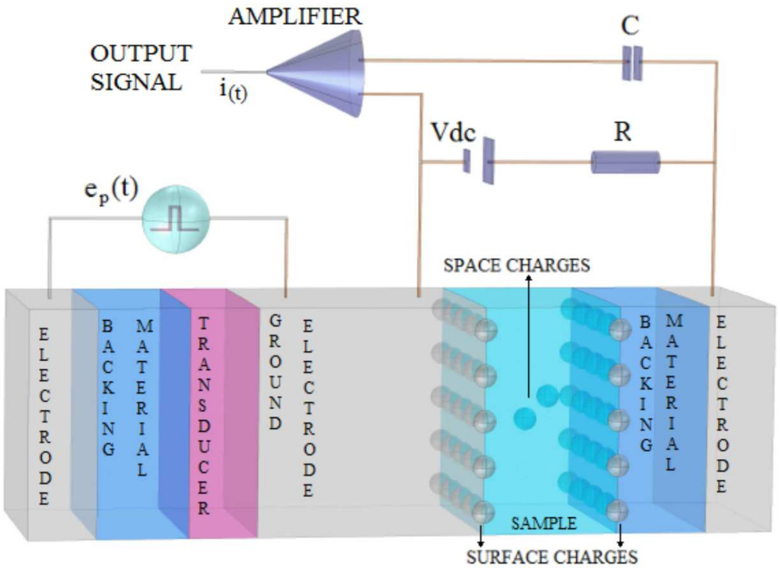

Figure 1.14. *Working principle of the PIPWP method.*

The output signal of the system, in frequency domain, is expressed as the following equation:

$$I(f) = S(f)\left[\frac{\sigma(0)}{u_s\Delta\tau} + R(f) + \frac{\sigma(d)}{u_s\Delta\tau}\exp\left(-\frac{i2\pi f d}{u_s}\right)\right] \tag{1.11}$$

where all terms are the same as those present in equation 1.10 for the PEA signal output.

The PWP technique is also used for measurements in 3D with a resolution in the directions x-y equal to 2.5 μm, while that in the z direction is not as efficient. The latter can be improved by increasing the working frequency [102]. Besides this, Takada et al. used a technique to calculate the space charge in dielectrics used in spacecraft [103]. In the same article they define the value of the resolution to 5 μm for a kapton sample with thickness of 50 μm.

A critical aspect of this method is the safety of the measurement system. Only a coupling capacitor separates the signal detecting circuit from the high voltage circuit. This means that the output signal is sensitive to external electrical noise and, therefore, if an electric breakdown takes place, the signal detection circuit could be destroyed [100].

1.3.2. The LIPP configuration

The LIPP method has been widely used by G.M. Sessler et al. not only for the measurement of space charge, but also for polarization and piezoelectricity profiles detection in different kinds of insulating materials [104-106] in which the resolution is about 1 μm [107]. The LIPP method in its latest configurations has a block diagram as shown in Figure 1.15 and employs a laser that shoots high intensity pulses on an absorbing layer placed on a side of the sample. The target absorbs the laser energy and converts it into a mechanical energy due to its expansion. In this way it creates a pressure wave that travels through the sample, resulting in the variation of the surface charge in the electrodes and consequently, in the appearance of electric current *i(t)* in the external circuit [4].

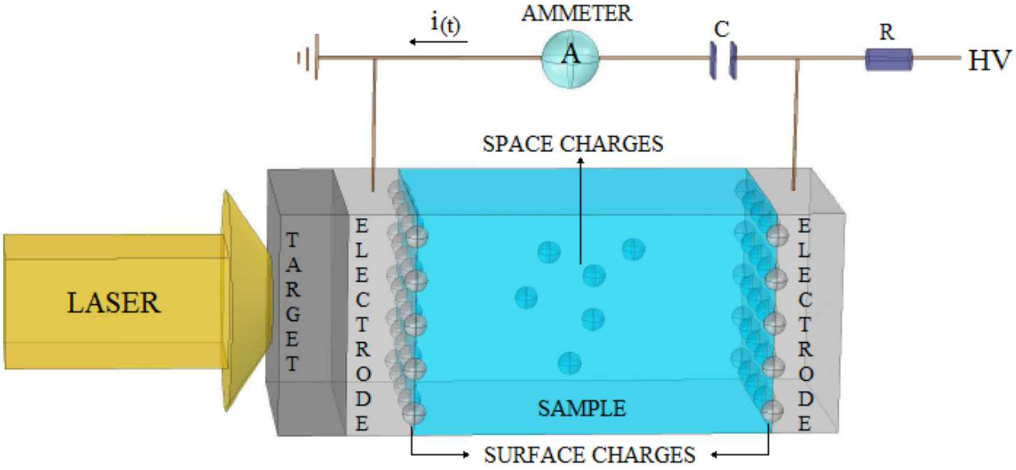

Figure 1.15. *Working principle of the LIPP method.*

By making a comparison with the methods previously described, which make use of the transducer, the LIPP shows a better spatial resolution due to a more rapid rising edge of the pressure pulses and also does not require a deconvolution.

The LIPP method is also employed to make tests under temperature gradient on the materials used in power cables. In the test setup, compared to the traditional case reported in Figure 1.15, some heating coils were added in proximity of the irradiated electrode as well as a thermocouple to measure the temperature [108].

In the past years, as indicated in [4], the method has been used for measurements on thin or very thin samples with thicknesses 0.1–1 mm, in cable specimens, but not to full-size power cables.

Recent developments of the method are proposed by Stéphan Holé in [109], where it is reported the possibility to bring the resolution to 50 nm in silicon dioxide and 100 nm in silicon nitride 200 nm thick, by using a laser pulse of the order of femtoseconds and an Electro-optic sampling.

The LIPP technique is also applicable to complex materials exhibiting either a divergent electric field or a heterogeneous structure. In these cases, the method has a problem due to the fact that the output signal is not only related to the presence of charges but it also depends on other spurious contributions [109].

To improve the sensitivity and resolution of the method the interface target/electrode was investigated, while the material, interposed between these two elements, had the task of reducing the reflections. Different liquids have been analyzed and it was pointed out that the best conditions were obtained by using a thin layer of Indian ink with laser pulse having energy equal to 180 mJ [110].

The LIPP technique, mainly in the past years, it was also used when the samples are previously charged with an electron beam. For example, the space charge distribution was determined in Mylar and Kapton films charged with 10 to 40 keV electron beams [111], but also in Polyethyleneterephthalate (PET) films charged with beam energies within the range of 4-55 keV [112].

The electron beam is used not only for charging the samples, as described above, but also to detect the space charge distribution within the insulating materials by means of the so called "*electron-beam method*". In this technique, the sample interposed between the two electrodes (rear and front electrodes), is initially charged, and then exposed to a series of electron beam irradiations. In this way, a virtual electrode is created and is capable to sweep through the sample in relation to the energy supplied by the electron beam irradiation. By sweeping the virtual electrode through the sample, from front to the rear electrode, an amount of charges will be released in the rear electrode; thus, the evaluation of the currents from the rear electrode yields the charge distribution [112, 113].

1.4. Optical method

The optical methods used to measure space charge distribution have not been widely used over the years due to the complexity of the measuring cell. For these reasons we will be given a brief and general description of these methods, without going into detail.

Optical methods are used to measure the distribution of space charge in dielectrics starting from the measurement of the electric field. When the lines of force of an electric field pass through a dielectric material the electro-optical effect appears. The latter consists in the change of the refractive index of the material itself. The phenomena that generate the refractive index variation are the Kerr effect and the Pockels effect. If a beam of light strikes a material with different values of refractive index, the birefringence arises. For the Pockels effect, which is a linear electro-optical effect often observed in crystalline materials, the difference in induced birefringence is linearly proportional to the electric field. While for the Kerr effect, which is a squared electro-optical effect, often observed in liquid materials, the difference in induced birefringence is proportional to the square of the electric field. The difference of induced birefringence can also arise due to a distribution of internal mechanical stress to solid dielectrics, the two effects are linearly connected and there is also a photoelastic effect [100]. A detailed analysis of the Kerr effect is given in [114-115]. While, as regards the possible applications, taking as a reference the most recent paper [116], the Kerr effect is used to evaluate the accumulation of the space charge in the oil for power transformers. In order to give an idea of the complexity of the measuring system, in Figure 1.16 the test set-up used in the same article is reported. The circular container, containing the electrodes and the oil to be tested, it is hit by a laser beam, the latter passes through it and comes out of a reflective surface and back again. The electric field is evaluated by the phase shift between the components of the laser beam. Any difference between the values of the electric field are justified by the presence of space charge accumulated, estimated through the Poisson equation.

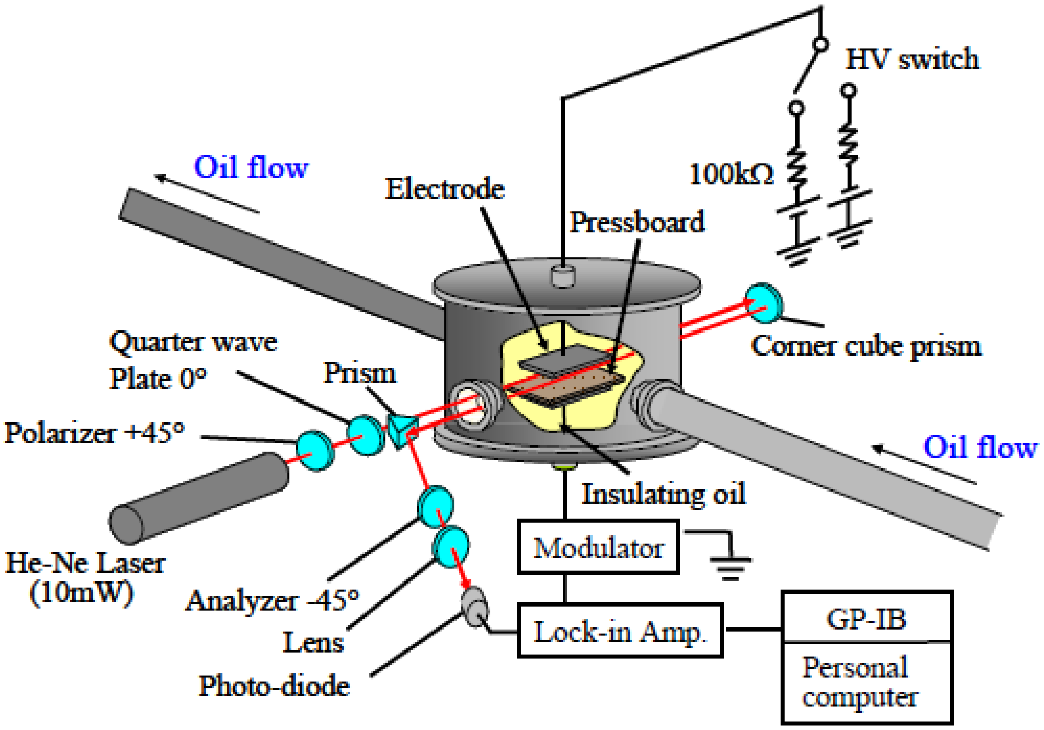

Figure 1.16. *Measurement setup in liquid dielectric using the Kerr effect.*

With regard to the Pockels effect, there are several articles describing the principle and the different applications, such as [117-119], while a description of the electric field sensors exploiting this effect is reported in [120-121]. The Pockels effect is most commonly used to measure the surface charges, therefore it has found a good application for the characterization of dielectrics used in spacecraft [117-118]. In [117], there is a 2D measuring system of the birefringence caused by the accumulation of charges in the crystal Pockels. The measurement sensitivity was improved by introducing the square pulsed optical phase modulation technique and an amplifier block to process the image recorded by a video camera. With this system it was possible to measure the phase delay to trace back the amount of the charged particles.

1.5. Discussion

The phenomenon of space charge accumulation, well studied in the past years, was strongly considered in the past decade thanks to the increased use of direct current due primarily to transport of electricity both over long distances and in the use of power electronics. The methods of measurement of space charge born several years ago, have been developed further in recent years. Thanks to the technological progress developed within the measurement equipment, new scopes, new types of laser, new converters, new pulse generators, new materials, have been employed to adapt the methods already used, to the new requirements, with a meaningful improvement spatial resolution.

In conclusion, it is now possible to perform measurements on both liquid and solid dielectric. For solid dielectrics the charge distribution is evaluated in one dimension with all the methods belonging to the acoustic and thermal groups, in two dimensions with the PEA and TPM methods, and in three dimensions, as well as with the latter two methods, even with the LIPP and FLIMM methods. For measurements on flat specimens by using the PEA method, the two variants of the PWP (PIPWP and LIPP), the TSM, the TPM and LIMM. While, for measurements on cables the most commonly used methods are PEA and TSM. As for the liquid dielectrics, the oils of transformers were the most investigated in recent years, the measurement of the space charge on them was carried out by optical methods utilizing the Kerr effect.

In Table 1.1 are summarized the thicknesses range of the samples analyzed and the best value of spatial resolution found in literature for each space charge measurement configuration discussed in this chapter, in particular for the methods belonging to the acoustic and thermal groups.

Table 1.1. *Overview of the resolution and specimens thickness used in the different measuring techniques.*

Group	Method	Configurations	Thickness (µm)	Resolution (µm)	Comments
Thermal	TSM	For Flat specimen	10 – 20000	~ 0.1 – 150	Measurements performed on very thin insulating require a faster heating. The resolution can reach the order of nm using a femtosecond pulse
		Cables	< 20000	1 – 10	The resolution is of the order of microns and depends on the homogeneity of the material
		ATWM	50 – 3000	1 – 10	The best resolution is obtained in the vicinity of the electrode thermally excited
	TPM	For Flat specimen	25 – 200	2.5	The resolution improves by taking the data from both sides of the sample
		Three-Dimensional	17	< 0.5	The resolution value in the table refers to the thickness direction. The resolution in the lateral direction is equal to 38 µm for a specimen width of a few millimeters
	LIMM	For Flat specimen	~ 100	1 – 2	These resolution values they have in the vicinity of the irradiated surface. Using a very tight laser pulse, the resolution can be up to about 100 nm
		FLIMM	< 200	~ 1	This is the resolution value along the thickness direction and depends on the magnitude of the laser beam. The resolution in the lateral direction is a few micrometers
Acoustic	PEA	For Flat specimen	25 - 27000	1.6	This is the better value of resolution reached, obtained by the smaller thickness, using a pulse voltage of 100 V and width 0.6 ns
		Three-Dimensional	250 - 750	16	The resolution value in the table refers to the vertical direction. In the lateral direction is 100 µm
		Two-Dimensional	100 - 300	15	Value of resolution in the vertical direction obtained for thicknesses from 100 µm. In the lateral direction that is 1.5 mm and depends on the distance between the sensors
		Open Upper Electrode	189 - 500	1 – 10	The resolution is a few micrometers. The system is used to measure surface charges and internal charge, even during irradiation
		Portable PEA	500	10	The performance of this method are very similar to those of the classic PEA
	PWP	For cables	3500 - 20000	100 - 1000	Although the resolution is of the order of millimeters, it is fine because the thickness of the insulation tested are significant
		Piezo – PWP	50 - 1000	5	The resolution value obtained for the smaller thickness in the application of dielectrics irradiated. In other cases the resolution is equal to 2 - 5 %

Chapter 2

The Pulsed Electro Acoustic (PEA) method

The working principle of PEA method has been already described in the previous chapter. Here, instead, its theoretical aspects and the related equations are discussed in detail.

In the first sections, the equations concerning the generation and induction of surface charges at the electrodes of the PEA cell, due to the applied high voltage stress and to the pulse voltage but also to the accumulated space charges, are reported and described. Besides this, the equations related to the generation, transmission and reflection of acoustic waves within the PEA cell, due to the charges vibration, are also analyzed.

Then, considering that the most relevant PEA cell components in which acoustic waves reflections can occur are the absorber and the ground electrode, the expressions useful to properly sized these two component are obtained.

In the second part of this chapter, the equation of PEA cell output signal is reported, as well as the effect of transducer thickness and pulse source on its magnitude and resolution values.

Finally, a detailed description of deconvolution technique and calibration process is given.

2.1 Generated and induced surface charges

By taking into account the working principle and the block diagram of the PEA cell previously described in Section 1.2.1, when the voltage DC stress V_{dc} is applied, in the first time intervals an amount of surface charge σ_{dc} begins to accumulate in correspondence of the sample interfaces. It depends on the applied electric field E_{dc} and on the dielectric constant ε:

$$\sigma_{dc} = \varepsilon E_{dc} \tag{2.1}$$

where:

- $\varepsilon = \varepsilon_0 \varepsilon_r$ (in which ε_0 is the dielectric permittivity of the free space and ε_r is the relative permittivity of the dielectric material);
- $E_{dc} = V_{dc}/d$ (where d is the thickness of the sample).

The accumulated surface charges in both sample interfaces are opposite in sign and equal in magnitude:

$$\sigma_{dc}^{+} = \varepsilon E_{dc} \tag{2.2}$$

$$\sigma_{dc}^{-} = -\,\varepsilon E_{dc} \tag{2.3}$$

The superscript "+" and "–" are referred to the surface charge accumulated in the vicinity of the High Voltage (HV) electrode (which is a positive electrode) and in proximity of the ground electrode (which is a negative electrode), respectively.

When the pulse generator $e_p(t)$ is applied (which is used to vibrate the charges) a further quantity of surface charge, named σ_{pulse}, is induced in correspondence of the positive (equation 2.4) and negative (equation 1.5) electrode:

$$\sigma_{pulse}^{+} = \frac{\varepsilon}{2} e_p(t) \tag{2.4}$$

$$\sigma_{pulse}^{-} = -\frac{\varepsilon}{2} e_p(t) \tag{2.5}$$

When a certain quantity of space charge $\rho(x)$ is accumulated in the bulk of the sample, the amount of surface charge σ_ρ, induced by it, results equal in sign and opposite in magnitude. The latter parameter depends on the distance between the space charge position x_ρ and the electrode (see Figure 2.1), as shown in equations (2.6) and (2.7):

$$\sigma_\rho^{+} = -\int_0^d \frac{x_\rho}{d}\, \rho(x) dx \tag{2.6}$$

$$\sigma_\rho^{+} = -\int_0^d \frac{d - x_\rho}{d}\, \rho(x) dx \tag{2.7}$$

where *d* is the thickness of the sample.

The total surface charge σ^{+} and σ^{-}, accumulated in correspondence of the HV-electrode/sample and sample/ground-electrode interfaces, respectively, are given by the following equations (2.8) and (2.9):

$$\sigma^{+} = \sigma_{dc}^{+} + \sigma_{pulse}^{+} + \sigma_\rho^{+} = \varepsilon E_{dc} + \frac{\varepsilon}{2} e_p(t) - \int_0^d \frac{x_\rho}{d}\, \rho(x) dx \tag{2.8}$$

$$\sigma^{-} = \sigma_{dc}^{-} + \sigma_{pulse}^{-} + \sigma_{\rho}^{-} = -\varepsilon E_{dc} - \frac{\varepsilon}{2} e_p(t) + \int_0^d \frac{d - x_\rho}{d} \rho(x)dx \qquad (2.9)$$

Considering that the magnitude of $e_p(t)$ is much smaller compared to E_{dc}, the second term of equations (2.8) and (2.9) can be neglected [51].

A schematic representation of the accumulated surface charges described in the equations above, without considering σ_{pulse}, is shown in Figure 2.1.

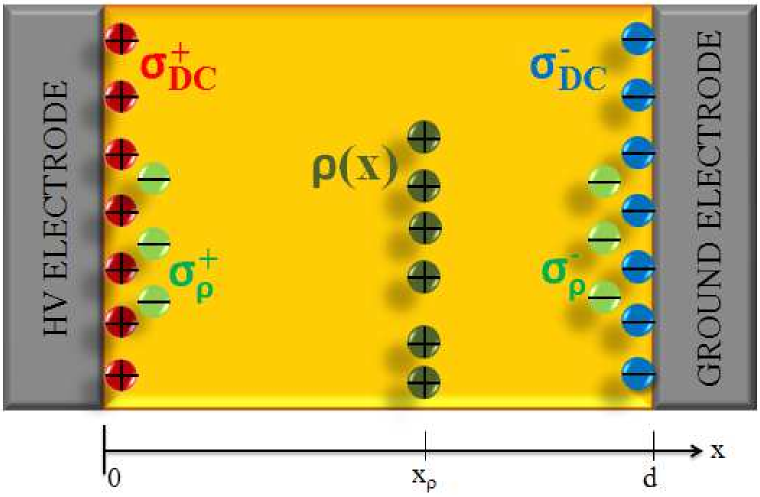

Figure 2.1. *Accumulated surface charges due to the constant electric field E_{dc} and space charge $\rho(x)$.*

2.2 Electrostatic forces

As previously explained, in PEA measurements the accumulated charges are subjected to the applied electric field $E_{dc}(x)$ and to the pulse electric field $e_p(t)$. Therefore, the total electric field $E(x,t)$ that acts on the charges is equal to the sum of both terms:

$$E(x,t) = E_{dc}(x) + e_p(t) \qquad (2.10)$$

According to Coulomb law, $F = q\,E$ (where q is the charge and F the force), the electrostatic forces generate by the electric field $E_{dc}(x)$ are:

$$f_{E_{dc}}^{+}(x) = \frac{1}{2}\sigma^{+} E_{dc}(x) = \frac{1}{2}\varepsilon {E_{dc}}^{2}(x) \qquad (2.11)$$

$$f_{E_{dc}}^{-}(x) = \frac{1}{2}\sigma^{-}E_{dc}(x) = \frac{1}{2}\varepsilon {E_{dc}}^{2}(x) \tag{2.12}$$

$$\Delta f_{E_{dc}}^{\rho}(x) = \rho(x)\Delta x E_{dc}(x) \tag{2.13}$$

where $f^{+}(x)$ and $f^{-}(x)$ are the forces acting on the surface charge σ^{+} and σ^{-}, respectively. While, $\Delta f^{\rho}(x)$ is the force acting on a thin space charge layer Δx placed in the generic position x.

Likewise, the forces generated by the pulse electric field $e_p(t)$ are:

$$f_{e_p}^{+}(t) = \sigma^{+}e_p(t) + \frac{1}{2}\varepsilon {e_p}^{2}(t) = \left[\sigma^{+} + \frac{1}{2}\varepsilon e_p(t)\right] e_p(t) \tag{2.14}$$

$$f_{e_p}^{-}(t) = \sigma^{-}e_p(t) - \frac{1}{2}\varepsilon {e_p}^{2}(t) = \left[\sigma^{-} - \frac{1}{2}\varepsilon e_p(t)\right] e_p(t) \tag{2.15}$$

$$\Delta f_{e_p}^{\rho}(x,t) = \rho(x)\Delta x e_p(t) \tag{2.16}$$

Because the working operation of the PEA method is based on the propagation of pressure waves generated from charges vibration, the electrostatic forces $f(x)$ due to Laplacian electric field $E_{dc}(x)$ (which represents a constant pressure) can be neglected. Therefore, only equations (2.14-2.16) are taken into account in the following, since only them are responsible of charges vibration [51].

2.3 Generation and propagation of acoustic waves

The charges vibration, due to the forces $f_{e_p}(t)$, generates acoustic waves which propagate within the PEA cell. When the acoustic waves travel in different components (made of different materials) of the PEA cell, are partially transmitted and partially reflected. These phenomena are described by the generation K^{G}, transmission K^{T} and reflection K^{R} coefficients, calculated as:

$$K_{i-j}^{G} = \frac{Z_j}{Z_i + Z_j} \tag{2.17}$$

$$K_{i-j}^{T} = \frac{2Z_j}{Z_i + Z_j} \tag{2.18}$$

$$K_{i-j}^{R} = \frac{Z_j - Z_i}{Z_i + Z_j} \tag{2.19}$$

where Z is the acoustic impedance of the material, calculated as product of mass density and acoustic velocity of the medium. The subscript i indicates the material from which the wave is generated or come from, while the subscript j indicates the material from which the wave is traveling.

The propagation time τ_x, useful for an acoustic wave to travel from one point to another point of a component x with thickness d_x, material i and speed of sound v_i, is calculated by the following equation:

$$\tau_x = \frac{d_x}{v_i} \tag{2.20}$$

In the configuration of Figure 2.2, consisting in a sample of dielectric material "A" placed between the HV and ground electrodes (both made of aluminum, AL), the generation and transmission coefficients are reported and described (reflection phenomenon are not considered here, it will be discussed later).

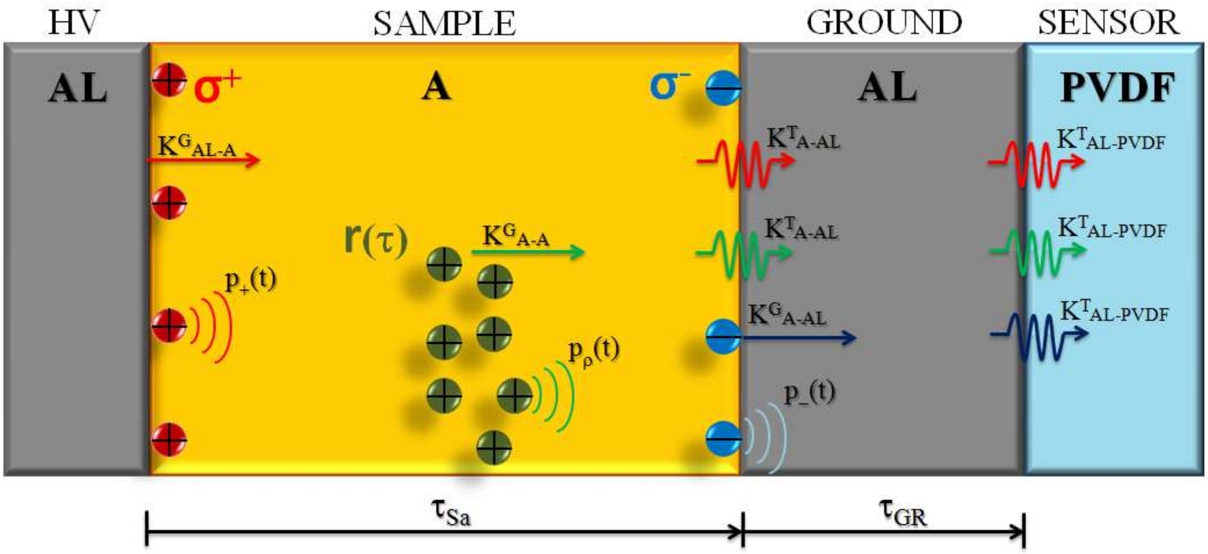

Figure 2.2. *Generation and propagation of acoustic pressure waves.*

In the following, a description of the generation and transmission coefficients illustrated in Figure 2.3 is given, while the pressure wave $p_+(t)$, $p_-(t)$ and $p_\rho(t)$ are explained later.

When the acoustic wave is generated by the positive surface charge accumulated in the HV-electrode/sample interface, the generation coefficient K^{G}_{AL-A} is calculated as equation (2.21). The generated acoustic wave travels through the dielectric material and reaches the sample/ground-electrode interface. In this point the fraction of the acoustic wave that will be transmitted towards the ground electrode depends on the transmission coefficient K^{T}_{A-AL}, calculated as equation (2.22). Before that the acoustic wave reaches the piezoelectric sensor (made of PDVF), it must pass through the ground-electrode/sensor interface. The transmission coefficient of this last interface, $K^{T}_{AL-PVDF}$, is given by equation (2.23).

$$K^{G}_{AL-A} = \frac{Z_A}{Z_{AL} + Z_A} \tag{2.21}$$

$$K^{T}_{A-AL} = \frac{2Z_{AL}}{Z_A + Z_{AL}} \tag{2.22}$$

$$K^{T}_{AL-PVDF} = \frac{2Z_{PVDF}}{Z_{AL} + Z_{PVDF}} \tag{2.23}$$

Concerning the acoustic wave generated by negative surface charge accumulated in the sample/ground-electrode interface, the generation coefficient K^{G}_{A-AL} is given by equation (2.24). While the transmission coefficient of the ground-electrode/sensor interface, $K^{T}_{AL-PVDF,}$ is the same of equation (2.23).

$$K^{G}_{A-AL} = \frac{Z_{AL}}{Z_A + Z_{AL}} \tag{2.24}$$

As regard the generation coefficient of acoustic wave generated by the space charge accumulated in the bulk of the sample, equation (2.17) can be used. For a homogeneous material "A" the generation coefficient K^{G}_{A-A} is equal to:

$$K^{G}_{A-A} = \frac{Z_A}{Z_A + Z_A} = 0.5 \tag{2.25}$$

The value 0.5 means that in a homogeneous material, the 50% of generated acoustic wave at one point propagates in one direction, and the other 50% in the opposite direction. Also in this case, the transmission coefficients at the sample/ground-electrode and ground-electrode/sensor interfaces are the same of equation (2.22) and (2.23), respectively.

The transit time of an acoustic wave that travels through a material is calculated by using equation (2.20). In case of Figure 2.2, τ_{Sa} is the transit time referred to the sample of material “A”, while τ_{GR} is the transit time referred to the ground electrode:

$$\tau_{Sa} = \frac{d_{Sa}}{v_A} \tag{2.26}$$

$$\tau_{GR} = \frac{d_{GR}}{v_{AL}} \tag{2.27}$$

where d_{Sa} and d_{GR} are the thickness of the sample and ground electrode, while v_A and v_{AL} are the speed of sound in the middle “A” and aluminum, respectively.

Therefore, in the situation of Figure 2.3, the generated acoustic waves (or pressure waves) $p(t)$ propagating in the piezoelectric direction are calculated as follows:

- acoustic wave originating from the positive surface charge σ^+

$$p_+(t) = K^G_{AL-A}\, K^T_{A-AL}\, K^T_{AL-PVDF}\, f^+_{e_p}(t) \tag{2.28}$$

- acoustic wave originating from the negative surface charge σ^-

$$p_-(t) = K^G_{A-AL}\, K^T_{AL-PVDF} f^-_{e_p}(t) \tag{2.29}$$

- acoustic wave originating from the space charge $\rho(x)$

$$\Delta p_\rho(x,t) = K^G_{A-A}\, K^T_{A-AL}\, K^T_{AL-PVDF} \Delta f^\rho_{e_p}(x,t) \tag{2.30}$$

By taking into account the transit time τ_{Sa} and τ_{GR} (equation (2.26) and (2.27)) in the expressions of the generated forces (2.14 -2.16), equations (2.28-2.30) can be rewritten as:

$$p_+(t) = K^G_{AL-A}\, K^T_{A-AL}\, K^T_{AL-PVDF} \left[\sigma^+ + \frac{1}{2}\varepsilon e_p(t - \tau_{\mathrm{Sa}} - \tau_{\mathrm{GR}})\right] e_p(t - \tau_{\mathrm{Sa}} - \tau_{\mathrm{GR}}) \tag{2.31}$$

$$p_-(t) = K^G_{A-AL}\, K^T_{AL-PVDF}\left[\sigma^- - \frac{1}{2}\varepsilon e_p(t-\tau_{\mathrm{GR}})\right] e_p(t-\tau_{\mathrm{GR}}) \tag{2.32}$$

$$\Delta p_\rho(x,t) = K^G_{A-A}\, K^T_{A-AL}\, K^T_{AL-PVDF}\rho(x)\Delta x e_p(t - \frac{\mathrm{d_{Sa}-x_\rho}}{\mathrm{v_A}} - \tau_{\mathrm{GR}}) \tag{2.33}$$

Equation (2.33) is referred at a thin space charge layer *Δx* placed in a generic position x_ρ of the sample, which is distant $d_{Sa} - x_\rho$ from the HV electrode (see Figure 2.1 in which $d = d_{Sa}$). While, the acoustic pressure wave generated by all of the space charge $r(\tau)$ is shown in equation (2.34). In which the term $d_{Sa} - x_\rho$ of equation (2.33) has been replaced by $v_A\tau$. Where v_A is constant and $\tau$is the transit time of an acoustic wave which propagates from a generic position.

$$p_\rho(t) = 0.5\, K^T_{A-AL}\, K^T_{AL-PVDF} v_A \int_0^t r(\tau) e_p(t-\tau-\tau_{\mathrm{GR}})\mathrm{d}\tau \tag{2.34}$$

Where the value 0.5 comes from equation (2.25).
The total acoustic wave $p_{tot}(t)$ that reaches the piezoelectric sensor is the sum of $p_+(t)$, $p_-(t)$ and $p_\rho(t)$, as reported in the following equation [51].

$$\begin{aligned} p_{tot}(t) &= p_+(t) + p_-(t) + p_\rho(t) = \\ & K^G_{AL-A}\, K^T_{A-AL}\, K^T_{AL-PVDF}\left[\sigma^+ + \frac{1}{2}\varepsilon e_p(t-\tau_{\mathrm{Sa}}-\tau_{\mathrm{GR}})\right] e_p(t-\tau_{\mathrm{Sa}}-\tau_{\mathrm{GR}}) + \\ & + K^G_{A-AL}\, K^T_{AL-PVDF}\left[\sigma^- - \frac{1}{2}\varepsilon e_p(t-\tau_{\mathrm{GR}})\right] e_p(t-\tau_{\mathrm{GR}}) + \\ & + 0.5\, K^T_{A-AL}\, K^T_{AL-PVDF} v_A \int_0^t r(\tau) e_p(t-\tau-\tau_{\mathrm{GR}})\mathrm{d}\tau \end{aligned} \tag{2.35}$$

2.4 Reflections of acoustic waves

The effect of wave reflections in PEA measurements could cause incorrect interpretation of the output signal. As previously reported in equation (2.19), the reflection coefficient K^R_{i-j} of an acoustic wave that travels through an interface *i-j*, depends on the acoustic impedances Z_i and

Z_j. If $Z_i = Z_j$, the acoustic wave that travels from material i to material j is not affected by reflections. In this case, considering a sample without accumulated space charge, the output charge profile is constituted of only two peaks due to the positive and negative surface charges. Whereas, if $Z_i \neq Z_j$, the coefficient K^R_{i-j} is different from zero and thus reflections occur. In this case, the output signal of the PEA cell is characterized by others peaks due to reflections, apart from the original signal. Therefore, the correct evaluation of the charge profile becomes complicated.

In the following, a theoretical analysis of the reflections wave phenomenon is given, while in the next chapter the effect of reflections in PEA cell output signal are evaluated by simulations. In order to avoid acoustic wave reflections in the output original signal, the ground electrode and the absorber of the PEA cell should be correctly sizing, as explained below.

2.4.1 Acoustic wave reflections within the ground electrode

The ground electrode acts as a delay line for the acoustic wave, with the aim to avoid that reflections anticipate the main signal. In the event that the thickness of the ground electrode is not properly sized, wave reflections occur and false signals are present in the output charge profile.

In the configuration depicted in Figure 2.3, wave reflections are analyzed in a free space charge single layer specimen, and hereinafter a description is given.

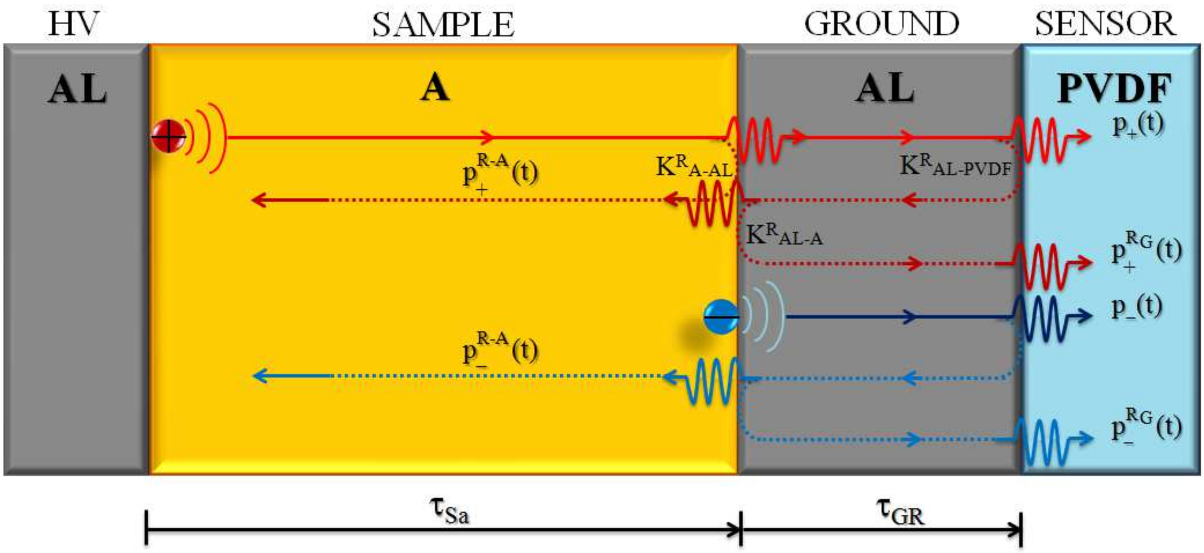

Figure 2.3. *Reflection of acoustic waves in a free space charge single layer specimen. The effect of ground electrode thickness.*

The generated acoustic wave in the HV-electrode/sample interface, $p_+(t)$, needs a time $\tau_{\mathrm{Sa}} + \tau_{\mathrm{GR}}$ to reach the piezoelectric sensor. When $p_+(t)$ passes through the sample/ground-electrode interface, is partially transmitted and partially reflected. This latter portion, named $p_+^{R-A}(t)$, according to the reflection coefficient K_{A-AL}^{R}, is reflected and go back to the HV-electrode direction. Further reflections of $p_+^{R-A}(t)$ are negligible because the time taken to reach the transducer will be greater compared to that taken by the original signal $p_+(t)$. The transmitted portion of $p_+(t)$ reaches the transducer after a time equal to $\tau_{\mathrm{Sa}} + \tau_{\mathrm{GR}}$ (as previously described in equation 2.31). At the same time a portion of $p_+(t)$, named $p_+^{R_G}(t)$, is twice reflected within the ground electrode in accordance to the reflection coefficients $K_{AL-PVDF}^{R}$ and K_{AL-A}^{R}. Finally, the reflected wave $p_+^{R_G}(t)$, described by equation (2.36), reaches the transducer after a time equal to $\tau_{\mathrm{Sa}} + 3\tau_{\mathrm{GR}}$.

$$p_+^{R_G}(t) = K_{TOT}\left[\sigma^+ + \frac{1}{2}\varepsilon e_p(t - \tau_{\mathrm{Sa}} - 3\tau_{\mathrm{GR}})\right] e_p(t - \tau_{\mathrm{Sa}} - 3\tau_{\mathrm{GR}}) \qquad (2.36)$$

Where $K_{TOT} = K_{AL-A}^{G}\, K_{A-AL}^{T}\, K_{AL-PVDF}^{R} K_{AL-A}^{R} K_{AL-PVDF}^{T}$.

As regard the generated acoustic wave in the sample/ground-electrode interface, $p_-(t)$, it needs only the time τ_{GR} to reach for the first time the transducer. After that, a fraction of $p_-(t)$, named $p_-^{R_G}(t)$, is reflected within the ground electrode in the same manner of $p_+^{R_G}(t)$. Finally, $p_-^{R_G}(t)$, described by equation (2.37), reaches the transducer for the second time after $3\tau_{\mathrm{GR}}$. While, the transmitted fraction in the HV-electrode direction, $p_-^{R-A}(t)$, is negligible as in the case of $p_+^{R-A}(t)$ [122].

$$p_-^{R_G}(t) = K_{A-AL}^{G}\, K_{AL-PVDF}^{R}\, K_{AL-A}^{R}\left[\sigma^- - \tfrac{1}{2}\varepsilon e_p(t - 3\tau_{\mathrm{GR}})\right] e_p(t - 3\tau_{\mathrm{GR}}) \qquad (2.37)$$

Considering that $p_-^{R_G}(t)$ reaches the transducer before than $p_+^{R_G}(t)$, more attention should be paid to $p_-^{R_G}(t)$ because it may give rise to false signals in the original charge profile. In order to avoid that the reflection $p_-^{R_G}(t)$ reaches the transducer before the original signal $p_+(t)$, the ground electrode should be sizing in accordance to the following relationship:

$$d_{GR} > \frac{1}{2} d_{Sa} \frac{v_{AL}}{v_A} \qquad (2.38)$$

As can be noted, reflections in the original signals depend on the sample thickness and on the sound velocity of the two media, such as aluminum and dielectric material “A”.

2.4.2 Acoustic wave reflections within the absorber

The absorber, placed in contact to the transducer, is useful to avoid wave reflections in the original signal, as in the case of the ground electrode previously analyzed. In the other side of the absorber is placed the bottom electrode (not inserted in Figure 1.8) useful to protect the transducer and the absorber which would otherwise be in contact with the work bench.

Considering that the absorber and the transducer are made by the same material (PVDF), the transmission and the reflection coefficients, $K_{PVDF-PDVF}^{T}$ and $K_{PVDF-PVDF}^{R}$, are equal to 1 and 0 respectively. This means that the acoustic wave reaching the transducer/absorber interface is totally transmitted. While, in correspondence of the absorber/bottom-electrode interface, $K_{PVDF-AL}^{R}$ is different from zero, and therefore the acoustic wave is partially transmitted and partially reflected. The reflected waves in the latter interface, travelling in the transducer direction, may affect the original signal.

In the following, only the wave reflections within the absorber are taken into account, as reported in Figure 2.4. To reach the piezoelectric sensor, the generated acoustic wave $p_{+}(t)$ needs a time equal to $\tau_{\mathrm{Sa}} + \tau_{\mathrm{GR}}$ (as in the Figure 2.3). While the reflected wave $p_{+}^{R_{ABS}}(t)$ needs a time $\tau_{+}^{R_{ABS}} = \tau_{\mathrm{Sa}} + \tau_{\mathrm{GR}} + \tau_{\mathrm{SE}} + 2\tau_{\mathrm{ABS}}$ (τ_{SE} and τ_{ABS} are the transit time of the sensor and absorber, respectively). For the same aim, $p_{-}(t)$ and its reflection $p_{-}^{R_{ABS}}(t)$ need a time intervals equal to τ_{GR} and $p_{-}^{R_{ABS}} = \tau_{\mathrm{GR}} + \tau_{\mathrm{SE}} + 2\tau_{\mathrm{ABS}}$, respectively.

The reflected waves $p_{+}^{R_{ABS}}(t)$ and $p_{-}^{R_{ABS}}(t)$ are given by:

$$p_{+}^{R_{ABS}}(t) = K_{AL-A}^{G}\, K_{A-AL}^{T}\, K_{AL-PVDF}^{T}\, K_{PVDF-AL}^{R} \left[\sigma^{+} + \tfrac{1}{2}\varepsilon e_{p}\left(t - \tau_{+}^{\mathrm{R_{ABS}}}\right)\right] \cdot \\ \cdot\; e_{p}\left(t - \tau_{+}^{\mathrm{R_{ABS}}}\right) \tag{2.39}$$

$$p_{-}^{R_{ABS}}(t) = K_{A-AL}^{G}\, K_{AL-PVDF}^{T}\, K_{PVDF-AL}^{R} \left[\sigma^{+} + \frac{1}{2}\varepsilon e_{p}(t - \tau_{-}^{\mathrm{R_{ABS}}})\right] e_{p}(t - \tau_{-}^{\mathrm{R_{ABS}}}) \tag{2.40}$$

Considering that both $p_{+}(t)$ and $p_{-}(t)$, described by equation (2.31) and (2.32), reach the transducer always before $p_{+}^{R_{ABS}}(t)$, the latter wave does not influence the original output signal. While, the reflected wave $p_{-}^{R_{ABS}}(t)$ could anticipate $p_{+}(t)$ if the absorber is not properly sized. In this case the thickness of the absorber d_{ABS} should be chosen according to the following relationship (2.41). In which the transit time within the sensor has been neglected.

$$d_{ABS} > \frac{1}{2} d_{Sa} \frac{v_{PVDF}}{v_A} \tag{2.41}$$

Where v_{PVDF} is the sound velocity of the absorber material.

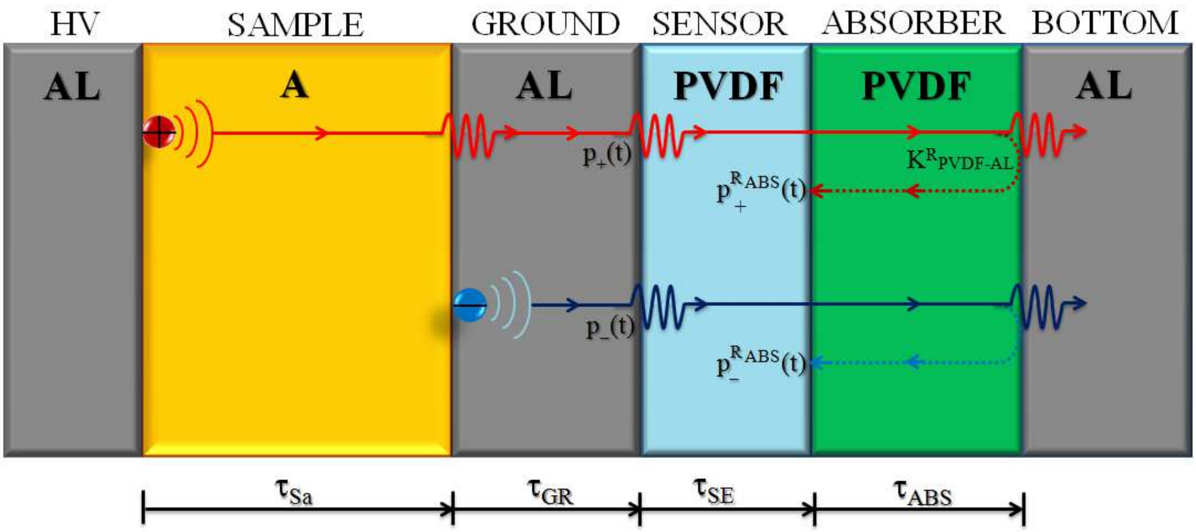

Figure 2.4. *Reflection of acoustic waves in a free space charge single layer specimen. The effect of the absorber thickness.*

If both relationship (2.38) and (2.41) are fulfilled, the original signal is not affected by reflections also in case in which space charge is presents in the insulation bulk. However, more attention should be paid in the case of multi-layer specimen. This aspect will be discuss later. The theoretical treatment described above is confirmed by simulation results reported in the next Chapter 3.

2.5 Output signal of the piezoelectric sensor

When the acoustic pressure wave $p_{tot}(t)$, described in equation (2.35), propagates through the piezoelectric sensor, an amount of charge $q(t)$ is induced on its surface due to the piezoelectric effect. The amount of this charge depends on the pressure wave $p_{tot}(t)$, but also on the piezoelectric constant P_c and area S of the transducer, as shown in equation (2.42).

$$q(t) = P_c S p_{tot}(t) \tag{2.42}$$

The electrical potential between the transducer surfaces, which represents its output signal $V_{PVDF}(t)$ is calculated as follows:

$$V_{PVDF}(t) = \frac{q(t)}{C_p} \tag{2.43}$$

where C_p is the static capacitance of the transducer equal to $\varepsilon S/d_{SE}$ (with $\varepsilon = \varepsilon_0 \varepsilon_{PVDF}$ and d_{SE} is the piezoelectric thickness). Therefore, equation (2.43) can be rewritten as:

$$V_{PVDF}(t) = \frac{q(t)}{C_p} = \frac{P_c\, S\, p_{tot}}{\varepsilon \frac{S}{d_{SE}}} = \frac{P_c d_{SE}}{\varepsilon} p_{tot}(t) \tag{2.44}$$

As can be seen in equation (2.44), the electrical output signal is proportional to the incident pressure wave and to the transducer thickness. While the area of the transducer is irrelevant.

2.6 Effect of transducer thickness and pulse source in the magnitude and resolution of the PEA output signal

The thickness of the piezoelectric sensor plays an important role even in the system measurement resolution. Indeed, for a smaller value of d_{SE}, the spatial resolution will be better. And vice versa, for larger values of d_{SE}, it results poorer. Therefore the choice of the transducer thickness needs attention since it is essential to have both a better resolution value and a high magnitude of the output signal. However these last two parameters depend also on the pulsewidth of the applied pulse voltage. A mathematical expression that proves the dependence of the output signal magnitude on the pulsewidth does not exist. As well as an equation in which it is shown the correlation between the spatial resolution and the transducer thickness. Nevertheless several works are present in literature in which these aspects are evaluated through simulations. It was found that the output signal magnitude is proportional to the pulsewidth (if the pulsewidth increases, the signal magnitude increase as well). Furthermore, as previously explained, simulation results show that the spatial resolution results poorer for thicker transducer.

By using the simulation model developed in this thesis, which will be widely described in the next chapters, two different pulse generators (with different pulsewidth) have been applied in a specimen containing only surface charges in correspondence of the electrode/sample interfaces, as shown in Figure 2.5. While, the effect of transducer thickness is evaluated in the next chapter.

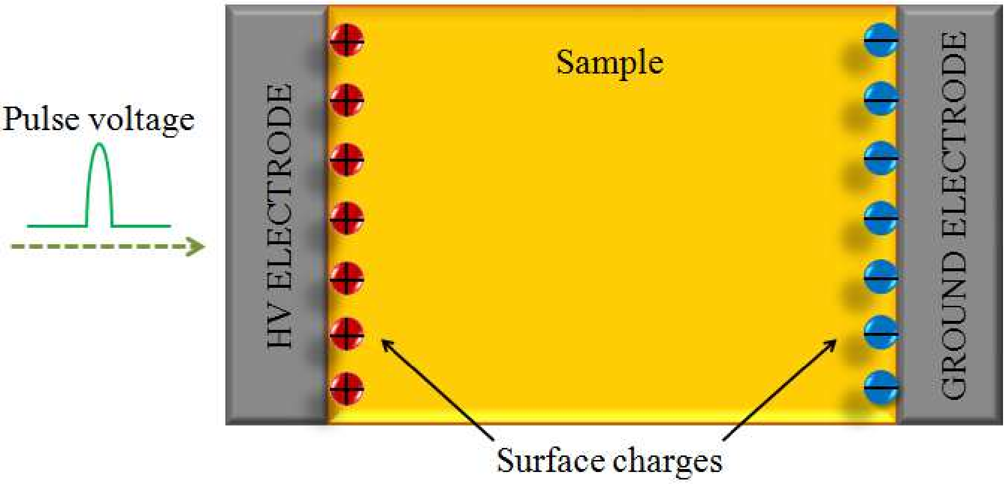

Figure 2.5. *Specimen containing surface charges, used to analyze the effect of pulsewidth on the output signal.*

As for example, two Gaussian pulses (which represent the ideal pulse voltage) with width *ΔT* equal to 0.7 ns and 10 ns have been chosen as pulse generator. The magnitude of both pulse sources has been selected 100 V, while *ΔT* is calculated in correspondence of 50% of the pulse magnitude, as shown in Figure 2.6.

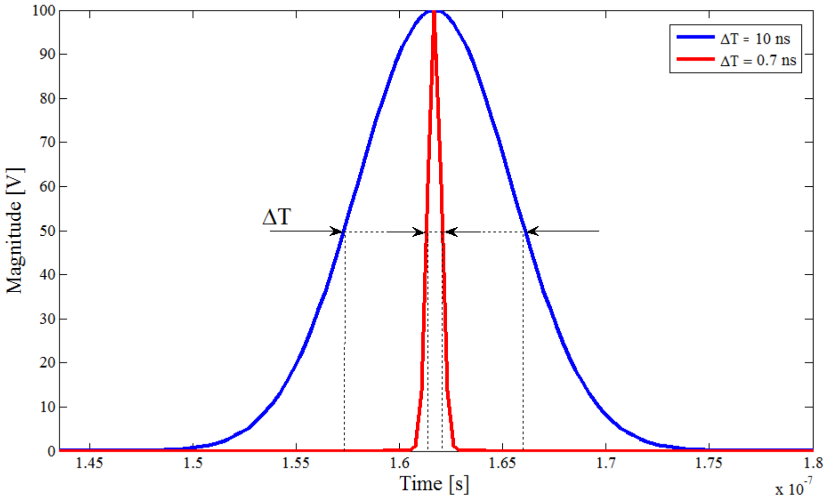

Figure 2.6. *Two pulse generators with different pulsewidth.*

The effect of the pulsewidth on the PEA output signal is shown in Figure 2.7, where the negative and positive peaks are due to the negative and positive surface charges, respectively. The red profile is obtained by using *ΔT* = 0.7 ns, while for *ΔT* = 10 ns the charge distribution is depicted by the blue line. In the first case, the negative peak magnitude is around 0.9 mV and the positive one is almost 0.3 mV. In the second case, in which the wider pulse is applied, the magnitude of both peaks increase significantly.

As regard the resolution, considering that the interfacial charge occupy infinitesimal space, it is possible to notice that the better profile is obtained by the narrow pulse.

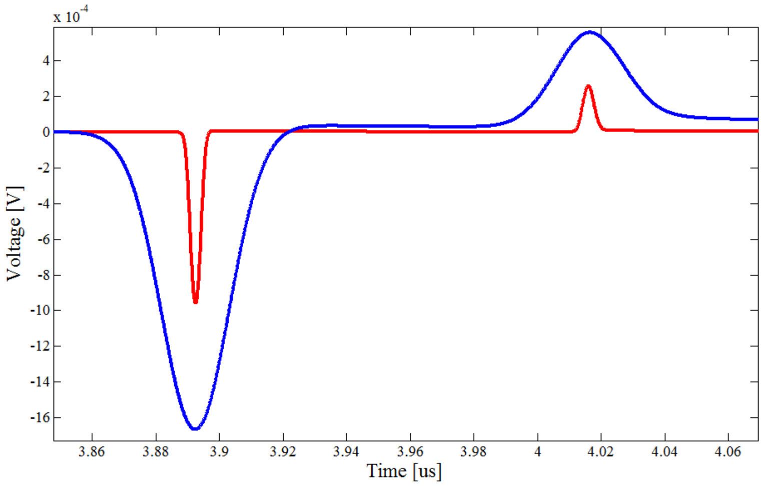

Figure 2.7. *Simulation results. The blue profile is referred to the PEA output signal obtained by applying the wider pulse. While the red profile is obtained by the narrow pulse.*

The expression explaining the correlation between the output signal magnitude and d_{SE} has been already reported in equation (2.44). While the spatial resolution Δs depending on the pulse width Δt is given as:

$$\Delta s = v_a \Delta t \tag{2.45}$$

where v_a is the sound velocity of the dielectric material under test.

Considering the same values of v_a and pulse voltage magnitude (because this parameter affects the output signal magnitude), based on the above described, the following summary table can be obtained:

Table 2.1. *Dependence of spatial resolution and output signal magnitude on the transducer thickness and pulse voltage width.*

Parameters	**Transducer thickness d_{SE}**		**Pulse voltage width Δt**	
	Thinner	***Thicker***	***Narrower***	***Wider***
Spatial resolution	Improve	Worsen	Improve	Worsen
Output signal magnitude	Lower	Higher	Lower	Higher

Because it is possible to increase the transducer output signal by amplifiers, the parameters d_{SE} and Δt are selected with the purpose to obtain the best spatial resolution values. Therefore d_{SE} and Δt should be selected thin and narrow, respectively. An equation useful for the choice of the transducer thickness by taking into account also Δt is given as:

$$d_{SE} \leq \Delta t \cdot v_{PVDF} \tag{2.46}$$

If equation (2.46) is satisfied the best spatial resolution of the PEA system is obtained.

In the commercial PEA cell, typical values of *Δt* are in the range 547 ns. This means that for a transducer made of PVDF material, with speed of sound v_{PVDF} = 2260 m/s, its thickness should be chosen less than 15 μm. However the most common commercial available PVDF sensor thicknesses in the market are 9 μm, 28 μm, 52 μm and 110 μm. Therefore the first one is that meets equation (2.46).

Another important aspect that should be considered in the transducer thickness choice is that the wave propagation time (τ_{SE}) from one side to the other side of its is about the same with the pulsewidth *Δt*. For a 9 μm thick transducer the τ_{SE} ~ 4 ns, which is close to *Δt* = 5 ns. Therefore the typical thickness adopted, in the PEA cell for flat specimen, is 9 μm.

2.7 Output signal of the amplifier

Considering that the magnitude of the piezoelectric sensor output signal is very small, an amplifier is used in order to increase the voltage level.

The linked between piezoelectric transducer and amplifier can be represented as an RC high-pass filter. Where *C* is the capacitance of the transducer and *R* the input resistance of the amplifier, as shown in Figure 2.8. The transfer function *W* of this system is reported in equation (2.47).

$$W(f) = \frac{j2\pi f CR}{1 + j2\pi f CR} \tag{2.47}$$

Where f is the frequency.

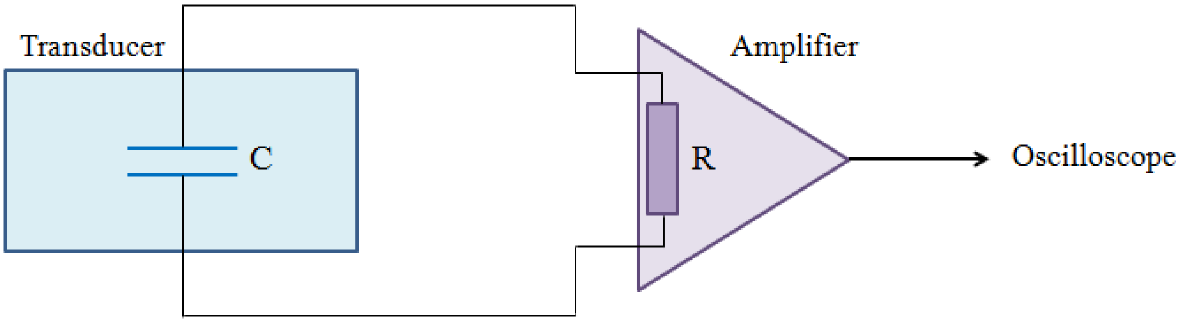

Figure 2.8. *Equivalent circuit of the PEA detection system.*

By taking into account the typical values of *R* and *C*, the cutoff frequency of this filter, which is calculated as $1/2\pi RC$, results under 100 Hz. Furthermore, considering the thicknesses and the sound velocity of the typical dielectric materials tested with the PEA cell, the lowest frequency component of the acoustic wave is in the order of MHz. However, this latter value is greater than the cutoff frequency and hence the system composed by transducer and amplifier is able to transmit the acoustic waves.

The output signal of the amplifier, $V_{out}(t)$, is given by:

$$V_{out}(t) = WGV_{PVDF}(t) = WG\frac{P_c d_{SE}}{\varepsilon} p_{tot}(t) \tag{2.48}$$

where *G* is the gain of the amplifier [51].

It is to be noted that, the voltage signal calculated in equation (2.48), which represents the output signal of the PEA cell, is proportional to the pressure wave $p_{tot}(t)$. The latter contains information on the accumulated charge and therefore $V_{out}(t)$ results proportional to the surface and space charges present in the interfaces and bulk of the specimen under test.

Finally, the signal $V_{out}(t)$ is visualized in the oscilloscope and sent to the computer to be processed.

2.8 Deconvolution process

As explained in the previous paragraph, the linked between transducer and amplifier leads the charge output signal to pass through a high-pass filter. This involves signal distortion that can be corrected by deconvolution technique.

Considering the same specimen of Figure 2.5, the ideal output charge profile should be like that of Figure 2.8. Instead, due to the presence of the amplifier after the transducer, and thus the presence of an RC filter, the real output signal results distorted, as shown in Figure 2.9. As can be seen in this last figure, the distortion cause a signal which seems an accumulation of charge with opposite polarity compared to that accumulated in the negative electrode/sample interface (red circle on the left side of Figure 2.9). Also in the space comprised between the two main peaks the signal is different from zero, as in the case of space charge accumulation in the bulk of the sample. While, the red circle on the right of the same figure highlights the signal distortion after the main signal, therefore its correction can be avoided. In reality, after signal processing by means of deconvolution technique, the final space charge profile becomes very similar to that of Figure 2.8, in which between the main peaks, but also on the right of the positive one, the signal is equal to zero.

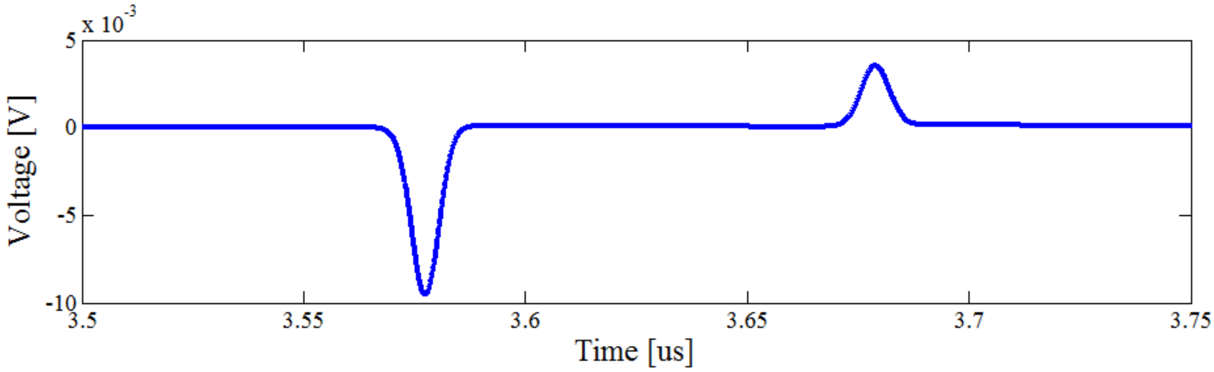

Figure 2.8. *Ideal charge profile detected by the piezoelectric transducer.*

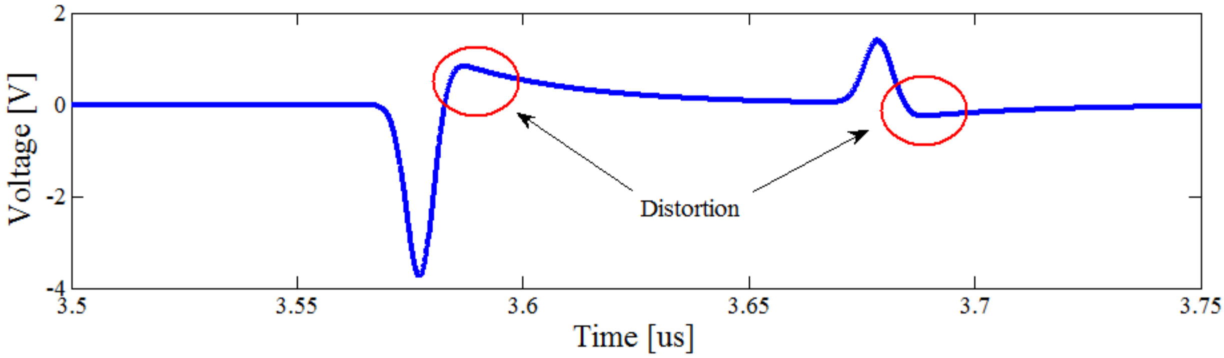

Figure 2.9. *Real output signal after amplification.*

The deconvolution technique proposed by Jeroense [123], which is the most used in PEA systems, allows to obtain the original signal $V_{dec}^{orig}(t)$ starting from the distorted signal detected at the oscilloscope $V_{det}(t)$, by means of the following equations:

$$V_{det}(t) = F^{-1}\left[V_{orig}(f) * H(f)\right] \tag{2.49}$$

$$V_{dec}^{orig}(t) = F^{-1}\left[\frac{V_{det}(f)}{H(f)}\right] \tag{2.50}$$

where F^{-1} is the inverse Fourier transformation. While $H(f)$ is the system response, such as the relation between the input and output of the PEA system, which means the relation between the real distribution of space charge $\rho(t)$ in the sample and the detected signal at the oscilloscope $V_{det}(t)$. If H is known, it is possible to compute the original signal by using the inverse system response H^{-1}.

In details, the system response H is calculated as explained below.

The signals $V_{det}(t)$, $\rho(t)$, the pressure signal $p(t)$, the pulse voltage $e_p(t)$ and the detection system response in time domain $h(t)$ are linked as:

$$V_{det}(t) = K\, h(t) \otimes e_p(t) \otimes \rho(t) \tag{2.51}$$

where K is a calibration factor. While the symbol $\otimes$ represents the convolution operation. The convolution between $h(t)$ and $e_p(t)$ is equal to the total system response $H(t)$. Therefore, in frequency domain, equation (2.51) can be rewritten as:

$$V_{det}(f) = K\, h(f)e_p(f)\rho(f) = kH(f)\rho(f) \tag{2.52}$$

As regard the original space charge distribution $\rho(t)$, it may be evaluated in frequency domain as well as in time domain by simple algebraic calculations, as shown below:

$$\rho(f) = \frac{1}{K}\frac{V_{det}(f)}{H(f)} \tag{2.53}$$

$$\rho(t) = \frac{1}{K}F^{-1}\left[\frac{V_{det}(f)}{H(f)}\right] \tag{2.54}$$

Once an electric signal V_{det} as a result of a known space charge distribution ρ is measured, the response function H can be calculate. The only space charge distributions that can be predicted exactly are the interfacial charges $\sigma^{+}$and σ^{-} according to equations (2.2) and (2.3). The surface charge σ^{-} is taken instead of σ^{+} because the acoustic signal of this charge has not experienced any attenuation and dispersion by the sample material.

For these reasons only the detected signal $V_{gr}(t)$, due to the accumulated charge in correspondence of the ground electrode interface and in a bulk material part $\rho_{gr}(t)$, will be taken into account.

Based on the above, from equation (2.52) the system response is given as:

$$H(f) = \frac{V_{det}(f)}{K\,\rho(f)} = \frac{V_{gr}(f)}{K\,\rho_{gr}(f)} \tag{2.55}$$

The surface charge is generally believed to be very thin, therefore $\rho_{gr}(f) = F[\sigma^{-}\delta(t)] = \sigma^{-}$ with $\delta(t)$ the impulse function. Assuming $K\sigma^{-} = K_1$, equation (2.55) becomes:

$$H(f) = \frac{V_{gr}(f)}{K\,\sigma^{-}} = \frac{1}{K_1}\,V_{gr}(f) \tag{2.56}$$

K_1 represents the ideal signal from the surface charge σ^{-}, which means without distortion due to RC filter. In this case the ideal signal is represented by a pulse which has approximately the same width as the earth electrode in $V_{det}(t)$ and has a height of one (which is usually much larger than the height of the electrode signal in $V_{det}(t)$).

In this way H has been obtained.

Considering that equation (2.50) needs $H^{-1}(f)$ instead of $H(f)$, the ideal signal is divided by the output signal V_{gr}, as follow:

$$H^{-1}(f) = \frac{K_1}{V_{gr}(f)} \tag{2.57}$$

Because the signal $H^{-1}(f)$ contains high frequency components, which cause distortion in the final deconvoluted signal $V_{dec}(t)$, a low pass Gaussian filter $G(f)$ is inserted with the aim to remove or attenuate these components.

Finally, according to equation (2.50), the signal $H^{-1}(f)$ is multiplied by the detected signal $V_{det}(f)$, and then F^{-1} is made in order to obtain the original charge profile $V_{orig}(t)$. Actually, the original signal is still not obtained because after F^{-1} of $[V_{det}(f)/H^{-1}(f)]$ the deconvoluted signal $V_{dec}(t)$ is an approximation of the real charge profile. This is due to the fact that the ideal signal K_1 was chosen with magnitude equal to one instead of the actual voltage. Therefore, to obtain the correct final value a correction factor K_{corr}, calculated as shown in equation (2.58) is needed.

$$K_{corr} = \frac{\max(|V_{dec}(t)|)}{max(|V_{det}(t)|)} \tag{2.58}$$

To acquire the correct original signal $V_{dec}^{orig}(t)$, $V_{dec}(t)$ is then divided by K_{corr}:

$$V_{dec}^{orig}(t) = \frac{V_{dec}(t)}{K_{corr}} \tag{2.59}$$

The schematic representation of the above described deconvolution technique is reported in Figure 2.10.

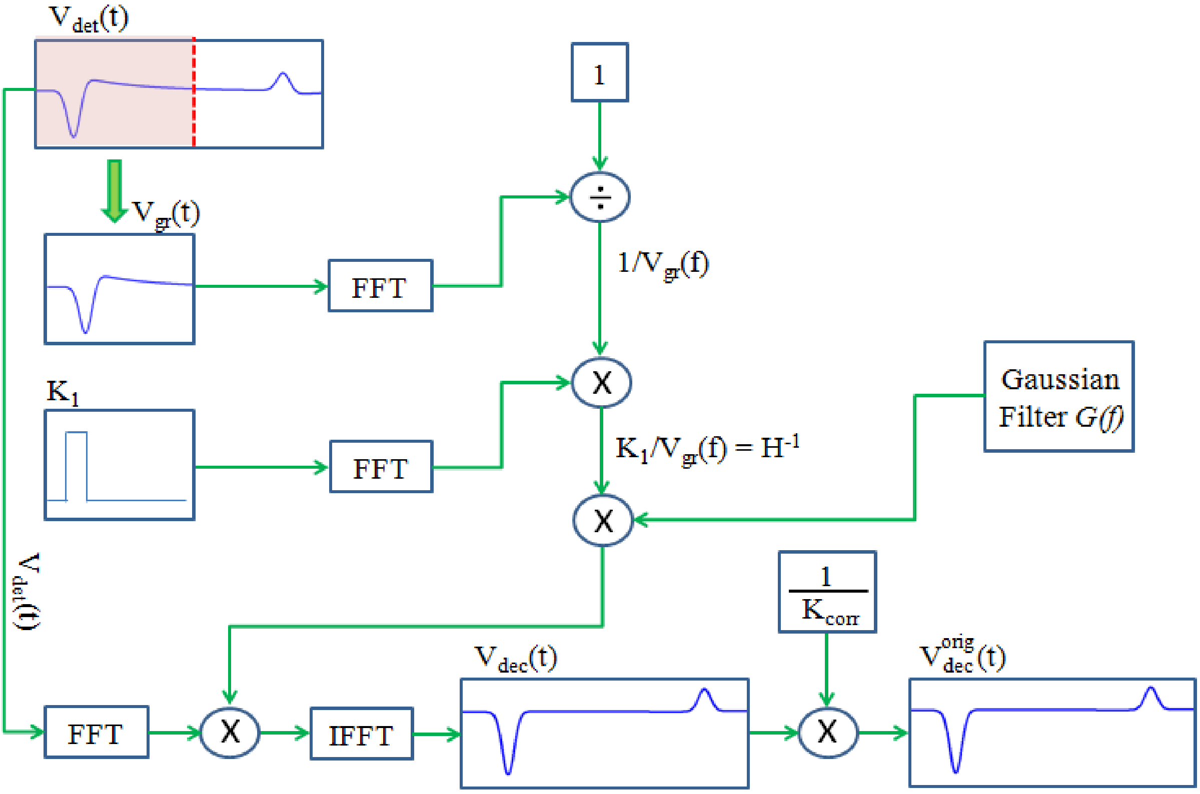

Figure 2.10. *Block diagram of deconvolution technique.*

2.9 Calibration process

The voltage signal after deconvolution process is still not a charge signal. This because $V_{dec}^{orig}(t)$

is in [mV], while the charge density $\rho(x)$ should be measured in [C/m^3]. Therefore a double calibration is needed, one to convert the magnitude [mV] into [C/m3] (y-axis calibration), and other one to convert the time t into the position x of the corresponding positive and negative peaks (x-axis calibration), as shown in Figure 2.11.

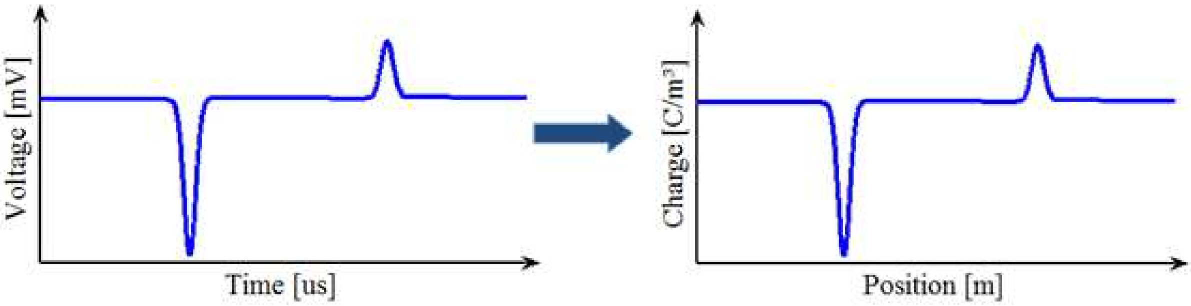

Figure 1.11. *Output PEA signal, before (on the left) and after (on the right) calibration procedure.*

In order to make x-axis calibration, the speed of sound of the sample material v_i must be known. Because it is also known the time axis of the deconvoluted signal (or original signal), the position of the two peaks can be found as:

$$position = v_i \cdot time \tag{2.60}$$

If the calibration procedure is correct, the distance between the two peaks should be equal to the sample thickness d_{Sa}.

Because the corresponding time of the negative peak depends on the ground electrode thickness d_{GR} and its speed of sound v_{AL}, it is always different from zero. Therefore the abscissa value $t = 0$ should be imposed in correspondence of the negative peak maximum value, in order to visualize the distribution of charges between $x = 0$ and $x = d_{Sa}$.

For example, if the ground electrode is made of aluminum with v_{AL} = 6420 m/s and d_{GR} = 10 mm, while the sample is made of XLPE with v_{XLPE} = 2200 m/s and d_{Sa} = 0.3 mm, the calculated x-axis is that of Figure 2.12a. As can be seen the position of the charges is not easy to understand. While, as shown in Figure 2.12b, in which the time is shifted, the x-axis gives directly the correct position of the charges located within the sample.

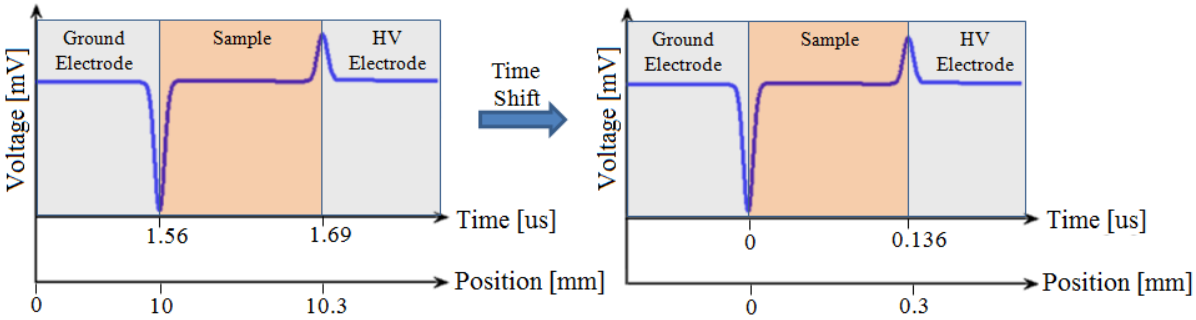

Figure 2.12. *Calibrated PEA output signal. a) x-axis not shifted, b) x-axis shifted in order to highlight the sample thickness.*

As regard the calibration along the y-axis, and thus the conversion from mV to C/m³, a calibration factor K_{cal} (different from that of equation (2.52)) should be determined. The voltage PEA output signal after deconvolution $V_{dec}^{orig}(t)$ can be written as a function of position x after the x-axis calibration, $V_{dec}^{orig}(x)$. In the latter, the detected charges $\rho(x)$ and K_{cal} are linked by the following relationship:

$$V_{dec}^{orig}(x) = K_{cal}\,\rho(x) \tag{2.61}$$

Therefore K_{cal} is given as:

$$K_{cal} = \frac{V_{dec}^{orig}(x)}{\rho(x)} \tag{2.62}$$

The determination of K_{cal} needs the knowledge of $V_{dec}^{orig}(x)$ and $\rho(x)$. The first one is already known, while the second one must be evaluated.

The only known charge density is the surface charge in correspondence of the electrodes. Because the detected signal due to positive surface charge is attenuated compared to the real accumulated charge, the negative surface charge will be taken into account for calibration process. The latter is calculated as follow.

Considering that the applied constant stress V is known, as well as the sample thickness d_{Sa}, the electric field E within the sample can be calculated as:

$$E = \frac{V}{d_{Sa}} \tag{2.63}$$

Without internal space charge in the sample the electric field distribution is the same between the electrodes, therefore by using equation (2.3) $\sigma^{-} = \varepsilon_0 \varepsilon_r E$, in which the permittivity ε_r of the sample is also known, the negative surface charge is obtained.

After that, equation (2.62) can be rewritten as:

$$K_{cal} = \frac{\int_{x_a}^{x_b} V_{dec}^{orig}(x)dx}{\sigma^{-}} \tag{2.64}$$

where x_a and x_b are the start and end point of the negative peak in $V_{dec}^{orig}(x)$.Therefore the integral in equation (2.64) represents the area of the ground electrode in $V_{dec}^{orig}(x)$, which is related to the negative surface charge density.

After K_{cal} is known, the y-axis of $V_{dec}^{orig}(x)$ can be calibrated and the space charge profile obtained by using the following equation:

$$\rho(x) = \frac{V_{dec}^{orig}(x)}{K_{cal}} \tag{2.65}$$

In order to verify the correct y-axis calibration, starting from the obtained charge density with equation (2.65), the electric field $E(x)$ and voltage $V(x)$ distributions, calculated with equations (2.66) and (2.67), should be the same as those applied (see equation 2.63).

$$E(x) = \frac{1}{\varepsilon_0 \varepsilon_r} \int_0^d \rho(x)dx \tag{2.66}$$

$$V(x) = -\int_0^d E(x)dx \tag{2.67}$$

The final charge pattern, calibrated both along *x* and *y* axis is that on the right of Figure 2.11.

It is important to highlight that the calibration as well as the deconvolution procedures must be made in a specimen without space charge. This means that the reference signals which should be taken into account for the mentioned procedures are those acquired in the first instants of measures.

This because after a certain time space charge accumulation occurs in the sample, which could influence the interfacial charges at the electrodes. Therefore became difficult the evaluation of the negative surface charge σ^{-}.

Chapter 3
Modeling of the PEA Cell

In this chapter, the PEA cell modeling approach used in this thesis is presented. The approach is based on the voltage-force and current-velocity analogies, which allows that each component of the PEA cell can be modeled as a lossy transmission line.

In Paragraph 3.4, the Telegraphist's equations for a transmission line have been obtained. Furthermore, the Finite Difference Time Domain (FDTD) method is used to simulate the electric (or acoustic) waves behavior within the series connected electric transmission lines (or PEA cell component).

In the subsequent paragraphs, all the details of the developed model, such as node equations, boundary conditions, setting of simulation time, etc. are presented and discussed.

An example of dynamic simulation, which allows to visualize the waves behavior in real time, is also proposed. Finally, the employed transducer model, implemented in Simulink environment, is described.

The PEA cell model has been implemented in Matlab environment and the pseudocode is reported in Appendix A.

3.1 The PEA cell

The theoretical aspects of the PEA method have been widely described in the previous chapter, while the block diagram of its working principle has been reported in Figure 1.8. Actually, compared to the latter figure, when measurements are made by the PEA cell, a sheet of semiconductor material with similar acoustic impedance of the sample under test, is placed between the high voltage electrode and the sample, with the aim to improve the acoustic matching.

The system consisting of the three electrodes (HV, ground and bottom), semiconductor layer, sample, sensor and absorber constitutes the acoustic circuit of the PEA cell. While the system, composed of resistance R, capacitance C, high voltage generator V_{dc}, pulse generator $e_p(t)$ and amplifier, constitutes the electrical circuit of the PEA cell. The entire system, which represents the PEA cell, is reported in Figure 3.1 [124].

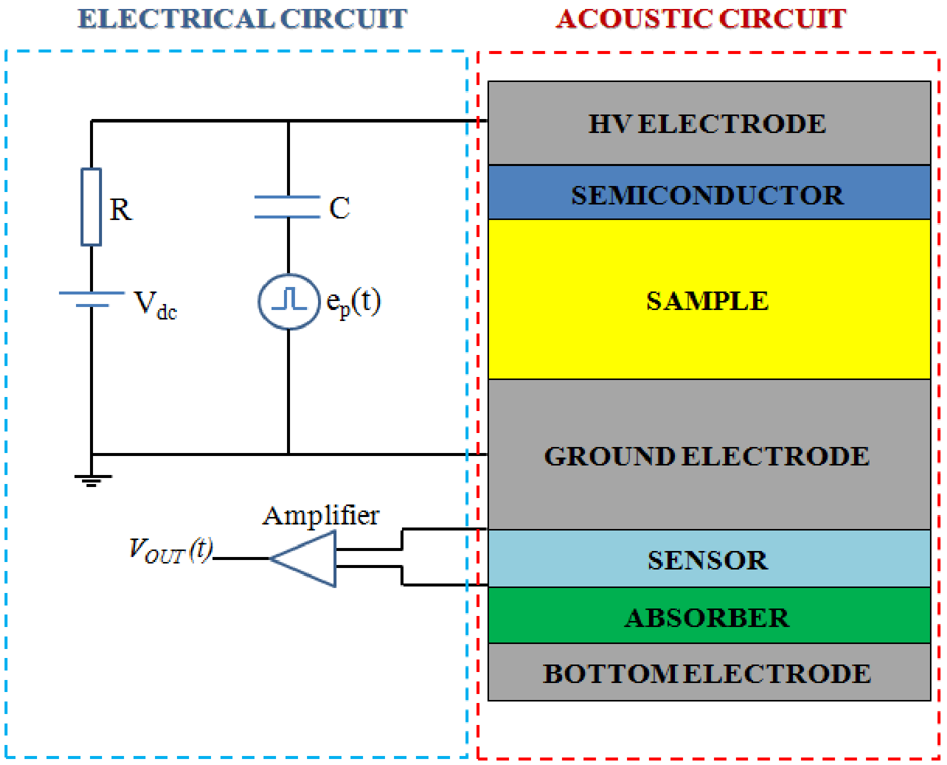

Figure 3.1. *Block diagram of the PEA cell. The electrical and acoustic circuits are highlighted by the blue and red dashed boxes, respectively.*

3.2 Motivation of the work

One of the most relevant issues in the PEA measurements is the correct interpretation of the output signal. The latter, in case of a single layer specimen and in absence of space charges, is constituted by only two peaks due to the accumulated surface charge in both electrodes/sample interfaces. This corresponds to the ideal case, in which the positive and negative peaks are separated and no signal is present between them (see Figure 2.8). In reality, as explained in Chapter 2, due to reflections of acoustic waves, false signals may appear between the two main peaks and thus the output signal interpretation becomes difficult. Considering that the acoustic part of the PEA cell is the sole responsible of wave reflections, in this work, only the acoustic circuit is taken into account (the pulse generator, belonging to the electrical part, affects only the magnitude of the output signal and the measurement resolution).

Based on the considerations above, the developed model is useful to properly size each PEA cell component in order to avoid reflected waves in the main signal and obtain a clear output charge profile.

3.3 Modeling approach

Considering a sample of dielectric material with only accumulated surface charges, the generated acoustic pressure waves propagate both in forward (toward the sensor) and opposite direction (toward the HV electrode), as shown in Figure 3.2. The pressure waves that travel in opposite directions are reflected in the sample/HV-electrode interface and come back to the sensor. These waves, as well as the other reflected waves between the ground electrode and the absorber are also sensed by the transducer. For these reasons all the acoustic waves propagating in both directions are taken into account into the model, unlike [124], in which only the acoustic waves that propagate in forward direction were considered.

Even if the semiconductor layer has been considered in the developed model, in order to better visualize the wave reflections in correspondence of the HV-electrode/sample interface, the same layer has not been inserted in Figure 3.2 as well as in the other figures in which the waves behavior is depicted.

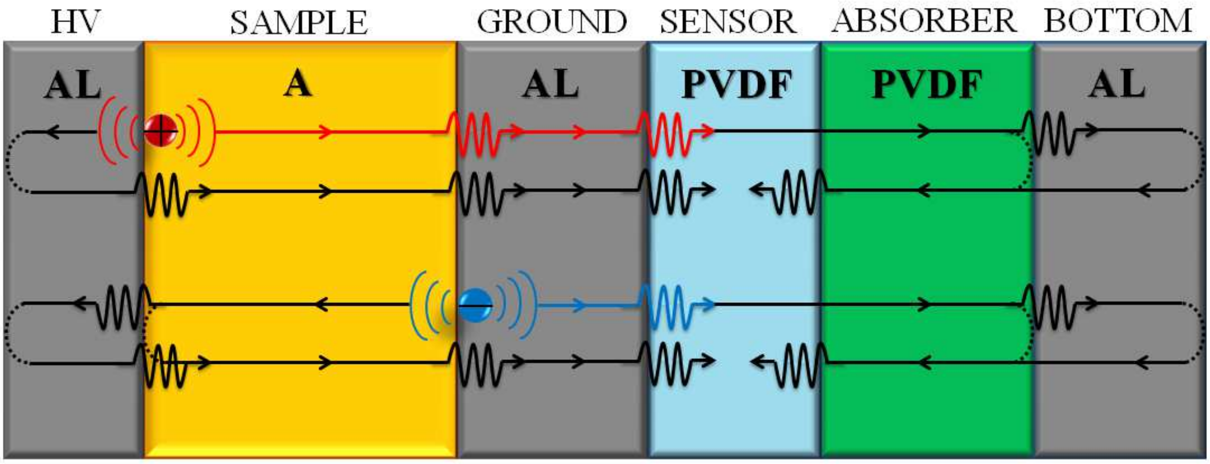

Figure 3.2. *Acoustic pressure wave propagation within the PEA cell. The red and blue waves propagate in forward direction just after being generated. While the black waves reach the transducer after being reflected.*

The acoustic pressure waves depicted in figure 3.2. propagate in the medium according to equations involving mechanical quantities such as force (or pressure) and velocity. Considering the analogy between force-voltage and velocity-current, pressure waves can be easily described by electrical quantities [125]. Moreover, each PEA cell component characterized by a different material can also be described by electrical quantities, such as resistance R, inductance L, capacitance C and conductance G, defined per unit length.

These electrical quantities are calculated by using some material properties, such as: the density ρ of the material (in kilograms per cubic meter, kg/m^3), the acoustic velocity v (in meter per second, m/s), the attenuation coefficient due to viscous losses α (in Neper per meter, Np/m) and the attenuation coefficient α_{tc} due to thermal conductance (in Np/m). As a result, the following equations can be written:

$$R = 2\rho v A \alpha \tag{3.1}$$

$$L = A\rho \tag{3.2}$$

$$C = \frac{1}{A\rho v^2} \tag{3.3}$$

$$G = \frac{2}{\rho v A}\alpha_{tc} \tag{3.4}$$

where A is the area of cross section (in square meters, m^2) .

Therefore, each PEA cell component can be represented by a lossy transmission line, as shown in Figure 3.3. In which the length of each transmission line is equal to the thickness of the corresponding PEA cell component.

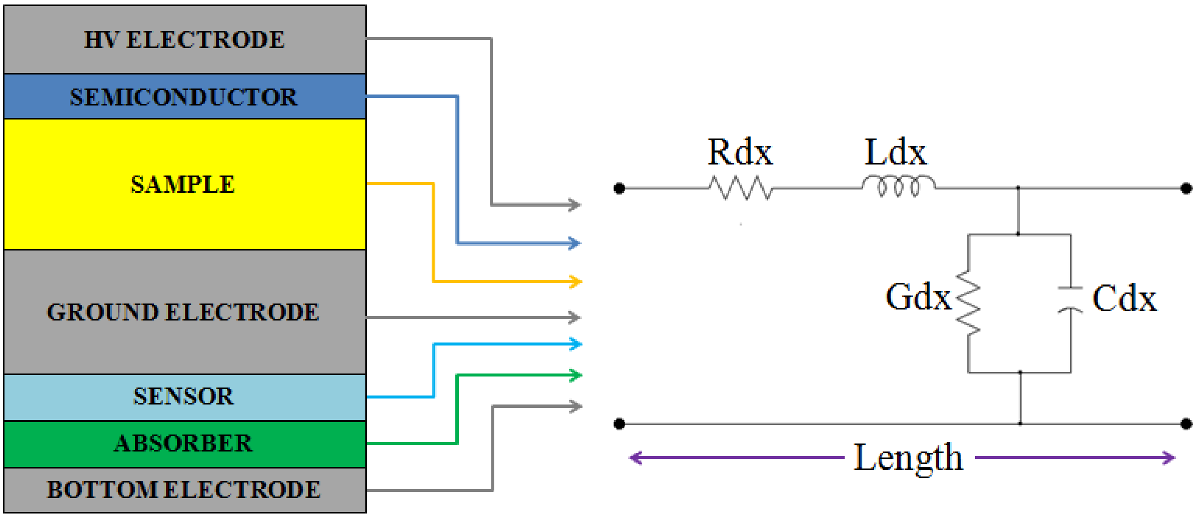

Figure 2.3. *Lossy transmission line used to describe each PEA cell component.*

Based on the above mentioned model, the propagation of acoustic waves within the PEA cell can be simulated as the electric waves propagation (voltage and current) on electric lossy transmission line, by using Telegraphist’s equations:

$$-\frac{\partial v(x,t)}{\partial x} = Ri(x,t) + L\frac{\partial i(x,t)}{\partial t} \tag{3.5}$$

$$-\frac{\partial i(x,t)}{\partial x} = Gv(x,t) + G\frac{\partial v(x,t)}{\partial t} \tag{3.6}$$

where $v(x,t)$ and $i(x,t)$ are the voltage and current waves, respectively. While, the transmission line parameters R, L, G and C are calculated as in equations (3.1-3.4).

3.4 Telegraphist's equations and FDTD method

In this paragraph the Telegraphist's equations, previously introduced, are described in details, starting from a typical schematization of an elementary section. Beyond this, the FDTD, used in this thesis to simulate the wave propagation within the PEA cell, is also described.

The elementary section of an electric line is shown in Figure 3.4.

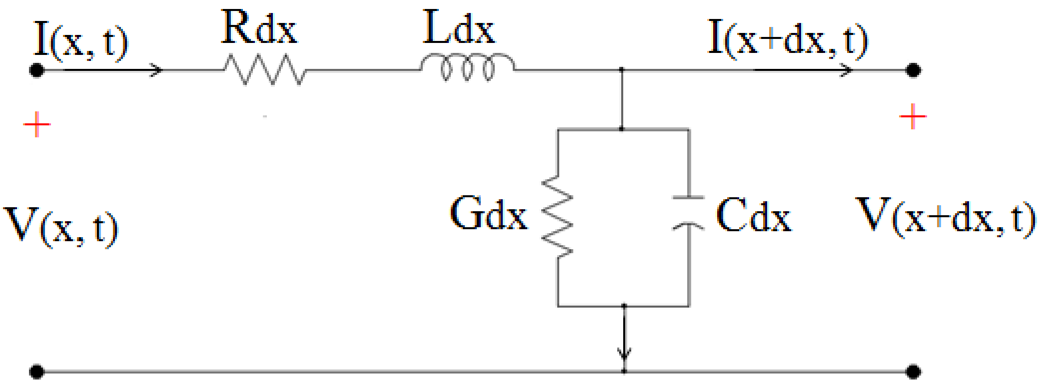

Figure 3.4. *Elementary section of an electric line.*

Where $V(x,t)$ and $I(x,t)$ are the input instantaneous voltage and current values of the chosen elementary section. While, $V(x+dx,t)$ and $I(x+dx,t)$ are the output voltage and current values of the same elementary section, where dx is the section length [126].

By applying the Kirchhoff's voltage law, the correlation between the input and output voltage of the elementary section can be determined as:

$$V(x,t) = Rdx \cdot I(x,t) + Ldx\frac{\partial}{\partial t} \cdot I(x,t) + V(x+dx,t) \tag{3.7}$$

With the following approximation:

$$V(x+dx,t) = V(x,t) + dV(x,t) \tag{3.8}$$

Equation (3.7) becomes:

$$-\frac{\partial}{\partial x}V(x,t)dx = Rdx \cdot I(x,t) + Ldx\frac{\partial}{\partial t}I(x,t) \tag{3.9}$$

Dividing all terms by dx, equation (3.9) can be rewritten as:

$$-\frac{\partial}{\partial x}V(x,t) = R \cdot I(x,t) + L\frac{\partial}{\partial t}I(x,t) \tag{3.10}$$

Likewise, the application of the Kirchhoff's current law provides the correlation between the input and output current of the elementary section:

$$I(x,t) = Gdx \cdot V(x+dx,t) + Cdx\ \frac{\partial}{\partial t}V(x+dx,t) + I(x+dx,t) \tag{3.11}$$

Similarly to that done for equation (3.7), equation (3.11) can be rewritten as:

$$-\frac{\partial}{\partial x}I(x,t) = G \cdot V(x,t) + C\frac{\partial}{\partial t}V(x,t) \tag{3.12}$$

Equations (3.10) and (3.12) are called Telegraphist's equations. If these two equations are solved by substitution method, a second order differential equation is obtained and thus two initial conditions are needed. Instead, by using numerical techniques, the resolution of a second order differential equation is avoided and the Telegraphist's equations could be simultaneously solved.

In this work, to calculate and simulate the Telegraphist's equations, and therefore to visualize the propagation of voltage and current in transmission line (or pressure and velocity within PEA cell), the FDTD method has been used. It is a finite differences technique in which the derivatives with respect to space x and time t are approximated by finite differences (equation (3.13) and (3.14)) applied in a spatial and temporal lattice.

$$\frac{\partial}{\partial t} \cong \frac{\Delta}{\Delta t} \tag{3.13}$$

$$\frac{\partial}{\partial x} \cong \frac{\Delta}{\Delta x} \tag{3.14}$$

Where Δt and Δx are the time step and the space step, respectively.

Initially, in the application of the FDTD algorithm, a lattice is defined [127].

The latter is a set of discrete points in space and time that samples the functions. This lattice is shown in Figure 3.5, in which the distance between two points in space Δx and in time Δt is fixed.

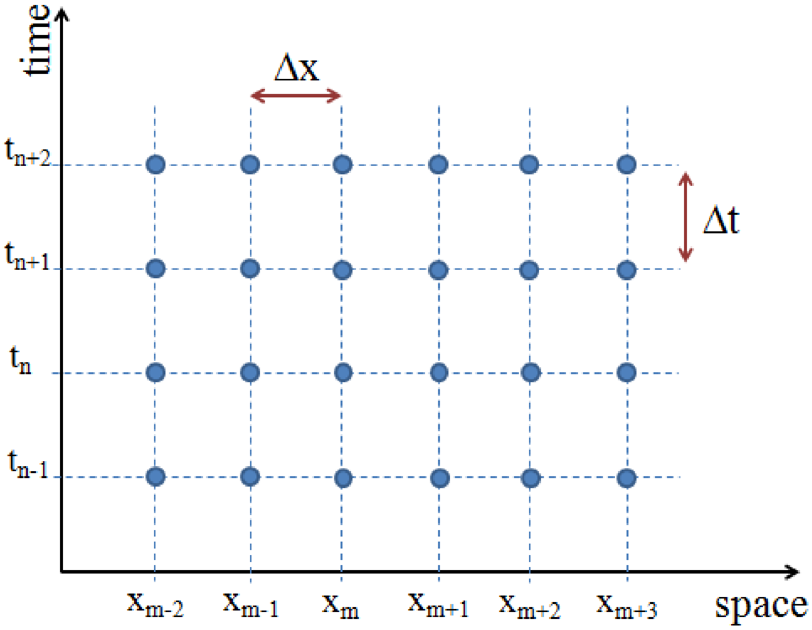

Figure 3.5. The lattice used in FDTD method.

The points in the lattice are identified by means of whole index m and n:

$$X_m = m\Delta x \tag{3.15}$$

$$t_n = n\Delta t \tag{3.16}$$

Based on the above, current and voltage variable in space and time can be written as I_m^n and V_m^n.

The spatial central finite difference formula for the voltage is defined as:

$$\frac{\partial}{\partial x}V(x,t) \cong \frac{V\left(x+\frac{\Delta x}{2},t\right)-V\left(x-\frac{\Delta x}{2},t\right)}{\Delta x} \tag{3.17}$$

By using the notation with index m and n, and taking into account that $\Delta x/2$ means half spatial step $(1/2)$, equation (3.17) can be rewritten as:

$$\frac{\partial}{\partial x}V(m\Delta x,n\Delta t) \cong \frac{V_{m+1/2}^{n}-V_{m-1/2}^{n}}{\Delta x} \tag{3.18}$$

Likewise, the temporal central finite difference formula for the current is given by:

$$\frac{\partial}{\partial t}I(x,t) \cong \frac{I\left(x,t+\frac{\Delta t}{2}\right)-I\left(x,t-\frac{\Delta t}{2}\right)}{\Delta t} \tag{3.19}$$

As it was done for the voltage formula, by inserting the indices m and n, equation (3.19) becomes:

$$\frac{\partial}{\partial t}I(k\Delta x,n\Delta t) \cong \frac{I_{m}^{n+1/2}-I_{m}^{n-1/2}}{\Delta t} \tag{3.20}$$

By means of finite difference technique described above, and thus introducing equations (3.18) and (3.20) in the Telegraphists' equation describing the voltage behavior (equation (3.10)), the latter can be rewritten as:

$$-\frac{V_{m+1/2}^{n}-V_{m-1/2}^{n}}{\Delta x}=R\cdot I_{m}^{n}+L\frac{I_{m}^{n+1/2}-I_{m}^{n-1/2}}{\Delta t} \tag{3.21}$$

As it can be seen in the equation above, the continue dependence of the voltage from the space x in equation (3.17) has been replaced by a discrete dependence from the index m. In equation (3.21), it is also possible to observe that the temporal index n appearing in the current expression is both entire I_m^n and shifted by half quantity $I_m^{n\pm 1/2}$. In this way, it will be difficult to solve this equation and therefore the current average at the instant n should be introduced, as shown in equation (3.22).

$$-\frac{V_{m+1/2}^{n}-V_{m-1/2}^{n}}{\Delta x}=R\cdot\frac{I_{m}^{n+1/2}+I_{m}^{n-1/2}}{2}+L\frac{I_{m}^{n+1/2}-I_{m}^{n-1/2}}{\Delta t} \tag{3.22}$$

The FDTD technique is based on explicit formulas in which the term more advanced in time $I_{m}^{n+1/2}$, is written as a function of others quantities. Therefore equation (3.22) can be rewritten as equation (3.23) and then dividing for $\left(\frac{L_m}{\Delta t}+\frac{R_m}{2}\right)$ and making same mathematical manipulations, thus obtaining equation (3.24).

$$I_{m}^{n+1/2}\left(\frac{L_m}{\Delta t}+\frac{R_m}{2}\right)=I_{m}^{n-1/2}\left(\frac{L_m}{\Delta t}-\frac{R_m}{2}\right)-\frac{1}{\Delta x}\left(V_{m+1/2}^{n}-V_{m-1/2}^{n}\right) \tag{3.23}$$

$$I_{m}^{n+1/2}=I_{m}^{n-1/2}\left(\frac{2L_m-R_m\Delta t}{2L_m+R_m\Delta t}\right)-\frac{2\Delta t}{2L_m\Delta x+R_m\Delta t\Delta x}\left(V_{m+1/2}^{n}-V_{m-1/2}^{n}\right) \tag{3.24}$$

In the same manner, starting from the second Telegraphists' equation describing the current behavior, the voltage term more advanced in time $V_{m}^{n+1/2}$ can be obtained as follows:

$$V_{m}^{n+1/2}=V_{m}^{n-1/2}\left(\frac{2C_m-G_m\Delta t}{2C_m+G_m\Delta t}\right)-\frac{2\Delta t}{2C_m\Delta x+G_m\Delta t\Delta x}\left(I_{m+1/2}^{n}-I_{m-1/2}^{n}\right) \tag{3.25}$$

By observing equations (3.24) and (3.25), it is possible to notice that the FDTD technique allows to obtain a new information at time $n+1/2$ as a function of other information detected in a previous time n and $n-1/2$. This information update method is called "LEAPFROG technique" [127-128].

As it can be seen in equations (3.24) and (3.25), the voltage terms are those at time n and its previous value $n-1/2$, respectively. Therefore from equation (3.24) it is difficult to solve equation (3.25) and vice versa. This happens because the first one needs entire n index, while the second equation needs half quantity of n index.

In the same way, for the current term which requires half n index in equation (3.24) and entire n index in the other one. Therefore the two equations are not easily simultaneously solvable. Because it is possible to evaluate current and voltage in different spatial and temporal times, this problem can be overcome by adopting two lattices, one for the current and one for the voltage, different to that proposed in Figure 3.5. The double lattice is reported in Figure 3.6, in which, as compared to the previous case, current and voltage are evaluated in a given time and at spatial points shifted by half quantity. By adding a half quantity $(+1/2)$ at each term of equation (3.25), the latter becomes:

$$V_{m+1/2}^{n+1} = V_{m+1/2}^{n}\left(\frac{2C_{m+1/2} - G_{m+1/2}\Delta t}{2C_{m+1/2} + G_{m+1/2}\Delta t}\right) - \\ - \frac{2\Delta t}{2C_{m+1/2}\Delta x + G_{m+1/2}\Delta t\Delta x}\left(I_{m+1}^{n+1/2} - I_{m}^{n+1/2}\right) \quad (3.26)$$

In this way, the current term in equations (3.26) can be calculated by using equation (3.24), and vice versa, each voltage term in equation (3.24) can be evaluated by equation (3.26). This happens because, in both equations, all voltage terms are described by entire n index and all current terms are described by half n index.

Equations (3.24) and (3.26) can be rewritten as equations (3.27) and (3.28).

$$I_m^{n+1/2} = P_m \cdot I_m^{n-1/2} + Q_m\left(V_{m-1/2}^{n} - V_{m+1/2}^{n}\right) \quad (3.27)$$

$$V_{m+1/2}^{n+1} = Y_{m+1/2} \cdot V_{m+1/2}^{n} + S_{m+1/2}\left(I_m^{n+1/2} - I_{m+1}^{n+1/2}\right) \quad (3.28)$$

Where:

$$P_k = \frac{2L_m - R_m\Delta t}{2L_m + R_m\Delta t} \quad (3.29)$$

$$Q_k = \frac{2\Delta t}{2L_m\Delta x + R_m\Delta t\Delta x} \quad (3.30)$$

$$Y_{m+1/2} = \frac{2C_{m+1/2} - G_{m+1/2}\Delta t}{2C_{m+1/2} + G_{m+1/2}\Delta t} \quad (3.31)$$

$$S_{m+1/2} = \frac{2\Delta t}{2C_{m+1/2}\Delta x + G_{m+1/2}\Delta t\Delta x} \quad (3.32)$$

In figure 3.6. below it is shown a double lattice. In this figure the spatial and temporal points describing the voltage are highlighted in red color, while the points referred to the current are depicted in green color.

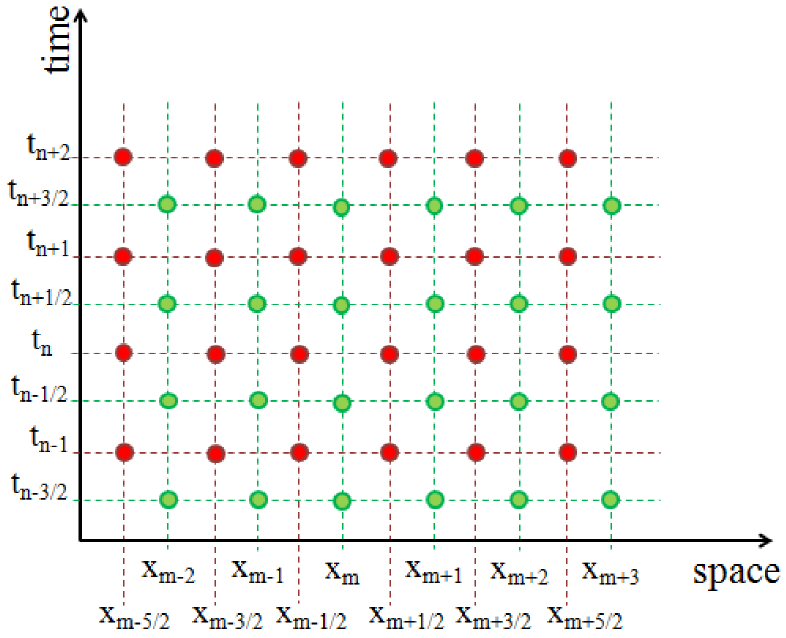

Figure 3.6. *The adopted double lattice.*

The solution of equations (3.27) and (3.28) is defined as a solution of a problem in which are defined the initial and boundary conditions. Therefore, the simulation is set according to the following steps:

1. Formulation of the problem, set spatial (M) and temporal (N) dimensions in a finite lattice. Where M and N are the upper limit of m and n employed in the equations previously described.
2. Set temporal initial conditions ($n = 0$) for current and voltage. Which means at time $t = 0$.
3. Update of the current at the time $n + 1/2$ and of the voltage at the state $n + 1$.
4. Evaluation of the phenomenon for a temporal increment.
5. Comparison between the simulated time n and the final time N.
    - If $n < N$ go back to point 3. Here, the real time propagation of acoustic wave can be visualized.
    - If n = N the simulation ends, and the final charge profile is obtained.

The flow chart of the developed model is reported in Paragraph 3.10, and further details are given in the following.

3.5 Setting of M and N dimensions

In the developed model, the choice of M and N dimensions has been made as follows.

Being M the number of discrete elements composing the sample and N the number of discrete elements spanned during the wave propagation.

Initially the spatial step Δx, named dz into the algorithm, has been set equal to $0.2 \cdot 10^{-5}$ in order to have a good compromise between spatial resolution and simulation time.

After that, the length of each PEA cell component has been divided by dz and then the calculation of M_x has been carried out as shown in equation (3.33) and in Figure 3.7, in which each spatial element is defined as m_x^i, where i is the element number and the footer x is the generic PEA cell component.

$$M_x = \frac{length\_x}{dz} \tag{3.33}$$

Therefore, the final M value (that describes the entire PEA cell) will be given by the sum of each M_x:

$$M = \sum_{x=1}^{n_x} M_x \tag{3.34}$$

Where n_x is the number of PEA cell components.

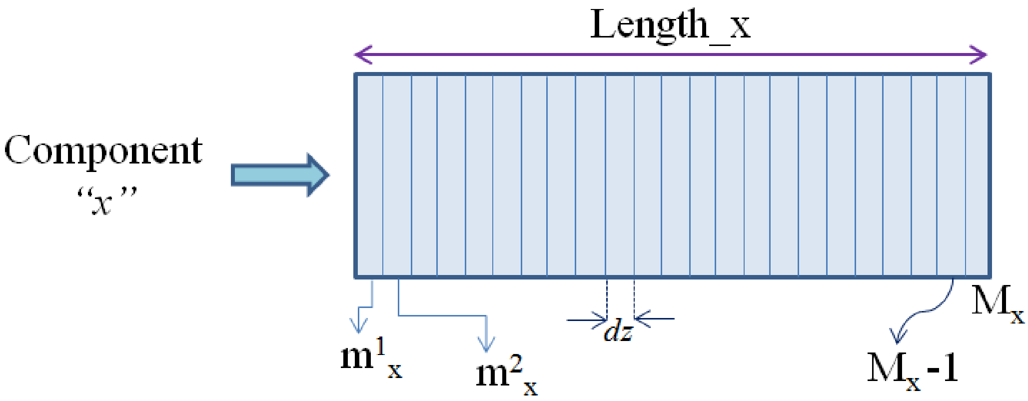

Figure 3.7. *Calculation of* $\boldsymbol{M_x}$ *for a generic PEA cell component.*

As regard the number of temporal samples N that are useful to describe the waves propagation within the PEA cell, the same number is calculated as shown in equation (3.35).

$$N = \sum_{x=1}^{n_x} \frac{\tau_x}{\Delta t_i} \tag{3.35}$$

Where τ_x is the time needed for a wave to come across a component x with material i and it is evaluated by using equation (2.20), while Δt_i is the step time for a material i calculated as later explained. By mathematical manipulation, it is possible to notice that $N = M$, as shown in equation (3.36):

$$N = \sum \frac{\tau_x}{\Delta t_i} = \sum \frac{\frac{length\_x}{v_i}}{\frac{dz}{v_i}} = \sum \frac{length\_x}{v_i} \cdot \frac{v_i}{dz} = \sum \frac{length\_x}{dz} = \sum M_c = M \tag{3.36}$$

Based on the formula above, to describe the waves propagation within the entire PEA cell, N should be chosen equal or greater than M. Typically, because it is interesting to visualize the wave starting from the dielectric material interfaces until the transducer surface or until the absorber (in order to visualize the reflected wave within it), N could be lower. However, the choice of N affects the simulation time, therefore it can be set differently based on the required simulation test.

Furthermore, for a fixed N, the simulation time depends on Δt_i and the latter is calculated as follows. Considering that the PEA cell is made up of components with different materials, and thus different sound propagation speed, Δt_i has been differentiated as shown in Figure 3.8. In the algorithm Δt_i is called dt_i, therefore, for each different material, the adopted time steps are:

- $dt_{AL} = \frac{dz}{v_{AL}}$ ⇒ for the electrodes made of aluminum material;
- $dt_A = \frac{dz}{v_A}$ ⇒ for the sample made of “A” material;
- $dt_{PVDF} = \frac{dz}{v_{PVDF}}$ ⇒ for the sensor and the absorber made of PVDF material.

The footer A in dt_A is referred to the general case. Into the algorithm it is replaced by XLPE or LDPE, depending on the sample under test.

The equations above are written according to the simulation stability condition, which will be explained in the next paragraph.

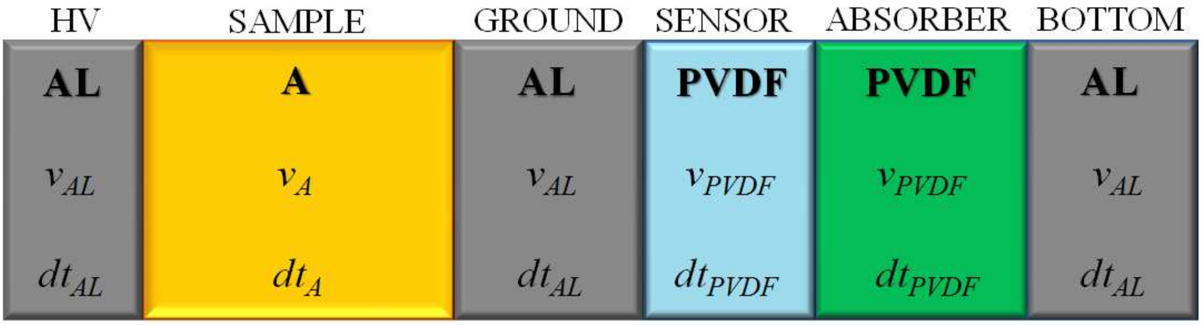

Figure 3.8. *Different steps time adopted into the model.*

As regards the semiconductor layer (not inserted in the figure above) placed between the HV-electrode and the sample, because it is made with similar material as the sample under test, the same step time dt_A has also been used for this component.

To better explain how the choice of N should be made, with the aim to obtain the correct simulation time, in Figure 3.9 six different examples of waves propagating within the PEA cell (with the same component dimensions of those used in the simulation tests described in the next chapter) are reported.

As an example, for a ground electrode made of aluminum with speed of sound v_{AL} = 6420 m/s and thickness d_{GR} = $23 \cdot 10^{-3}$ m (typical thickness value adopted in PEA cells), dt_{AL} is $3.11 \cdot 10^{-10}$ s and M = M_{GR} is set to 11500, where M_{GR} is the number of spatial elements calculated for the ground electrode.

For an acoustic wave starting from the sample/ground-electrode interface, named "*Wave 1*", the time to reach the sensor surface is t = 3.58 μs.

Into the algorithm, in order to simulate only this wave propagating within the ground electrode, N should be set equal to M and thus N = 11500. In this way, the simulation time is given by t = Ndt_{AL} = 3.58 μs as that requested for this type of test.

In another case, named "*Wave 2*" in Figure 3.9, the acoustic wave starts from the HV-electrode/sample interface, propagates up to the sensor. In this case the quantity M is set to M_{Sa} + M_{GR} spatial steps (in which M_{Sa} is the number of spatial elements of the sample).

If, as an example, the sample is $2 \cdot 10^{-4}$ m thick and the speed of sound in the medium constituting the sample is v_A = 1950 m/s (typical LDPE speed of sound) M_{Sa} = 100 and thus the number of samples should be set as N = M_{Sa} + M_{GR} = 11600. In this case, the simulated time is equal to t = $M_{Sa}dt_A$ + $M_{GR}dt_{AL}$ = 3.68 μs, which correspond to the time needed for the *Wave 2* to cross the sample and the ground electrode.

The case "*Wave 3*", instead, is referred to a wave that starts from the sample/ground-electrode interface and reaches the sensor after being reflected in the absorber/bottom-electrode interface.

In this case, the wave propagation is described by M = M_{GR} + M_{SE} + $2M_{ABS}$ spatial steps and N = M= 11755 temporal samples. The latter quantity is calculated by using the components dimensions reported in Figure 3.9. The simulation time results: t = $M_{GR}dt_{AL}$ + $M_{SE}dt_{PVDF}$ + $2M_{ABS}dt_{PVDF}$ = 3.84 µs, which is the time needed to the acoustic wave in case "Wave3" to reach the sensor after its reflection within the absorber.

The case "*Wave 4*" describes the same path of *Wave 3* apart from the fact that the starting point is in the HV-electrode/sample interface. This means that M_{Sa} must be added in the equation previously reported for *Wave 3*. Finally, *Wave 5* and *Wave 6* (with different starting points) are referred to the case in which, in the simulation, the reflections within the ground electrode should be analyzed.

For all of the simulation cases described above, the values of M and the corresponding values of N, that must be set in order to obtain the correct simulation time, for different simulation tests, are summarized in Table 3.1.

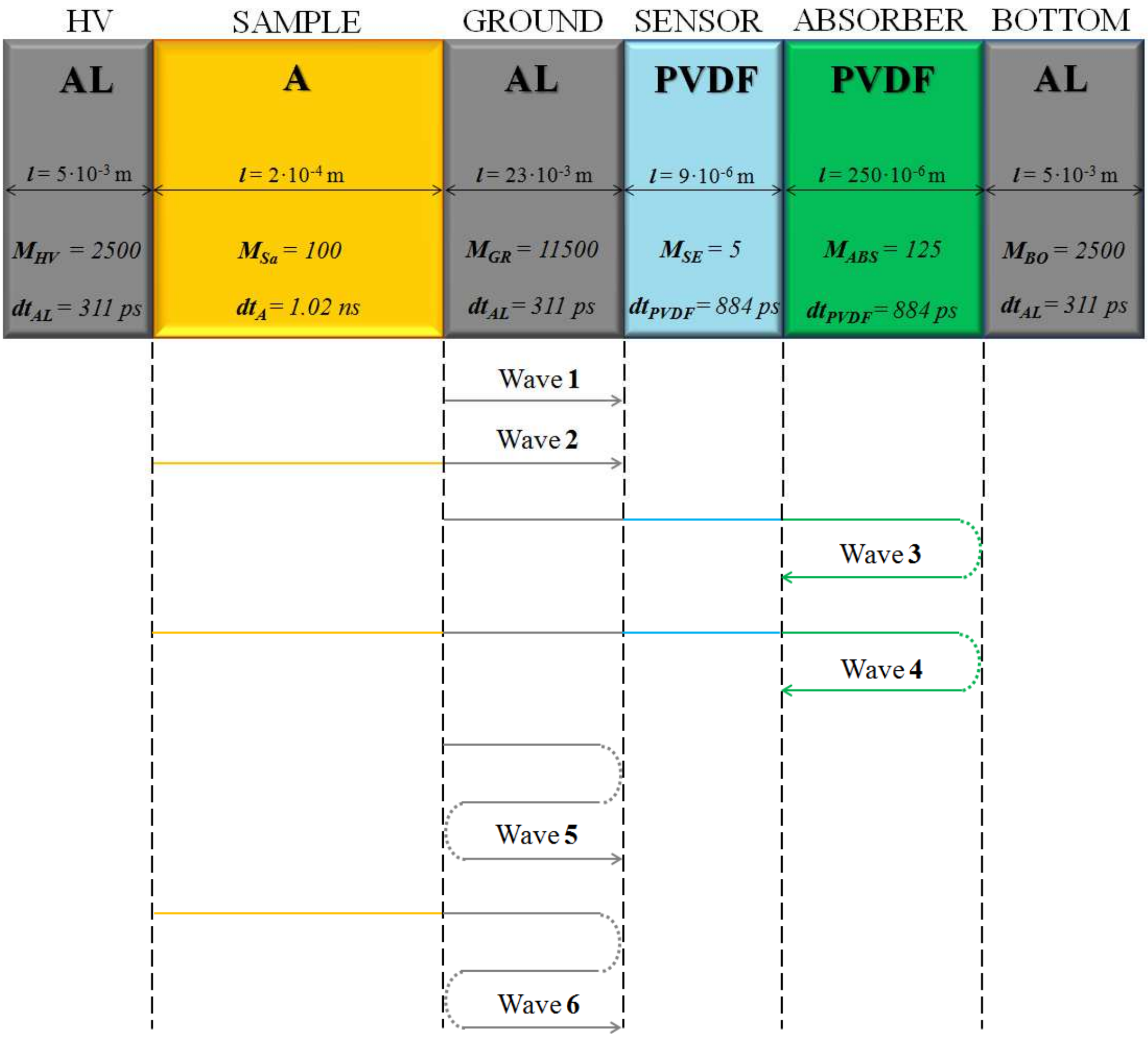

Figure 3.9. *Examples of wave propagation paths within the PEA cell.*

Table 3.1. *Values of M, N and corresponding simulation time for different simulation test.*

Wave	M	$N = \sum M_x$	Simulated time ($\boldsymbol{Ndt_i}$)
1	M_{GR}	11500	$M_{GR}\,dt_{AL}$ = 3.58µs
2	M_{Sa}+ M_{GR}	11600	($M_{Sa}\,dt_{A}$)+($M_{GR}\,dt_{AL}$) = 3.68µs
3	M_{GR}+ M_{SE} +2M_{ABS}	11755	($M_{GR}\,dt_{AL}$)+($M_{SE}\,dt_{PVDF}$) +2($M_{ABS}\,dt_{PVDF}$) =3.84µs
4	M_{Sa} + M_{GR} + M_{SE} +2 M_{ABS}	11855	($M_{Sa}\,dt_{A}$)+($M_{GR}\,dt_{AL}$)+($M_{SE}\,dt_{PVDF}$)+2($M_{ABS}\,dt_{PVDF}$) = 3.94µs
5	3 M_{GR}	34500	3($M_{GR}\,dt_{AL}$) = 10.7µs
6	M_{Sa} +3M_{GR}	34600	($M_{Sa}\,dt_{A}$)+3($M_{GR}\,dt_{AL}$) = 10.8µs

In other cases, in which the components thickness or the sample material (with different speed of sound) are different from those reported in Figure 3.9, M will also be different from the values of Table 3.1. Therefore, the setting of N must be made again, in order to obtain the correct simulation time.

3.6 Stability of the simulation

In the previous section, the Telegraphist's equations have been solved analytically (see equations (3.27) and (3.28)). In case of lossless transmission line, (with R = 0 and G= 0), the classic analytical solution of these equations is equal to:

$$v(x,t) = V_0^+ \cos(\omega t - \beta x + \phi^+) + V_0^- \cos(\omega t + \beta x + \phi^-) \tag{3.37}$$

$$i(x,t) = \frac{V_0^+}{Z_0}\cos(\omega t - \beta x + \phi^+) - \frac{V_0^-}{Z_0}\cos(\omega t + \beta x + \phi^-) \tag{3.38}$$

where, for both equations, the first term represents the propagation wave, while the second term describes the reflection wave [129]. The propagation constant is represented by β, while Z_0 is the characteristic impedance of the line calculated as $\sqrt{L/C}$.

By neglecting the reflected waves and assuming, for the propagation wave, the phase $\phi^+ = 0$ and the amplitude $V_0^+ = 1V$, equations (3.37) and (3.38) become:

$$v(x,t) = \cos(\omega t - \beta x) \tag{3.39}$$

$$i(x,t) = \frac{1}{Z_0}\cos(\omega t - \beta x) \tag{3.40}$$

After that, the two equations above are reported in the finite FDTD lattice of Figure 3.6 and therefore they can be rewritten as:

$$V_m^n = \cos(\omega\, n\, \mathit{\Delta} t - \beta\, m\, \mathit{\Delta} x) \tag{3.41}$$

$$I_m^n = \frac{1}{Z_0}\cos(\omega\, n\, \mathit{\Delta} t - \beta\, m\, \mathit{\Delta} x) \tag{3.42}$$

Considering the following assumptions:

$$a = \omega\, n\, \mathit{\Delta} t - \beta\, m\, \mathit{\Delta} x \tag{3.43a}$$

$$b = \omega\, \mathit{\Delta} t \tag{3.43b}$$

$$c = \beta\, \mathit{\Delta} x \tag{3.43c}$$

the updated voltage and current equations can be rewritten as:

$$\begin{aligned} V_{m+1/2}^n &= \cos\left[\omega n \Delta t - \beta\left(m + \frac{1}{2}\right)\Delta x\right] \\ &= \cos\left(\omega n \Delta t - \beta m \Delta x - \frac{\beta}{2}\Delta x\right) = \cos\left(a - \frac{c}{2}\right) \end{aligned} \tag{3.44}$$

$$\begin{aligned} V_{m+\frac{1}{2}}^{n+1} &= cos\left[\omega(n+1)\Delta t - \beta\left(m + \frac{1}{2}\right)\Delta x\right] \\ &= cos\left[\omega n \Delta t + \omega \Delta t - \beta m \Delta x - \frac{\beta}{2}\Delta x\right] = \cos\left(a + b - \frac{c}{2}\right) \end{aligned} \tag{3.45}$$

$$\begin{aligned} I_m^{n+\frac{1}{2}} &= \frac{1}{Z_0} cos\left[\omega\left(n + \frac{1}{2}\right)\Delta t - \beta m \Delta x\right] \\ &= \frac{1}{Z_0} cos\left(\omega n \Delta t + \frac{\omega \Delta t}{2} - \beta m \Delta x\right) = \frac{1}{Z_0}\cos\left(a + \frac{b}{2}\right) \end{aligned} \tag{3.46}$$

$$
\begin{aligned}
I_{m+1}^{n+\frac{1}{2}} &= \frac{1}{Z_0} cos\left[\omega\left(n+\frac{1}{2}\right)\Delta t-\beta(m+1)\Delta x\right] \\
&= \frac{1}{Z_0} cos\left(\omega n\Delta t+\frac{\omega\Delta t}{2}-\beta m\Delta x-\beta\Delta x\right)=\frac{1}{Z_0}\cos\left(a+\frac{b}{2}-c\right)
\end{aligned}
\tag{3.47}
$$

Therefore, by taking into account equations (3.44 – 3.47) and considering a lossless transmission line, which means that the conductance *G* is set to *0* and thus the parameter *Y = 1* and $S=\Delta t/C\Delta x$ (see equations (3.31) and (3.32)), equation (3.28) becomes:

$$
\cos\left(a+b-\frac{c}{2}\right)=1\cdot\cos\left(a-\frac{c}{2}\right)+S\frac{1}{Z_0}\left[cos\left(a+\frac{b}{2}\right)-cos\left(a+\frac{b}{2}-c\right)\right] \tag{3.48}
$$

In order to obtain the stability or convergence of the simulation, the second term of equation (3.48) must not exceed the maximum value assumed by the first member.

Considering that the parameters a, b and c are real numbers, the left term of equation (3.48) is always delimited in the interval [-1, 1], thus its maximum value is equal to 1. In the same equation, due to the fact that the constant term S depends on the capacitance to ground which can be highly variable, its value is arbitrary. Therefore the second term on the right can take different values as compared to the value taken by the first term.

In this case the error accumulates quickly in the simulation and the system becomes instable or divergent. In the light of this, to avoid simulation instability problem the time step Δt must be chosen appropriately, on the basis of a fixed Δx value.

As an example, if the first member, $\cos(a+b-c/2)$, assumes its maximum value and the first term at second member, $\cos(a-c/2)$, is equal to -1, on the basis of the stability condition, equation (3.48) can be rewritten as:

$$
1\geq -1+S\frac{1}{Z_0}\left[cos\left(a+\frac{b}{2}\right)-cos\left(a+\frac{b}{2}-c\right)\right] \tag{3.49}
$$

By inserting the expression of Z_0 and S previously reported in this paragraph, and if the term in square brackets takes the maximum allowed value for the simulation stability, such as 2, equation (3.49) becomes:

$$
1\geq -1+\frac{\Delta t}{C\Delta x}\frac{1}{\sqrt{L/C}}\cdot 2 \tag{3.50}
$$

Through the following mathematical steps:

$$2 \geq \frac{\Delta t}{C\Delta x}\frac{1}{\sqrt{L/C}} \cdot 2 \rightarrow 1 \geq \frac{\Delta t}{C\Delta x}\sqrt{\frac{C}{L}} \rightarrow 1 \geq \frac{\Delta t}{C\Delta x}\sqrt{\frac{C}{L}\frac{C}{C}} \rightarrow 1 \geq \frac{\Delta t\, C}{C\Delta x}\sqrt{\frac{1}{LC}} \\ \rightarrow 1 \geq \frac{\Delta t}{\Delta x} v_T \tag{3.51}$$

the final relationship, which must be taken into account to obtain the stability condition for the simulation, is given by:

$$\mathit{\Delta} t \leq \frac{\Delta x}{v_T} \tag{3.52}$$

where v_T calculated as $\sqrt{1/LC}$ is the waveform’s propagation speed in the transmission line. If equation (3.52) is satisfied, the simulation results stable. The obtained stability condition is easily understandable, in fact it is impossible to increase the time step $\mathit{\Delta} t$ over the time needed for the wave to cross a spatial step Δx of the lattice.

3.7 Boundary conditions

In Telegraphist’s equations solution, the boundary conditions can be determined by knowing the current or voltage values assumed at the ending parts of a transmission line. This boundary condition is called *constraint of Dirichlet* and is the most simple to apply. For example, if the transmission line ends with a short-circuit the boundary condition is fixed by setting to zero the voltage value:

$$V_{m+1/2}^{n} = 0 \tag{3.53}$$

In other cases, instead, when the transmission line ends with a open-circuit, the Neumann boundary condition can be applied. In this case the limit is imposed in the temporal derivate and thus the boundary condition can be written as:

$$V_{m+1/2}^{n} = V_{m-1/2}^{n} \tag{3.54}$$

In our case, a resistance with high value (~1MΩ) has been inserted in both ends of the PEA cell and thus the equation describing the open circuit condition has been applied.

3.8 Node equations

In correspondence of the nodes between two PEA cell components connected in series, the continuity of current and voltage waves is imposed as shown in equations (3.55) and (3.56).

$$IL_x(M_x) = IL_{x+1}(m^1_{x+1}) \tag{3.55}$$

$$VL_x(M_x) = VL_{x+1}(m^1_{x+1}) \tag{3.56}$$

Where the first term of the above equations is referred to the current and voltage values assumed in the last spatial element of the generic component x, before the node. While the second member is referred to the values assumed in the first spatial element of the next component $x + 1$ (which is contact with the component x), after the node. The components x and $x + 1$, and their spatial elements are depicted in Figure 3.10.

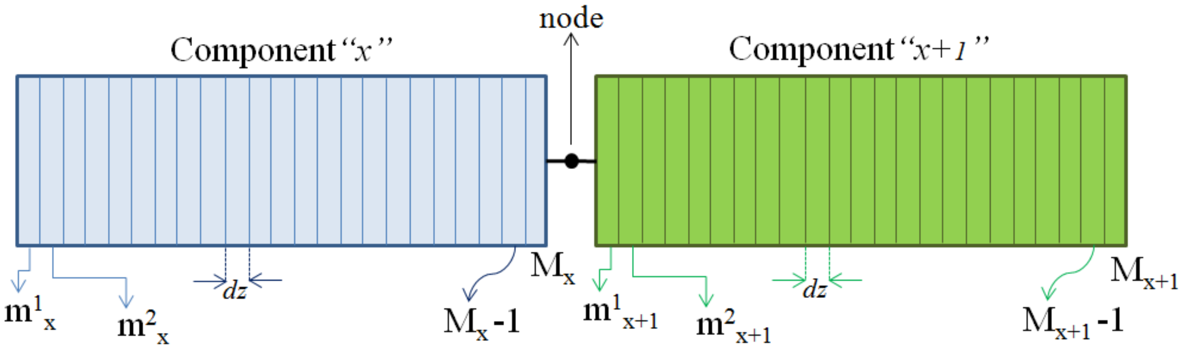

Figure 3.10. *Connection between two generic PEA cell components and related spatial elements*

By means of equation (3.27), which describes the current wave behavior from m_x = 1 to m_x = M_x – 1, the second member of equation (3.55) is evaluated and thus the continuity condition can be easily determined. As regard the other continuity condition of equation (3.56), none of the members are provided by equation (3.28). This because this last one describes the voltage wave behavior from m_x = 2 to m_x = M_x – 1, while the request voltage values in equation (3.56) are referred to the spatial element m_x = 1 and m_x = M_x. However, another equation can be written to solve equation (3.56) and is given by:

$$VL_x(M_x) = Y_{x,x+1} \cdot VL_x(M_x) + S_{x,x+1} \cdot (IL_x(M_{x-1}) - IL_{x+1}(m_{x+1}^1)) \tag{3.57}$$

Where $Y_{x,x+1}$ and $S_{x,x+1}$, refer to the node between the components x and $x+1$ and are calculated as:

$$Y_{x,x+1} = \frac{\left[2\frac{C_x(m_x^1) + C_{x+1}(m_{x+1}^1)}{2}\right] - \left[\frac{G_x(m_x^1) + G_{x+1}(m_{x+1}^1)\Delta t_x}{2}\right]}{\left[2\frac{C_x(m_x^1) + C_{x+1}(m_{x+1}^1)}{2}\right] + \left[\frac{G_x(m_x^1) + G_{x+1}(m_{x+1}^1)\Delta t_x}{2}\right]} \tag{3.58}$$

$$S_{x,x+1} = \frac{2\Delta t_x}{2\left[\frac{C_x(m_x^1) + C_{x+1}(m_{x+1}^1)}{2}\right]\Delta x + \left[\frac{G_x(m_x^1) + G_{x+1}(m_{x+1}^1)}{2}\right]\Delta t \Delta x} \tag{3.59}$$

3.9 Pulse sources

As previously explained, acoustic waves are generated by charges vibration due to the applied pulse electric field. According to the pressure-voltage analogy, the generation of an acoustic pressure wave can be modeled by using a voltage pulse source V_{pulse}. The latter is characterized by a waveform equal to that of the external pulse generator $e_p(t)$, which in the ideal case is approximated by the Gaussian pulse with width in the range of nanoseconds, as shown in Figure 3.11. The implemented equation, used to generate the requested pulse source is given by:

$$V_{pulse} = A\, e^{\frac{-(n-\alpha)^2}{\beta}} \tag{3.60}$$

Where A is the magnitude, while α and β are used to set the time delay and the pulse width, respectively.

As regard the magnitude of $e_p(t)$, typical values are in the range between 450 and 600 V, depending on the thickness of the sample under test. Into the model, instead, the magnitude of the voltage pulse source is chosen as proportional to the accumulated charge. For example, if the magnitude of $e_p(t)$ is fixed to 600 V, and if the amount of negative surface charges is half the positive ones, the magnitude of the voltage pulse source is chosen as 600 V for the positive charge and half (300 V) for the negative ones.

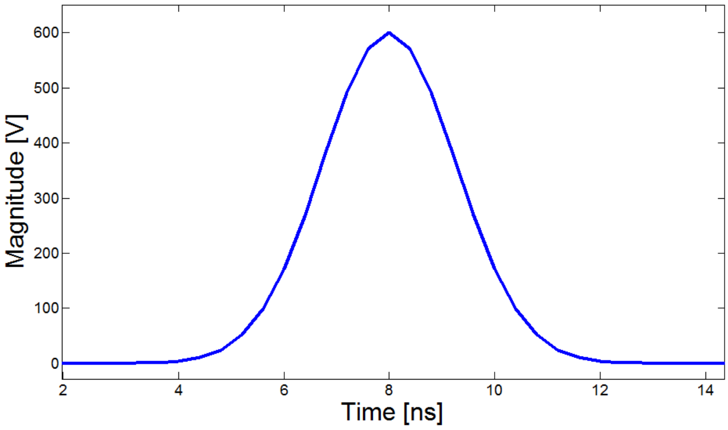

Figure 3.11. *Ideal pulse voltage waveform used into the model.*

In case in which only positive and negative surface charges are present in the sample interfaces, two pulse sources are inserted in series to the transmission line representing the sample, as shown in Figure 3.12, in which the pulse source polarity depends on the sign of the accumulated surface charge.

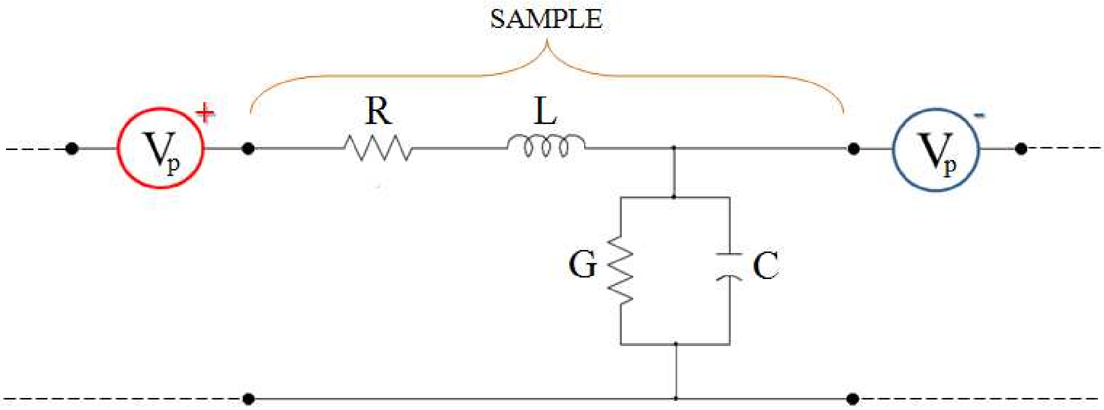

Figure 3.12. *Pulse sources inserted at the extremity of the sample transmission line. The red generator is referred to positive surface charge, while the black generator is referred to negative surface charge.*

3.10 Flow chart of the developed model

The model has been implemented in Matlab-Simulink environment. In Matlab the FDTD method has been used in order to simulate the propagation of acoustic waves in lossy transmission lines. While, in Simulink, the Leach's impedance-type transducer model has been implemented in order to simulate the piezoelectric sensor.

The flow chart of the developed model is reported in Figure 3.13. As input data, the model requires the parameters of each PEA cell component, such as length (or thickness), density ρ, speed of sound v and the attenuation coefficients α and α_{tc}. Then, the corresponding values of resistance R, inductance L, capacitance C and conductance G are calculated for each transmission line by using equations (3.1-3.4). After that, the Telegraphist's equations are solved by using the FDTD algorithm and Leapfrog technique. The simulation time is fixed by choosing an appropriate iterations number N of the FDTD for loop. When the index n of the *for loop* is lower than N, the software allows to visualize the propagation of acoustic waves as they are calculated by the software in real time. In this way the propagation, transmission and reflection phenomena within the PEA cell components and in their interfaces become easily understandable, as reported in the example of the next paragraph. When n is equal to N, the simulation ends and the final distribution of acoustic waves, described by voltage (or force) and current (or velocity), is plotted. Finally, the input and output current waves recorded in correspondence of the transducer transmission line are sent to Simulink in which are used as input data for the Leach's transducer model (which will be explained in paragraph 3.12). The output of the transducer represents the output of the PEA cell and thus the charge distribution.

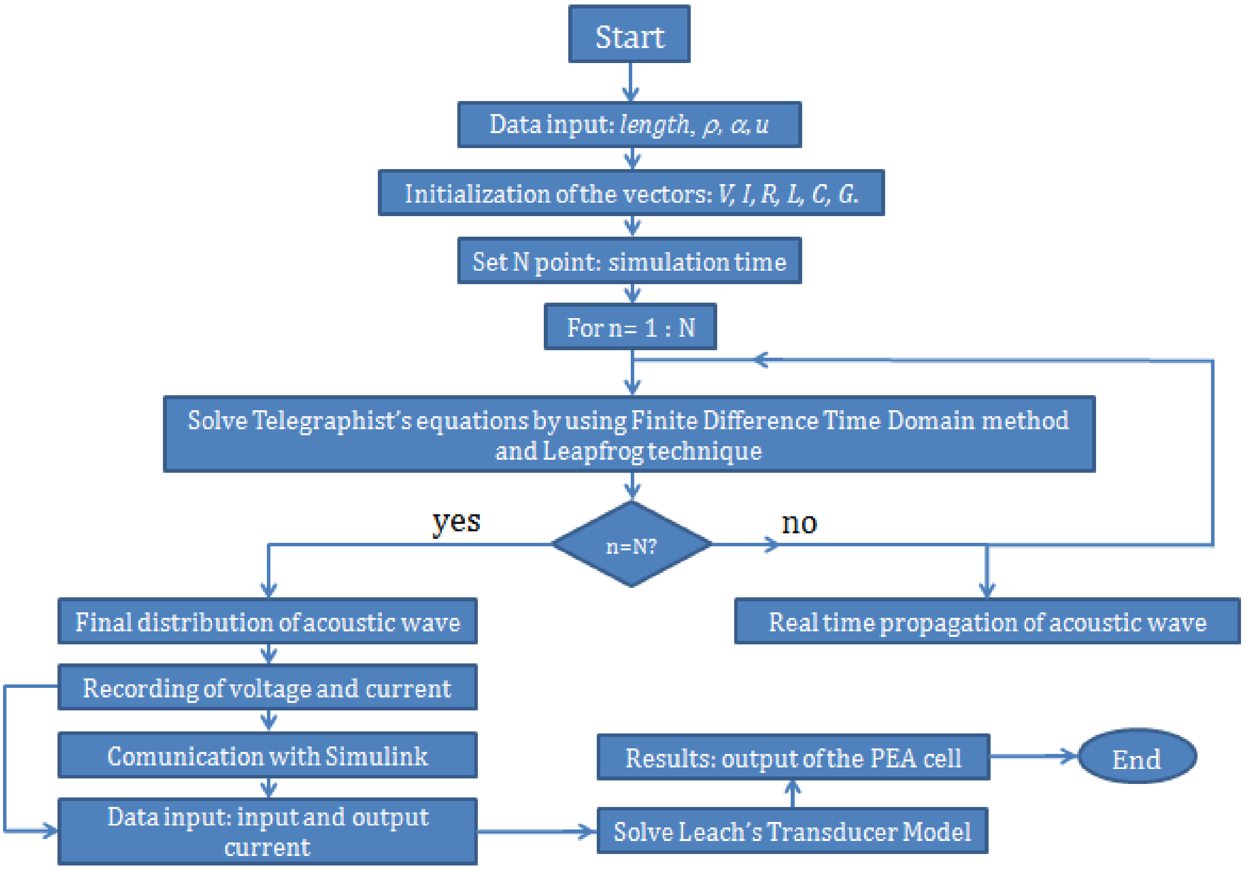

Figure 3.13. *Flow chart of the developed model.*

3.11 Dynamic simulation

As previously explained, when $n < N$ the model allows to visualize the real time propagation of acoustic waves within each PEA cell component while it is elaborated by the software.

An example of dynamic simulation is reported in the following, in which the behavior of acoustic waves within a PEA cell has been simulated. In order to better visualize the waves behavior, the pulse sources magnitude have been chosen respectively equal to + 1 V and – 1 V, while the relevant materials properties of the PEA cell components are reported in Table 3.2.

Table 3.2. *Materials properties of a PEA cell.*

Component	Material	ρ [kg/m³]	v [m/s]	Z [kg·m⁻²·s⁻¹]
HV Electrode	Aluminum	2690	6420	$17.3 \cdot 10^6$
Semiconductor	~ LDPE	930	1950	$1.8 \cdot 10^6$
Sample	LDPE	930	1950	$1.8 \cdot 10^6$
Ground Electrode	Aluminum	2690	6420	$17.3 \cdot 10^6$
Transducer	PVDF	1780	2260	$4 \cdot 10^6$
Absorber	PVDF	1780	2260	$4 \cdot 10^6$
Bottom Electrode	Aluminum	2690	6420	$17.3 \cdot 10^6$

In the table above, the acoustic impedance Z of each component, calculated as $Z = \rho \cdot v$, is also reported. In this way, the generation K^G, transmission K^T and reflection K^R coefficients previously described in equations (2.17 – 2.19), can be calculated for each interface between the PEA cell components, as shown in Table 3.3.

In the proposed example, the magnitude of the pulse sources inserted in correspondence of the semiconductor/sample and sample/ground-electrode interfaces have been chosen equal to V_{pulse_1} = 1 V and V_{pulse_2} = -1 V, respectively. Despite the same magnitude value, due to the different generation coefficients, the generated acoustic waves result different. In fact, as shown in Table 3.3, K^G_{Sem-Sa} = 0.5 and K^G_{Sa-Gr} = 0.9 for the waves propagating in the transducer direction, while, for the waves propagating in the opposite direction K^G_{Sa-Sem} = 0.5 and K^G_{GR-Sa} = 0.1. The waves generated in both directions, with magnitude given by the product $K^G_{i-j} \cdot V_{pulse}$, calculated at the start of the dynamic simulation, are shown in Figure 3.14. In this case, the waves propagate in the transducer and opposite directions and are generated by V_{pulse_1}. These are highlighted in red and orange colors, respectively. For the waves generated by V_{pulse_2}, the blue (for the transducer direction) and violet (for the opposite direction) colors are used (see also Table 3.3).

Table 3.3. *Generation, transmission and reflection coefficients for the PEA cell simulated in the example.*

Component	K^G_{i-j}	K^T_{i-j}	K^R_{i-j}
HV Electrode (HV)		1.8 ↑	-0.8 ↑ -1 ↓
Semiconductor (SEM)	0.5 ↑	↓ 0.19 1 ↑	0 ↑ 0.8 ↓
Sample (Sa)	● ↓ 0.5 0.1 ↑	↓ 1 0.19 ↑	0.8 ↑ 0 ↓
Ground Electrode (GR)	● ↓ 0.9	↓ 1.8 1.62 ↑	-0.62 ↑ -0.8 ↓
Sensor (SE)		↓ 0.37 1 ↑	0 ↑ 0.62 ↓
Absorber (ABS)		↓ 1 0.37 ↑	0.62 ↑ 0 ↓
Bottom Electrode (BO)		↓ 1.62	-1 ↑ -0.62 ↓

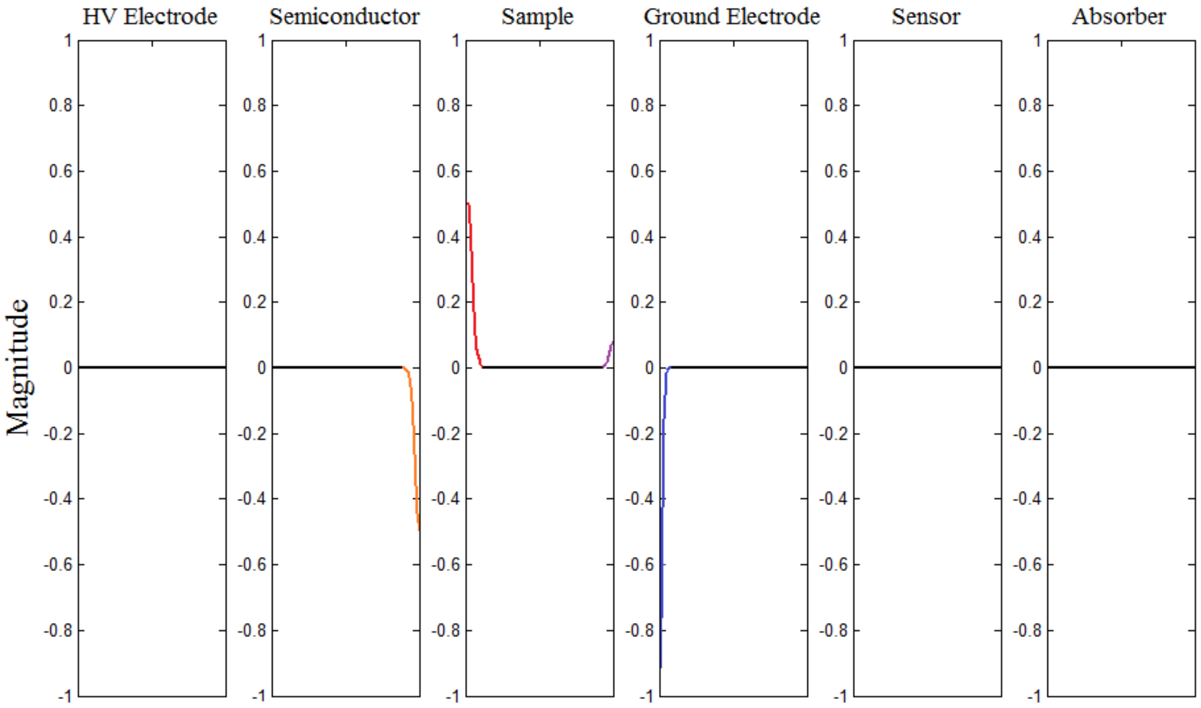

Figure 3.14. *Dynamic simulation. Waves generated at the initial time.*

Subsequently, the waves begin to travel in both directions, as depicted in Figure 3.15.

When the waves travel through the PEA cell components, they are attenuated in dependence of the material attenuation coefficient. Therefore, after a few microseconds, the situation is that of Figure 3.16. As it can be seen in the figure, because the attenuation coefficient of the dielectric material is much higher than that of aluminum, the attenuation of the waves propagating within the sample and semiconductor layer is greater as compared to that within the ground electrode.

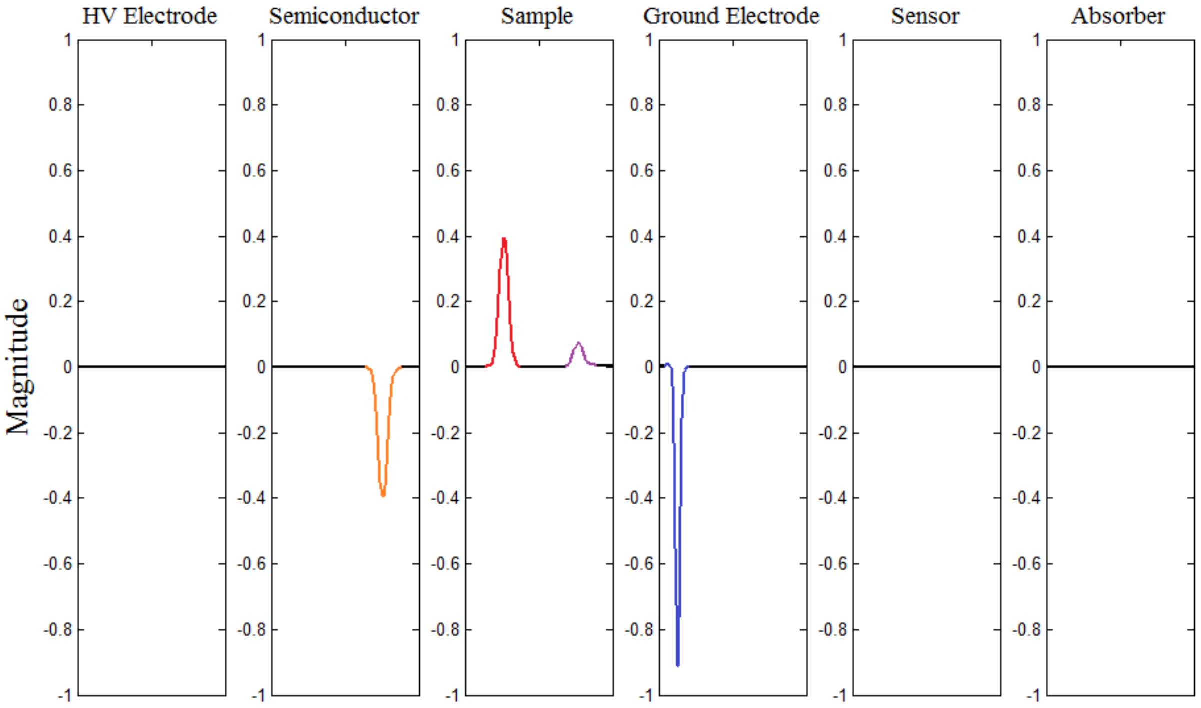

Figure 3.15. *Dynamic simulation. Propagation waves after the initial time.*

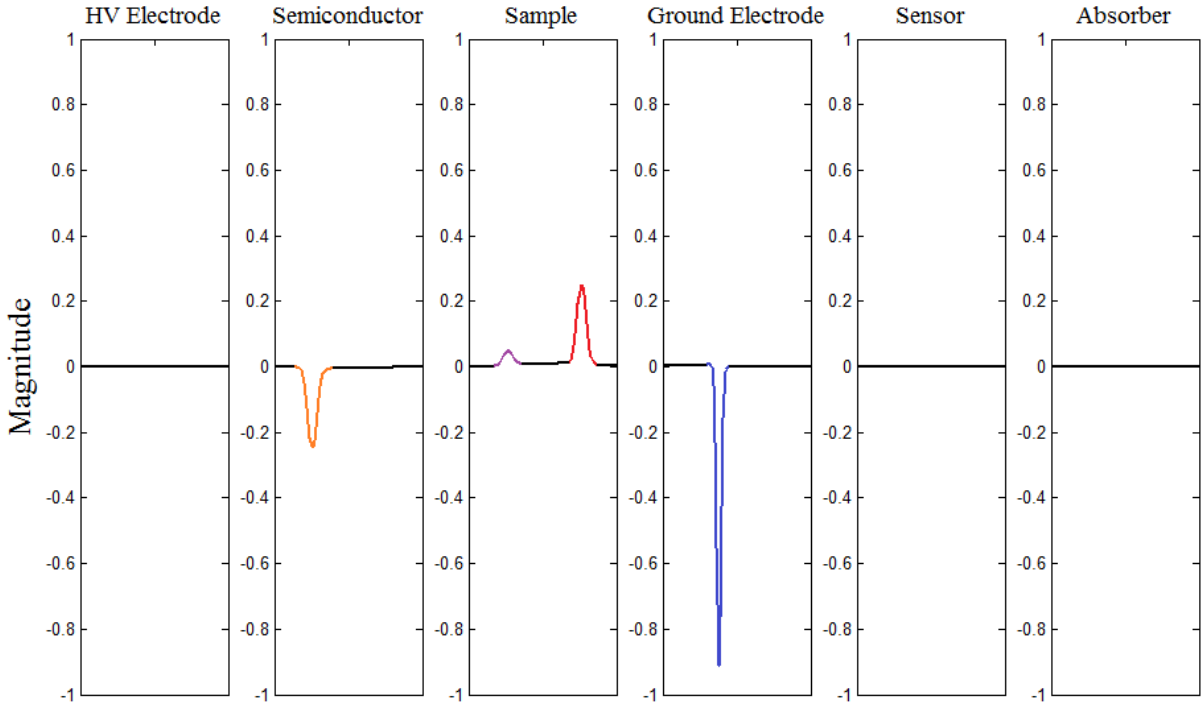

Figure 3.16. *Dynamic simulation. Waves attenuation during propagation.*

When the red wave, that travels in the transducer direction, reaches the sample/ground-electrode interface, a fraction of it is transmitted and another fraction is reflected in the opposite direction, in dependence of K_{i-j}^{T} and K_{i-j}^{G} that in this interface are equal to K_{Sa-GR}^{T} = 1.8 and K_{Sa-GR}^{R} = 0.8, as reported in Table 3.3. The same thing happens for the orange wave that travels through the semiconductor/HV-electrode interface, because the transmission and reflection coefficients are the same as the previous ones. This means that, in these interfaces, the transmitted and reflected waves are 1.8 and 0.8 times the incident waves, respectively.

These results may appear strange, as the conservation of energy principle appears violated. [130]

However, both wave magnitude and wave velocity determine the time rate of flow of energy (i. e., power) at the interface and, in terms of power, there should be a net balance. As regard the violet wave, instead, it is totally transmitted because K_{Sa-Sem}^{T} = 1, while K_{Sa-Sem}^{R} = 0. In Figure 3.17 the dynamic simulation has been stopped in correspondence of the time in which the red, violet and orange waves reach the different interfaces.

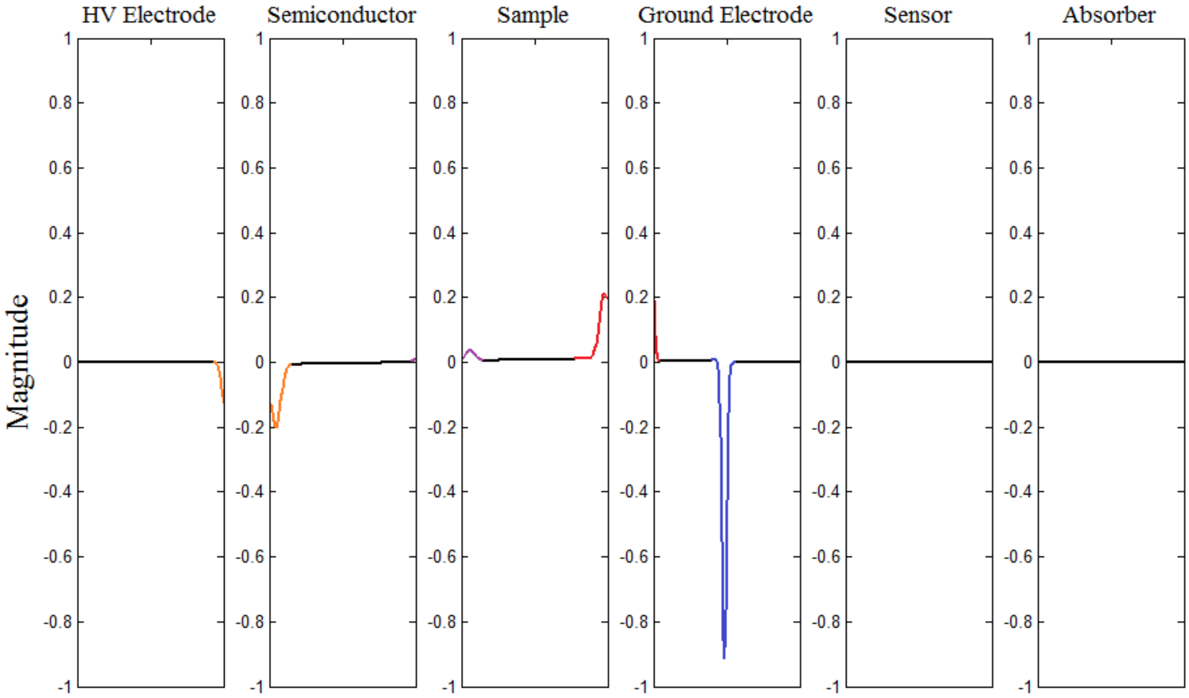

Figure 3.17. *Dynamic simulation. Instant of time in which the red, violet and orange waves reach the different interfaces.*

For subsequent time intervals, in which the red and orange waves are divided in transmitted and reflected fractions, while the violet wave is totally transmitted, the situation is reported in Figure 3.18.

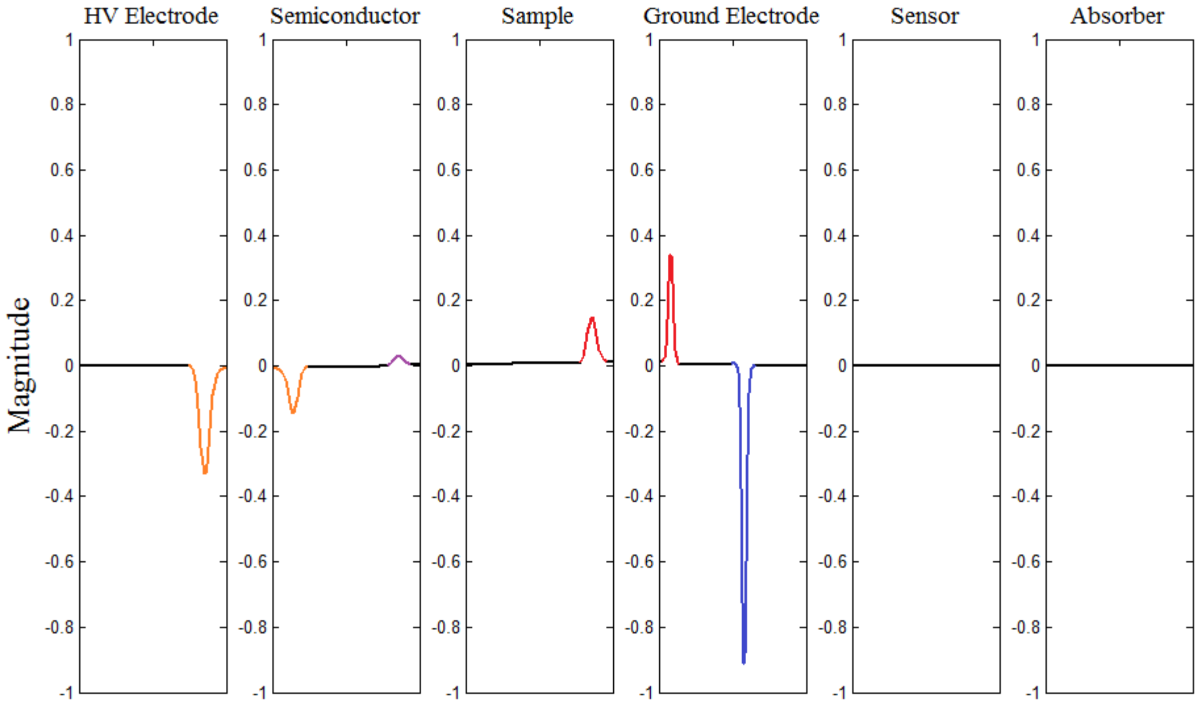

Figure 3.18. *Dynamic simulation. The red and orange waves, after reaching the interfaces, are partially transmitted and partially reflected in the opposite direction. While, the violet wave is totally transmitted. The blue wave is still propagating within the ground electrode.*

In the ground-electrode/sensor interface K^{T}_{GR-SE} = 0.37 and K^{R}_{GR-SE} = -0.62, here the negative sign indicates that the reflected wave is at 180° with the incident wave. In Figure 3.19, the time in which the blue wave reaches the transducer and starts to cross it is reported (see also the transducer oscillation in the figure). After the transducer vibration, the blue wave is reflected and goes back (with K^{R}_{GR-SE} = -0.62), while the transmitted fraction (with K^{T}_{GR-SE} = 0.37) crosses the transducer and propagates along the absorber, as shown in Figure 3.20. At the same time, the orange wave is totally reflected in the end of the PEA cell, due to the fact that, at this point, the open circuit boundary condition has been considered and thus K^{R}_{GR-SE} = -1.

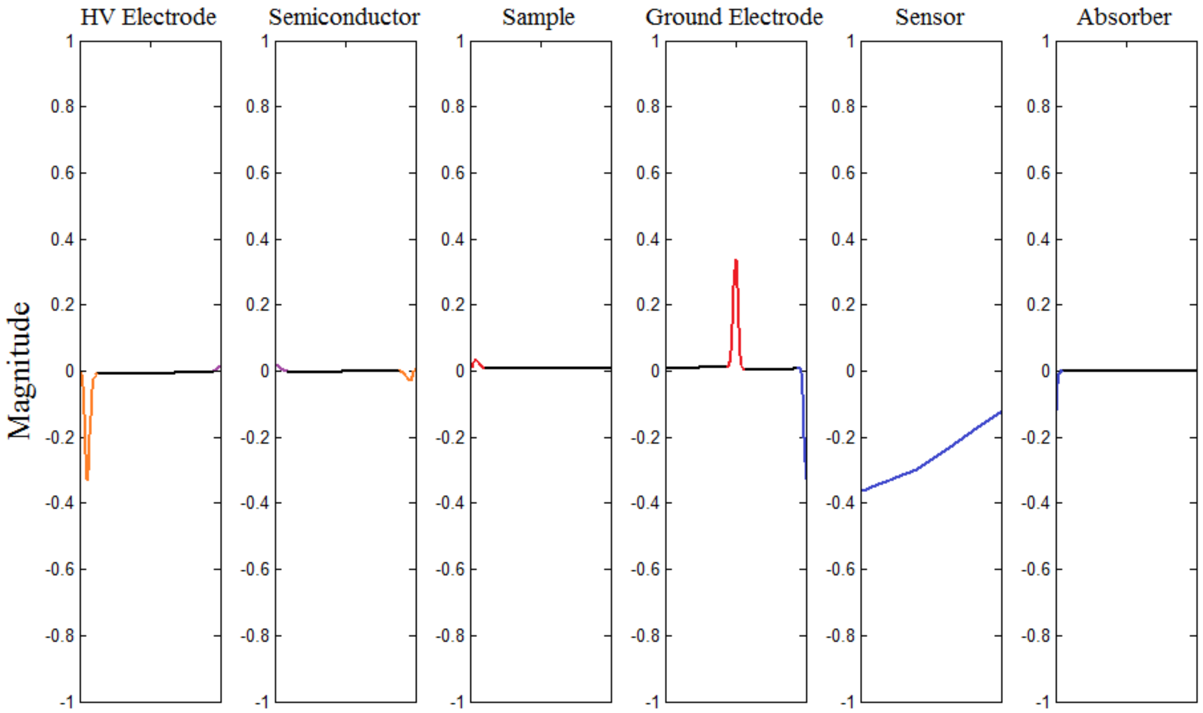

Figure 3.19. *Dynamic simulation. Instant of time in which the blue wave reaches the transducer surface, while the orange wave reaches the end part of the PEA cell.*

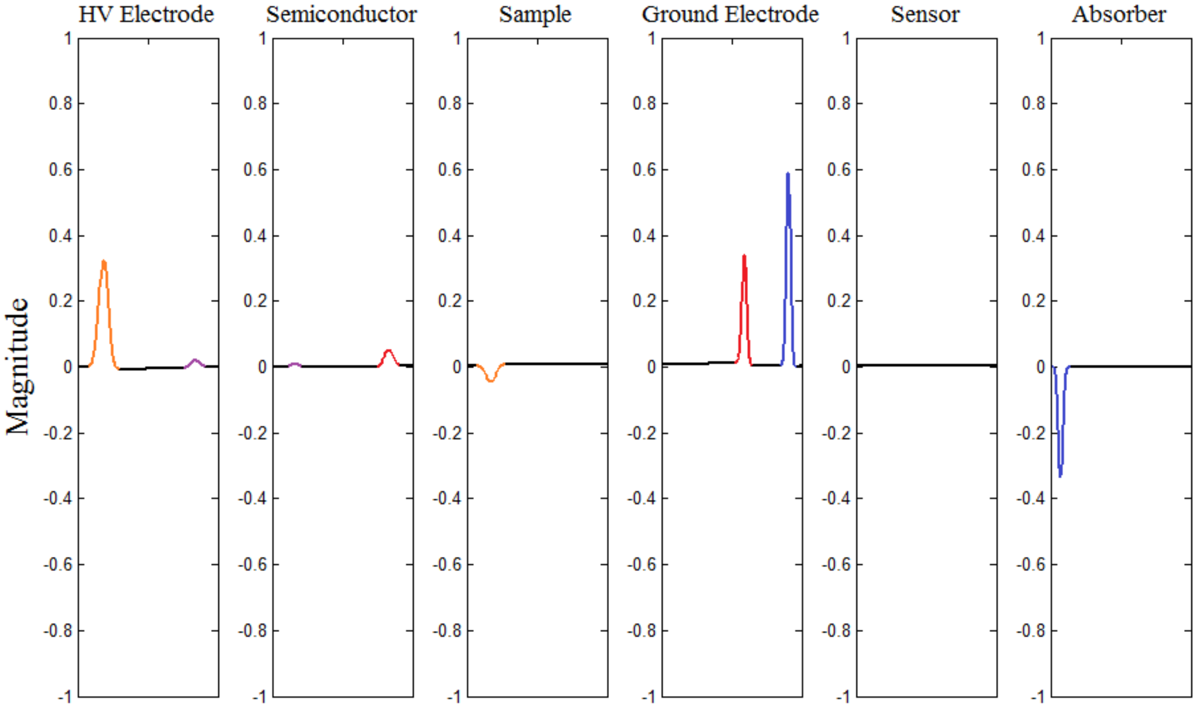

Figure 3.20. *Dynamic simulation. The blue wave, after reaching the transducer, is partially reflected in the opposite direction and partially transmitted in the absorber. The orange wave, instead, is totally reflected in the end part of the PEA cell.*

After that, also the red wave reaches the transducer surface and it is transmitted and reflected as the blue wave previously described. The time at which the transducer oscillates, due to the incident red wave, is shown in Figure 3.21.

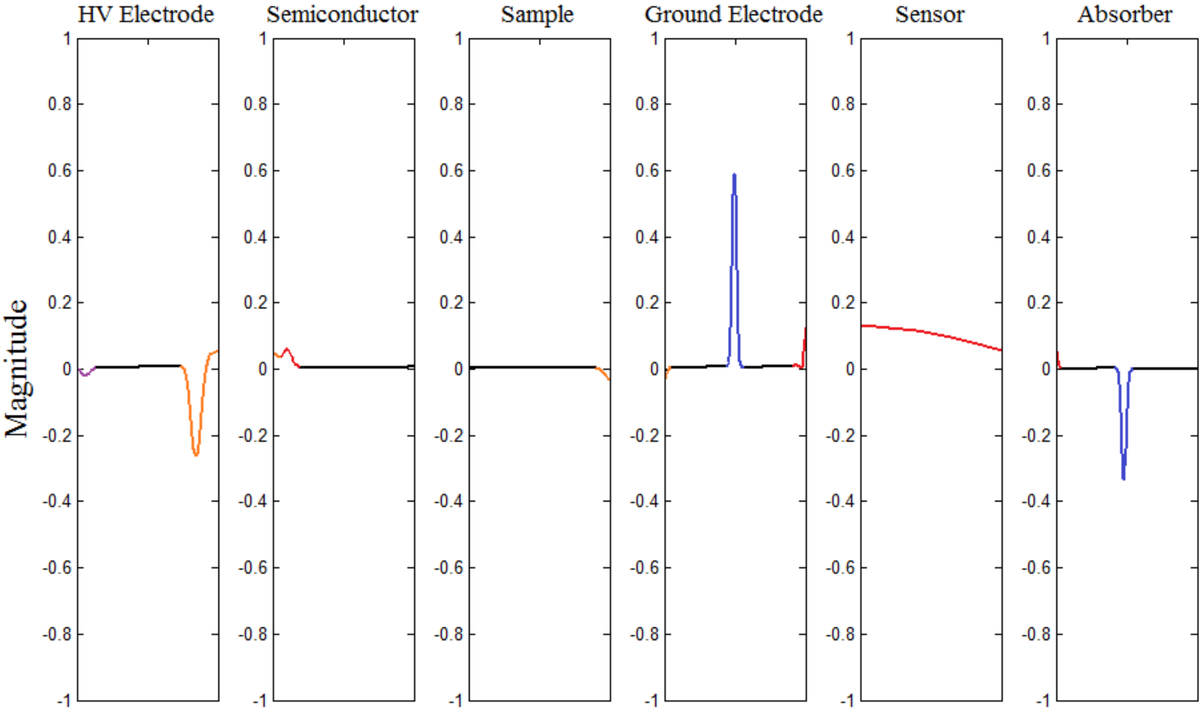

Figure 3.12. *Dynamic simulation. Instant of time in which the red wave reaches and passes through the transducer.*

After a certain time, both red and blue waves (representing the positive and negative accumulated surface charges in the sample interfaces) propagate within the absorber, as shown in Figure 3.22.

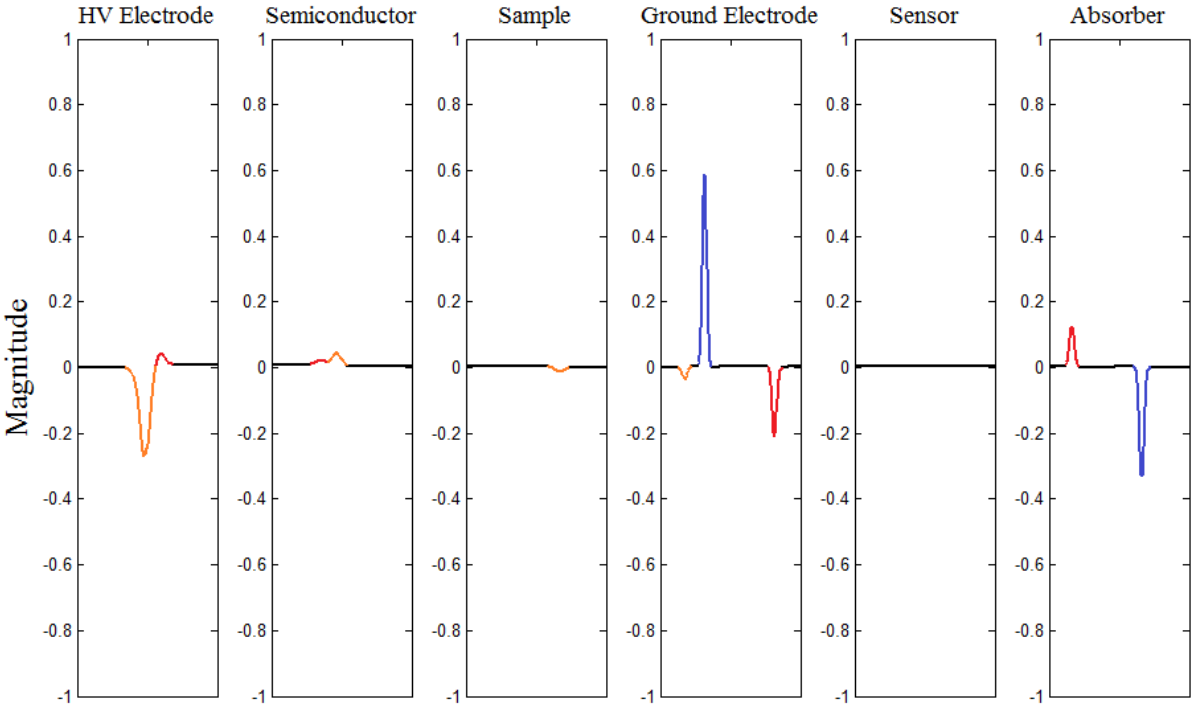

Figure 3.22. *Dynamic simulation. Both blue and red waves after being detected by the transducer are propagating within the absorber.*

The signal that passes through the transmission line representing the sensor is sent to Simulink software in which the transducer model (described in the next paragraph) is implemented.

The example above is referred to the case in which all of the PEA cell components are properly sized, and thus no reflections are present in final output signal. As explained in the previous Chapter 2, if the ground electrode or the absorber had been incorrectly sized, the blue wave would have reached the transducer surfaces several times before the red wave, and thus there would be reflections in the output signal. Simulation tests for different cases are reported in the next chapters.

3.12 The transducer model

The piezoelectric transducer, which is used to convert an incident pressure wave in an electrical signal, is modeled in Simulink environment according to the Leach's model [131-132], as shown in Figure 3.23. The transducer is constituted by two parts: the mechanical and the electrical part. The first one is used to measure the deformation of the transducer due to incident acoustic waves, while the second is used to convert the deformation into an electrical signal. The link between mechanical and electrical parts is established using current controlled current generators F_1 and F_2.

Concerning the mechanical section, the deformation is given by the difference between the propagation velocities of each surface normal to the propagation path. Because of the velocity-current analogy, it is possible to evaluate this deformation as the difference between input and output currents of the transmission line representing the transducer simulated in Matlab. The resulting current $I_{input} - I_{output}$ (read by the ammeter A_1), multiplied by the product of the piezoelectric transmitting constant h and the static capacitance of the transducer C_0, controls the current generator F_1. Finally, across the capacitance C_0, connected in parallel to the source F_1, a potential difference proportional to the transducer deformation is obtained.

As regards the electrical part, the current read by the ammeter A_2 and multiplied by the constant h is used to control the other current generator F_2. In order to obtain the total charge, that proportionally modifies the shape of the transducer, the output of F_2 is connected to the capacitor C_1 (with value equal to 1 F) to be integrated. The controlled voltage generator E_1 with unitary gain is a one-way insulation for the integrator. The resistances R with value 10 MΩ are inserted just to avoid a floating voltage of nodes. While, C_0 and h for the 9μm PVDF transducer, are equal to 226 pF and $0.03 \cdot 10^{12}$, respectively.

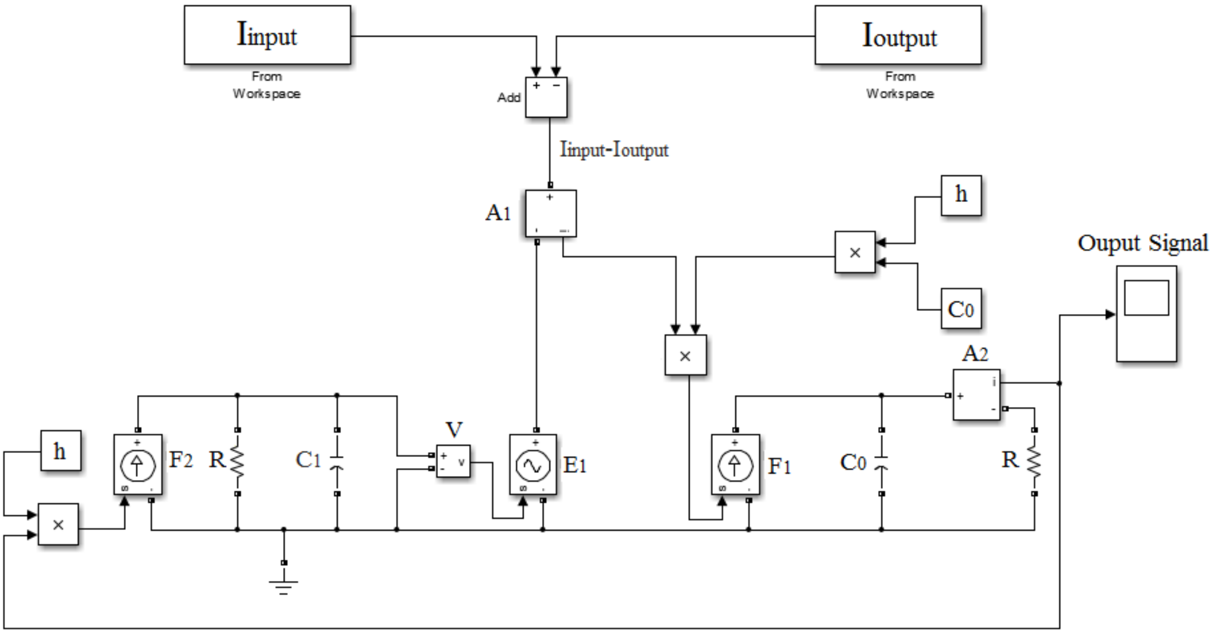

Figure 3.23. *Implemented Leach's impedance-type transducer model.*

Chapter 4

Simulation of the PEA cell

In this chapter, the validation of the developed PEA cell model is reported.

Initially, simulations demonstrating what already explained in the previous Chapter 2, with respect to the correct sizing of the PEA cell components, are carried out. Therefore, the influence of the ground electrode and absorber thicknesses, which may cause reflections within the main PEA cell output signal, is evaluated. In this case, a first validation of the model has been obtained, because the simulations results provide the same patterns as those found in literature.

In the second part of this chapter, a further model validation has been made by comparing simulation and experimental results. The latter have been obtained by using both the PEA cell of the TDHVL laboratory and the PEA cell of the LEPRE laboratory. Also in this case, the good performance of the developed model are confirmed, due to very similar PEA cell output signals (by both experimental and simulation tests) obtained.

4.1 Features of the simulated PEA cell

In order to evaluate the correct functioning of the developed model, the first simulations have been made similar to those proposed in the work [124], in which a LDPE layer with thickness 200 μm has been used as a sample.

The simulated acoustic circuit of the PEA cell has the same structure as that reported in Figure 3.1. Besides, its electrical equivalent circuit, which is realized by connecting in series the transmission lines of each PEA cell component, is shown in Figure 4.1. Considering the presence of only surface charges, in the electrical equivalent circuit, two pulses sources are inserted in the extremities of the transmission line that models the sample under test. Furthermore, two resistances R_0 with high value (~1 MΩ) are inserted at the beginning and at the end of the entire equivalent circuit as terminating resistance for the transmission line.

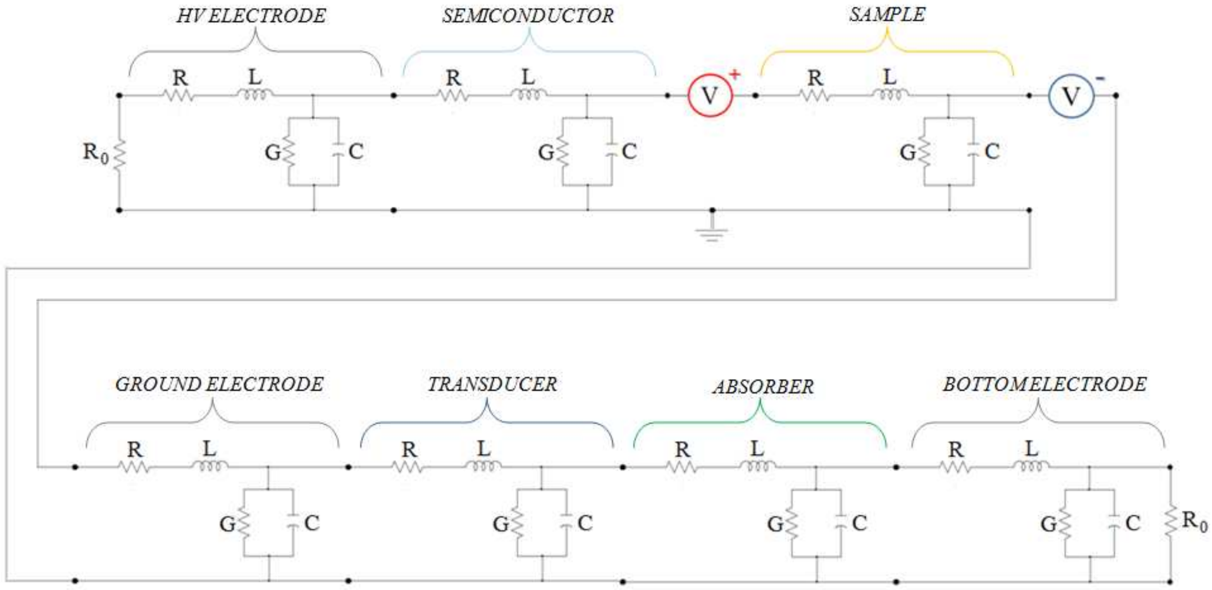

Figure 4.1. *Equivalent electric circuit of the PEA cell.*

The physical properties of the materials employed in PEA cell components of Figure 4.1, such as aluminum, PVDF and LDPE are reported in Table 4.1.

Table 4.1. *Physical properties of the materials employed in the PEA cell*

Material	ρ [kg/m³]	v [m/s]	α [Np/m]
Aluminum	2690	6420	10
PVDF	1780	2260	15.42
LDPE	930	1950	4873

Knowing the physical properties listed in Table 4.1, the electrical quantities of each transmission line can be calculated by using equations (3.1 - 3.4). In these equations, the area A of cross section is also required. Considering that, in most cases, the diameter of the HV electrode is 10 mm, the parameter A results 78.5 mm². The calculated electrical quantities, neglecting the conductance G, are shown in Table 4.2, in which the thickness of each component is also reported.

Table 4.2. *Transmission lines parameters*

Component	Material	R [kΩ/m]	L[mH/m]	C [μF]	Thickness [m]
HV Electrode	Aluminum	27.11	211.16	0.15	$5\cdot10^{-3}$
Semiconductor	LDPE[1]	1387.43	73	3.6	$2\cdot10^{-4}$
Sample	LDPE	1387.43	73	3.6	$2\cdot10^{-4}$
Ground Electrode	Aluminum	27.11	211.16	0.15	$23\cdot10^{-3}$
Sensor	PVDF	9.73	139	1.4	$10\cdot10^{-6}$
Absorber	PVDF	9.73	139	1.4	$250\cdot10^{-6}$
Bottom Electrode	Aluminum	27.11	211.16	0.15	$5\cdot10^{-3}$

---

[1] In the referred article [124] LDPE was used as semiconductor layer.

4.2 Simulations results

The first simulation is performed considering a constant DC stress equal to 10 kV, which corresponds to an electric field equal to 50 kV/mm across the 200 μm thick sample. Because the dielectric permittivity of LDPE is ε_r = 2.3, the accumulated surface charge in both sample interfaces, calculated by using equations (2.2) and (2.3), results almost 1 mC/m² and -1 mC/m². Furthermore, because of the same absolute value of the surface charges, the magnitudes of the positive and negative pulse sources of Figure 4.1, which are proportional to the accumulated charge, are chosen +600 V and -600 V.

In addition, in the y-axis of the following patterns, the voltage quantity in [mV] is present instead of charge quantity in [C/m³]. This because the signal obtained in the simulations represents the output signal of the transducer, without being processed on the computer. In order to convert the voltage signal in the corresponding charge, a calibration procedure is needed, as previously described in Chapter 2. However, because the time scale (which is the more significant quantity in the simulations for this thesis) remains unchanged before and after the calibration, which means that the position of the main output signal and the position of the reflections are not affected, this technique will not be applied in the simulated output signal.

Based on the above assumptions, and by using the component dimensions listed in Table 4.2, simulation result is shown in Figure 4.2.

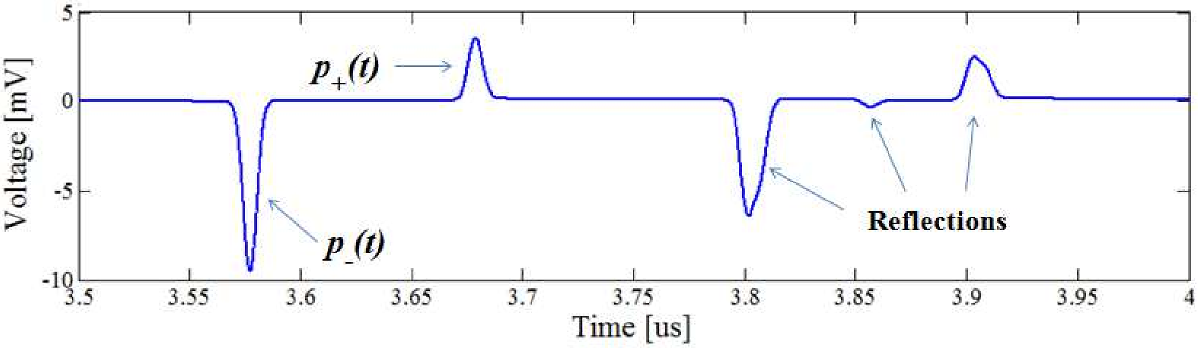

Figure 4.2. *Output of the transducer in the properly dimensioned PEA cell*

As it can be noted in the figure above, due to correct dimensions of the PEA cell components, the original signal constituted by $p_+(t)$ and $p_-(t)$, due to positive and negative surface charge, respectively, is not affected by reflections. The latter occur within the absorber, and after a certain time (the first one around 3.8 μs) are detected by the transducer.

4.2.1 Importance of ground electrode thickness

As explained in paragraph 2.4, if the thickness of the ground electrode is not properly sized, reflections may occur in the main output signal of the PEA cell. In particular, it has been found that equation (2.38) must be satisfied in order to avoid that the reflected wave within the ground electrode $p_-^{R_G}(t)$ anticipates the main peak $p_+(t)$ referred to the positive surface charge.
For example, for a LDPE sample with thickness d_{Sa} and speed of sound v_{LDPE}, equation (2.38) can be rewritten as follows:

$$d_{GR} > \frac{1}{2} d_{Sa} \frac{v_{AL}}{v_{LDPE}} \tag{4.1}$$

Considering the values of Table 4.1, and d_{Sa} = 200 μm, d_{GR} should be greater than 330 μm. By reference to Figure 2.3, if d_{GR} is chosen 325 μm, $p_-(t)$ reaches the transducer after 0.05 μs and $p_+(t)$ after $\tau_{Sa} + \tau_{GR}$ = 0.153 μs, while $p_-^{R_G}(t)$ after $3\tau_{GR}$ = 0.150 μs. Therefore, reflections are present and thus more than two peaks will appear in the original signal, as shown in Figure 4.3.

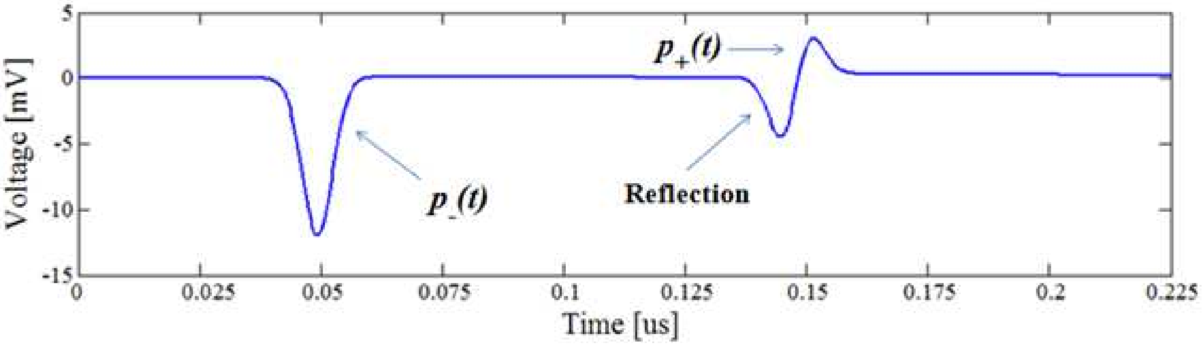

Figure 4.3. *Output of the PEA cell. A reflection is present in the original signal due to the incorrect thickness of the ground electrode.*

Whereas, if d_{GR} is equal to 335 μm, $\tau_{Sa} + \tau_{GR}$ becomes 0.154 μs, while $3\tau_{GR}$ results 0.156 μs. In this case, the relationship (4.1) is satisfied and no reflections occur in the original signal, as in the case of Figure 4.2, in which the ground electrode is properly sized.

4.2.2 Importance of absorber thickness

Considering the result of the previous example, for a 200 μm thick LDPE sample the correct thickness of the ground electrode has been calculated greater than 330 μm. By using the ground electrode thickness equal to 23 mm (which is the typical value adopted in real PEA cell), $p_{+}(t)$ and $p_{-}(t)$ reach the transducer after 3.68 μs and 3.58 μs, respectively. With respect to Figure 2.4, and according to equation (2.41) in which v_A is replaced by v_{LDPE}, to avoid that the reflection $p_{-}^{R_{ABS}}(t)$ reaches the transducer before than $p_{+}(t)$, the thickness of the absorber d_{ABS} must be greater than 116 μm. In fact, if equation (2.41) is not fulfilled because d_{ABS} is chosen equal to 100 μm, $p_{-}^{R_{ABS}}(t)$ reaches the transducer after 3.67 μs and thus false signals occur in the main output signal, as shown in Figure 4.4.

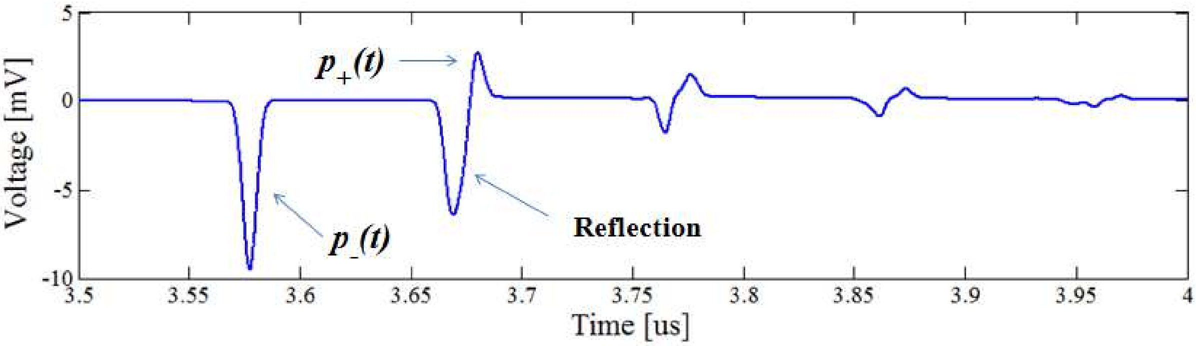

Figure 4.4. *Output of the PEA cell. A reflection is present in the original signal due to the incorrect thickness of the absorber.*

In order to better evaluate the effect of the absorber thickness in the output of the PEA cell, another simulation is carried out. For a 50 μm thick absorber, the reflected wave $p_{-}^{R_{ABS}}(t)$ reaches the transducer after 3.62 μs. Subsequently $p_{-}^{R_{ABS}}(t)$ is reflected again within the absorber and after τ_{GR} + 4τ_{ABS} = 3.67 μs the signal reaches the transducer for the second time, and before the main peak $p_{+}(t)$. Therefore, two reflections are present in the main signal, as shown in Figure 4.5.

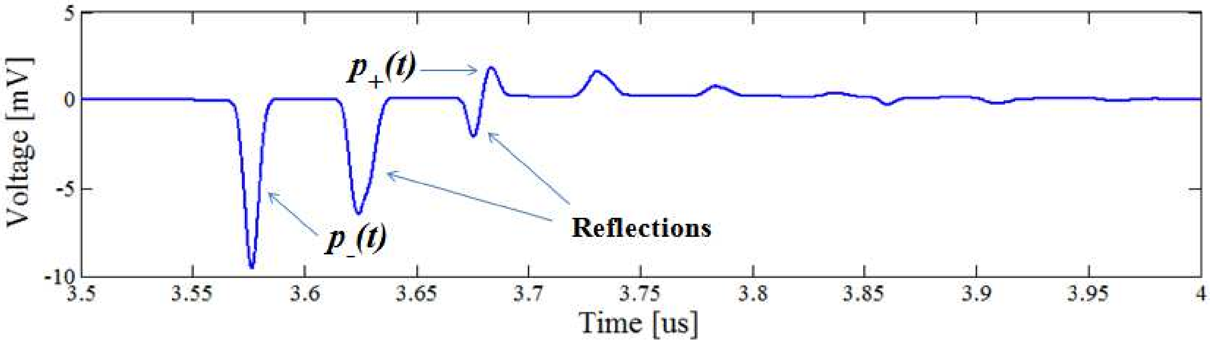

Figure 4.5. *Output of the PEA cell. Two reflections are present in the original signal due to the smaller thickness of the absorber.*

4.2.3 Importance of transducer thickness

The piezoelectric sensor employed in the PEA cell and the mathematical formulas which describe its principle of operation have been already reported and are discussed in Chapter 2. As it can be noted in equation (2.44), the magnitude of the transducer voltage output signal is proportional to its static capacitance, to the incident pressure on its surface and to its thickness. The effect of the transducer thickness d_{SE} on the PEA output signal has been evaluated by performing a simulation in which all dimensions of the PEA cell components are the same as those reported in Table 4.2, unlike the value of d_{SE}.

By choosing d_{SE} = 5 µm, the simulation result is shown in Figure 4.6. The comparison between this result and that of Figure 4.2, in which d_{SE} = 10 µm was used, shows that for a double d_{SE} value, the PEA output signal magnitude is also doubled and vice versa. In fact, for d_{SE} = 10 µm the maximum magnitude values of the negative and positive peaks were almost -10 mV and 4 mV, respectively. While, for d_{SE} = 5 µm the maximum magnitude values of the negative and positive peaks are around -5 mV and 2 mV, respectively.

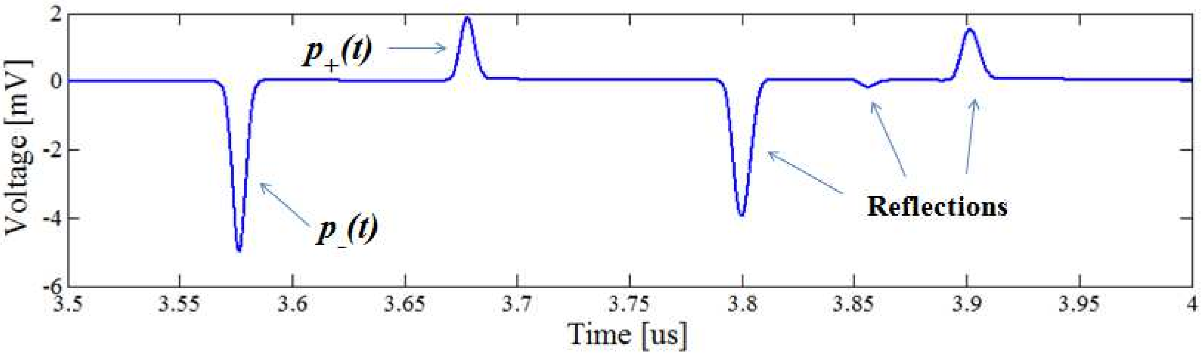

Figure 4.6. *Output of the PEA cell for 5µm transducer thickness.*

4.3 Experimental validation of the developed model by the PEA cell of the TDHVL laboratory

In order to validate the model, a comparison between experimental tests and simulation results have been carried out in different dielectric specimens with physical properties listed in Table 4.3. As it can be noted, the speed of sound of the LDPE is different from the previous value reported in Table 4.1. This because of a different sample realization process.

Experimental tests have been made by using the PEA cell of the TDHVL, with components dimensions and transmission line parameters reported in table 4.4. In the same table, the thicknesses and the calculated transmission line parameters for the three tested samples, are also reported.

As regard the DC stress, 2 kV has been chosen for the LDPE samples with thicknesses 100 μm and 180 μm. While, 4 kV has been used for the 280 μm thick XLPE sample. These low DC voltage supply values have been chosen in order avoid space charge formation in the insulation bulk, with the aim to observe only the peaks due to surface charges.

The accumulated surface charges in the three samples are equal in magnitude and opposite in sign (equations (2.2) and (2.3)). Therefore, as in the case of the previous simulation tests, the inserted pulse sources (see Figure 4.1) are chosen proportional to the accumulated surface charges and equal to +600 V and – 600 V.

Table 4.3. *Physical properties of the LDPE and XLPE materials.*

Material	ρ [kg/m^3]	v [m/s]	α [Np/m]
LDPE	930	2200	4873
XLPE	900	2200	2140

Table 4.4. *Transmission line parameters calculated for the experimental PEA cell components and samples under test.*

Component	Material	R [kΩ/m]	L[mH/m]	C [μF]	Thickness [m]
HV Electrode	Aluminum	27.11	211.16	0.15	$5\cdot10^{-3}$
Semiconductor	Semiconductor	1936.6	86	2.18	$150\cdot10^{-6}$
Sample 1	LDPE	1556.1	73	2.8	$100\cdot10^{-6}$
Sample 2	LDPE	1556.1	73	2.8	$180\cdot10^{-6}$
Sample 3	XLPE	665.6	70	2.9	$280\cdot10^{-6}$
Ground Electrode	Aluminum	27.13	211.3	0.11	$2\cdot10^{-3}$
Sensor	PVDF	9.74	139	1.4	$9\cdot10^{-6}$
Absorber	PVDF	9.74	139	1.4	$0.45\cdot10^{-3}$
Bottom Electrode	Aluminum	27.11	211.16	0.15	$5\cdot10^{-3}$

In the following, the patterns obtained by experimental tests, show the output of the PEA cell after application of the calibration technique; therefore a charge signal is obtained. On the other hand, the patterns obtained by simulation tests, show a voltage signal. As previously explained, both signals differ for a calibration factor and therefore the comparison is possible because the time axis remains unchanged.

The time delay present in the output signal of the experimental PEA cell, which is equal to 22 ns, has been taken into account into the model.

4.3.1 Experimental and simulation results on Sample 1

For a 100 μm LDPE sample, the first peak due to negative surface charge occurs after 0.311 μs. While the second peak due to positive surface charge occurs after 0.356 μs. Considering the time delay of the measurement system, the peaks are shifted of 22 ns. Therefore, the corresponding times of the first and the second peak are 0.333 μs and 0.378 μs, respectively. Figure 4.7 shows the charge distribution obtained by experimental test, while simulation result is reported in Figure 4.8.

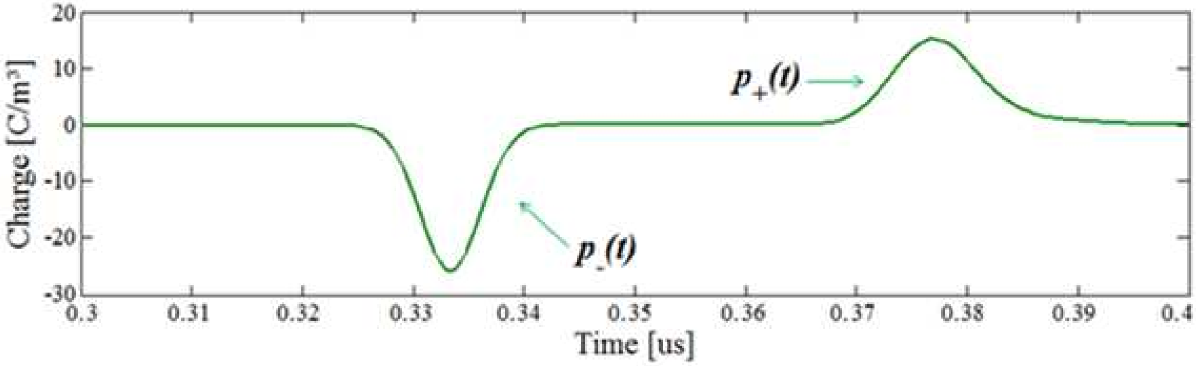

Figure 4.7. *Charge pattern obtained by experimental test, for LDPE sample with thickness 100 μm.*

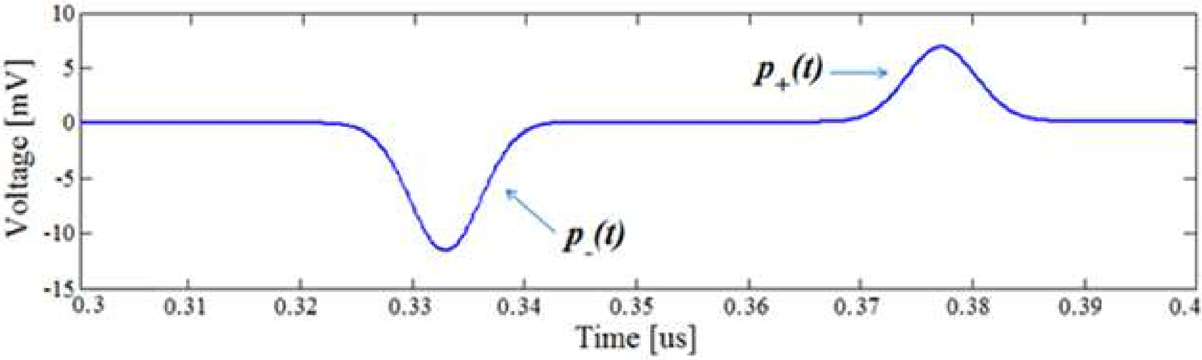

Figure 4.8. *Output of the PEA cell obtained by simulation test, for LDPE sample with thickness 100 μm.*

4.3.2 Experimental and simulation results on Sample 2

For a LDPE sample with thickness 180 μm, the negative peak occurs at the same time of the previous case. This because the corresponding time of this peak depends only on the ground electrode thickness and its speed of sound, which have remained unchanged. The positive peak, which depends on the sample features, occurs after 0.081 μs from the negative one. By taking into account the PEA cell time delay, the second peak occurs at 0.414 μs. The calculated time values are confirmed by both experimental and simulation results, as shown in Figures 4.9 and 4.10.

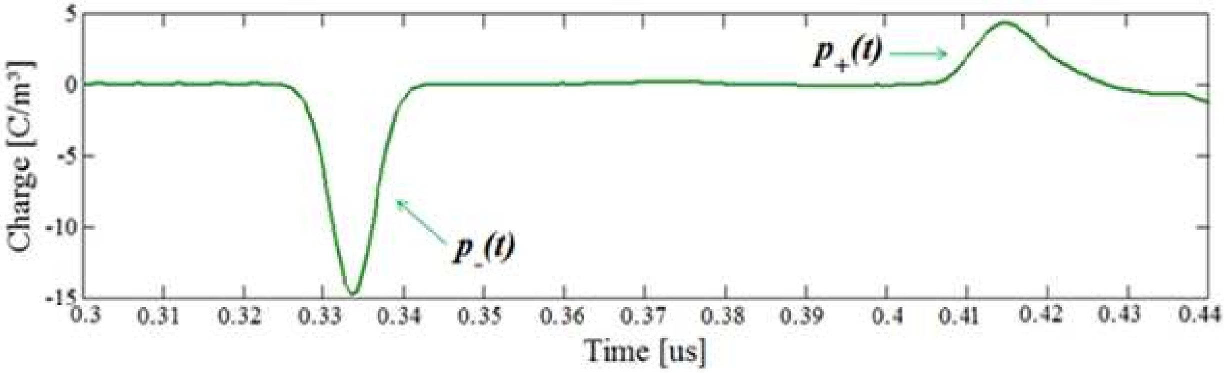

Figure 4.9. *Charge pattern obtained by experimental test, for LDPE sample with thickness 180 μm.*

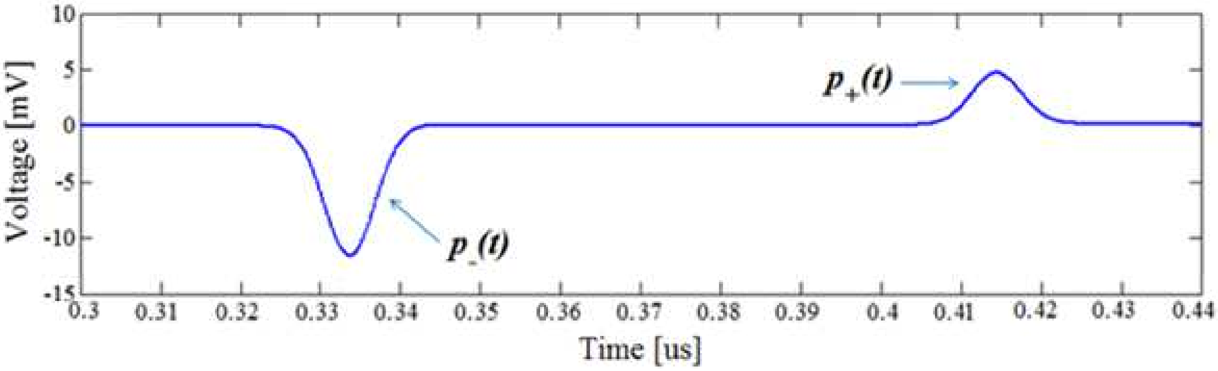

Figure 4.10. *Output of the PEA cell obtained by simulation test, for LDPE sample with thickness 180 μm.*

4.3.3 Experimental and simulation results on Sample 3

The last comparison is performed in a XLPE sample with thickness 280 μm. The speed of sound of this material is the same of the previous samples, while the thickness is higher. This implies that the second peak, due to positive surface charge, occurs at 0.460 μs (including the time delay). Experimental and simulation results are shown in Figures 4.11 and 4.12, respectively.

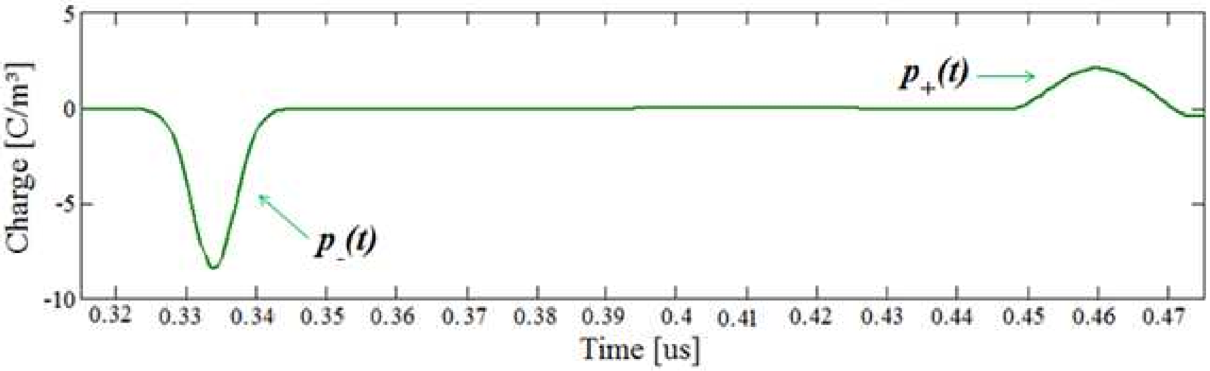

Figure 4.11. *Charge pattern obtained by experimental test, for XLPE sample with thickness 280 μm.*

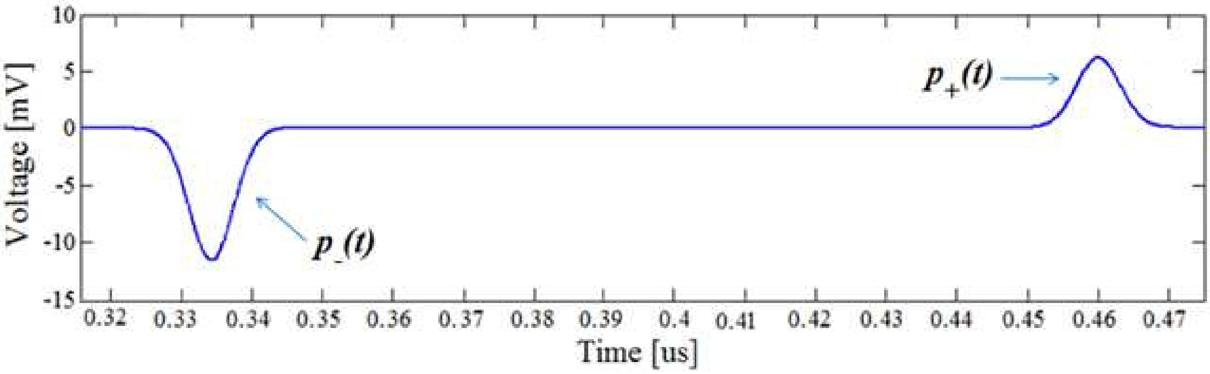

Figure 4.12. *Output of the PEA cell obtained by simulation test, for XLPE sample with thickness 280 μm.*

As it can be noticed in all the figures above, the comparison between experimental and simulation results confirm the good performances of the developed model.

4.4 Experimental validation of the developed model by the PEA cell of the LEPRE laboratory

In this paragraph, a further experimental validation of the developed model is made by means of the PEA cell of the LEPRE laboratory.

The experimental measurement setup, which is similar to that used at the TDHVL, is reported in Figure 4.13. Where, cable 1 connects the HVDC generator to the upper electrode of the PEA cell. Cable 2 provides the constant DC voltage at the chopper placed within the PEA cell. The chopper, which is externally powered by the connection 3, is used to create the pulse stress. The latter, with amplitude equal to that of the pulse generator voltage supply, is sent to upper electrode of the PEA cell by means of connection 4. The amplifier, used to increase the sensor output voltage level, is externally powered by cable 5, and its output signal is connected to the CH2 channel of the oscilloscope to be visualized. While, the CH3 channel is used as trigger. Finally, the oscilloscope is connected by GPIB (General Purpose Interface Bus) at the computer, in which the measured space charge signal is processed.

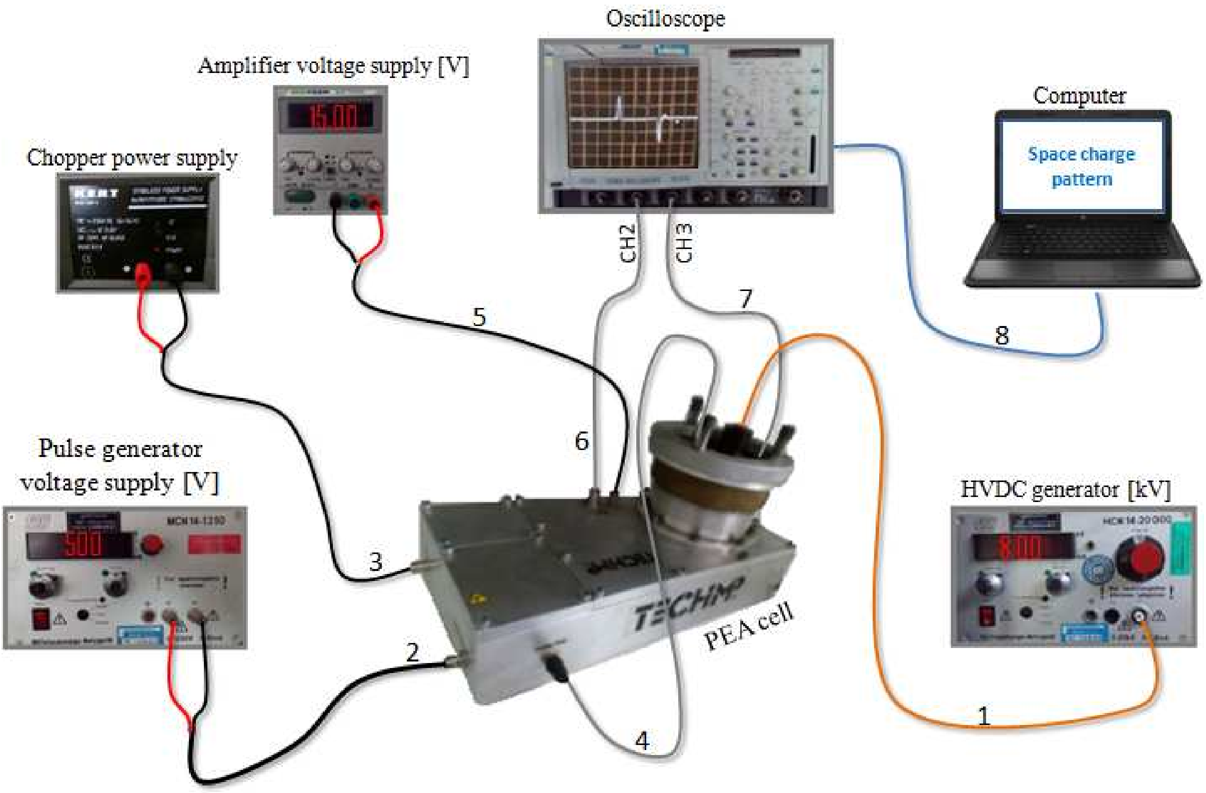

Figure 4.13. *PEA measurement setup of the LEPRE laboratory.*

In the operating manual of the PEA cell above described is reported that the instrument allows to test specimens with thickness under 0.5 mm. This is true only in the case in which materials with speed of sound equal to 2200 m/s are tested. In fact, considering that the absorber of this PEA cell is 250 µm thick (and v_{PVDF}= 2260 m/s, as in the previous cases), after simple mathematical manipulations of equation (2.41), the following value $d_{Sa} \leq 0.5$ mm is obtained. This means that, with respect to Figure 2.4, if a specimen with v_{Sa} = 2200 m/s and d_{Sa} greater than 0.5 mm is used, $p_{-}^{R_{ABS}}(t)$ reaches the sensor surface before than $p_{+}(t)$ and therefore reflections occur in the main output signal.

In order to verify what explained above, a specimen with v_{Sa} = 2200 m/s and $d_{Sa} \geq 0.5$ mm should be used. Unfortunately, a specimen with these features was not found, and thus another sample with features reported in Table 4.5 has been employed.

Table 4.5. *Features of the material tested for the verification of reflections within the absorber.*

Material code	**Thickness [m]**	**ρ [kg/m³]**	**v [m/s]**	**α [Np/m]**
RS 2134	$0.69 \cdot 10^{-3}$	900	1189	2170

By using the speed of sound of this material, the maximum value of the sample thickness d_{Sa} that can be tested without resorting to reflections in the main output signal, can be derived from equation (2.41), which is rewritten as:

$$d_{Sa} < 2d_{ABS}\frac{v_{Sa}}{v_{ABS}} \Rightarrow d_{Sa} < 0.26\text{ mm} \tag{4.2}$$

Considering that the thicknesses of the ground electrode and of the sensor of the LEPRE lab PEA cell are 1 cm and 9 μm, respectively, with reference to Figure 2.4, $p_{-}(t)$ reaches the sensor after τ_{GR} = 1.55 μs and $p_{+}(t)$ after $\tau_{\text{Sa}} + \tau_{\text{GR}}$ = 2.13 μs. While the reflected wave within the absorber $p_{-}^{R_{ABS}}(t)$ needs a time $\tau_{\text{GR}} + \tau_{\text{SE}} + 2\tau_{\text{ABS}}$ = 1.77 μs to be detected by the sensor. However, a reflection occurs in the main signal, as demonstrated in the following.

An experimental measure has been made by using the PEA cell of the LEPRE laboratory and the material described in Table 4.5 as specimen under test. The magnitudes of the HVDC and pulse generators are chosen the same as those shown in Figure 4.13, namely 8 kV and 500 V, respectively.

The output signal depicted in the oscilloscope is reported in Figure 4.14. As it can be seen, the signal is not deconvoluted and calibrated, therefore a voltage signal is present in the y-axis.

In the figure, the negative and positive peaks, due to the surface charges deposited in the ground-electrode/sample and sample/HV-electrode interfaces, are positioned at the corresponding time previously calculated, namely 1.55 and 2.13 μs, respectively. In the same way, the negative peak due to the reflection within the absorber occurs at the time 1.77 μs.

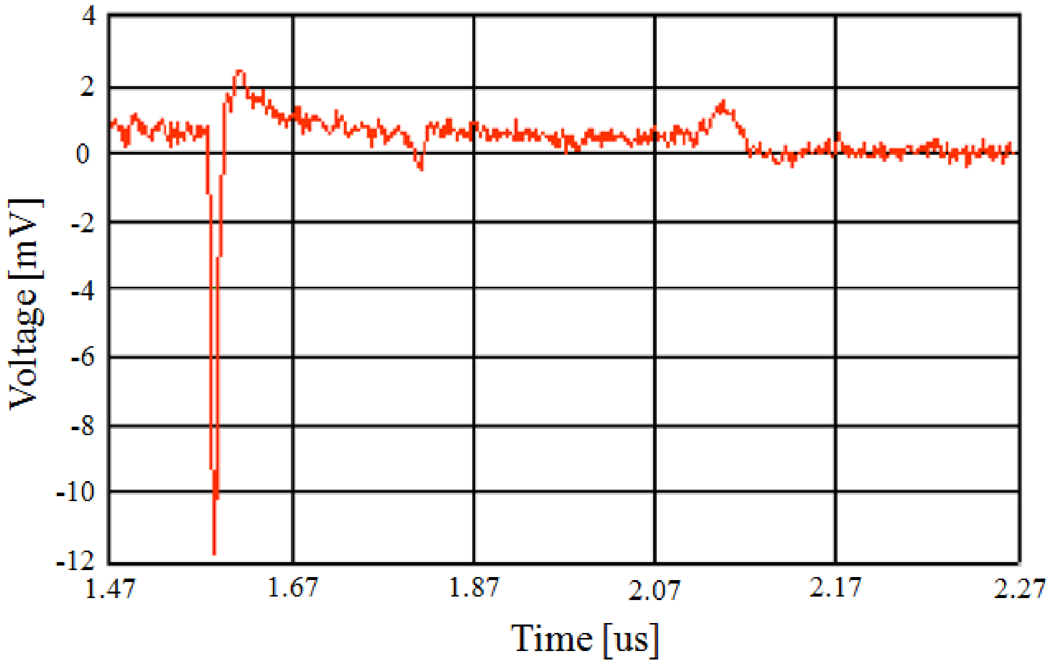

Figure 4.14. *PEA output signal displayed by the oscilloscope. A reflection occurs within the main output signal, due to absorber thickness and specimen features.*

In the light of the above, the calculations previously made, regarding the position of the peaks and the presence of a reflection, have been confirmed by experimental test.

In order to verify if the developed model provides the same result of those found experimentally, the PEA cell of the LEPRE laboratory and the sample described in Table 4.5 have been modeled. The transmission line parameters, as well as the materials and thicknesses, of both PEA cell components and sample under test, are reported in Table 4.6.

Table 4.6. *Transmission line parameters calculated for the experimental LEPRE PEA cell components and samples under test.*

Component	Material	R [kΩ/m]	L[mH/m]	C [μF]	Thickness [m]
HV Electrode	Aluminum	27.11	211.16	0.15	$5 \cdot 10^{-3}$
Semiconductor	Semiconductor	359.71	70	10	$2 \cdot 10^{-3}$
Sample	RS 2134	359.71	70	10	$0.69 \cdot 10^{-3}$
Ground Electrode	Aluminum	27.11	211.3	0.11	$10 \cdot 10^{-3}$
Sensor	PVDF	9.74	139	1.4	$9 \cdot 10^{-6}$
Absorber	PVDF	9.74	139	1.4	$250 \cdot 10^{-6}$
Bottom Electrode	Aluminum	27.11	211.16	0.15	$10 \cdot 10^{-3}$

As regard the magnitude of voltage from the pulse generators (see Figure 4.1), 500 V is used, which is the same value of that applied in the experimental test.

Simulation result is shown in Figure 4.15. As it can be seen, a reflection occurs within the main output signal and, furthermore, all of the peaks are at the same position of those obtained by experimental test of Figure 4.14.

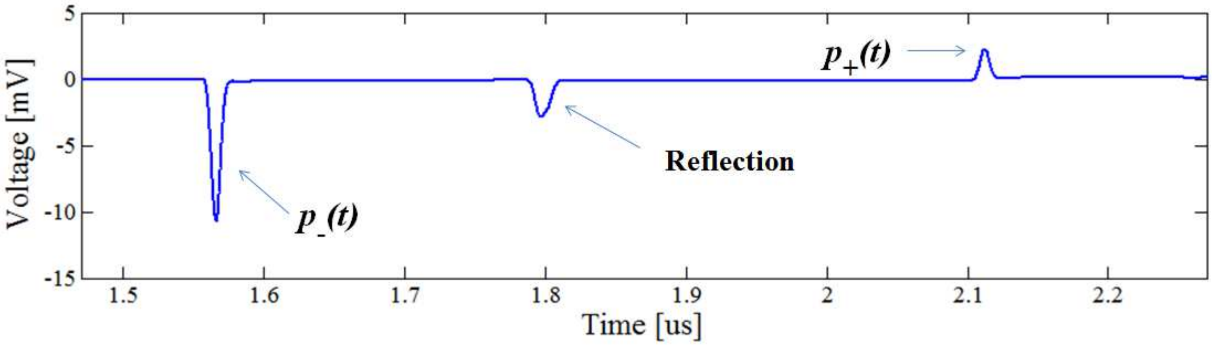

Figure 4.15. *Output of the PEA cell carried out by simulation test. Validation of the model by implementing the PEA cell of the LEPRE laboratory.*

Chapter 5

Multilayer specimens

This chapter deals with the case in which surface and interfacial charges accumulate in two different dielectric materials placed in contact with each other. This configuration will be described by the Maxwell capacitor, while the accumulated charges will be calculated by means of the Maxwell-Wagner theory.

After the evaluation of the surface and interfacial charges, the middle part of this chapter focuses on the study of the waves behavior within the PEA cell, when a two layers specimen is placed between HV and ground electrodes. Therefore, as previously made for a single layer specimen, the relationships useful for the correct sizing of the ground electrode and absorber, that should be satisfied in order to avoid reflections within the main PEA cell output signal, are reported.

Finally, the developed model, for the two layers specimen, has been validated by comparing simulation and experimental results. The latter have been obtained by means of the same real PEA cell of the TDHVL, used in the previous chapter.

5.1 Maxwell capacitor and Maxwell-Wagner theory

The configuration composed of two different dielectric materials "A" and "B" (with different permittivity ε and conductivity γ) placed in contact to eachother, can be described by the Maxwell capacitor [133], as shown in Figure 5.1.

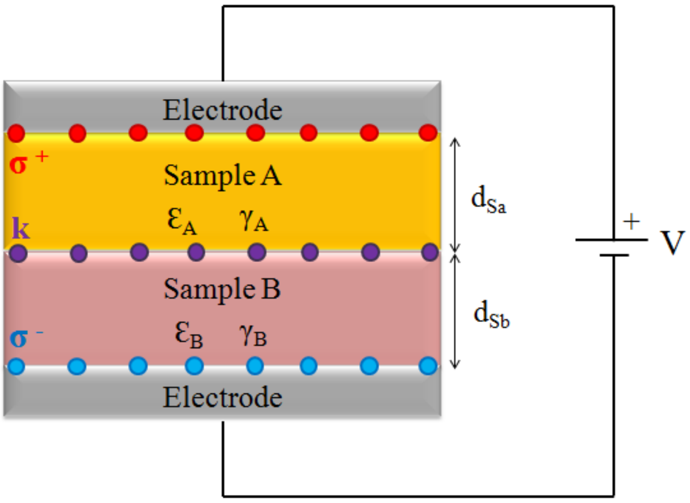

Figure 5.1. *Maxwell capacitor*

In the situation depicted in the figure above, the electric field distribution in samples A and B are given by:

$$E_A = \frac{\gamma_B}{d_{Sb}\gamma_A + d_{Sa}\gamma_B} V \left(1 - e^{-\frac{t}{\tau}}\right) + \frac{\varepsilon_B}{d_{Sb}\varepsilon_A + d_{Sa}\varepsilon_B} V e^{-\frac{t}{\tau}} \tag{5.1}$$

$$E_B = \frac{\gamma_A}{d_{Sb}\gamma_A + d_{Sa}\gamma_B} V \left(1 - e^{-\frac{t}{\tau}}\right) + \frac{\varepsilon_A}{d_{Sb}\varepsilon_A + d_{Sa}\varepsilon_B} V e^{-\frac{t}{\tau}} \tag{5.2}$$

where V is the applied voltage, d_{Sa} and d_{Sb} are the thicknesses of sample A and B, while τ is the time constant given by:

$$\tau = \frac{d_{Sb}\varepsilon_A + d_{Sa}\varepsilon_B}{d_{Sb}\gamma_A + d_{Sa}\gamma_B} \tag{5.3}$$

For the time t tending to zero, the first terms of equations (5.1) and (5.2) can be neglected and the electric field E_x^c is capacitive distributed[2]. Therefore, equations (5.1 - 5.2) become:

$$E_A^c = \frac{\varepsilon_B}{d_{Sb}\varepsilon_A + d_{Sa}\varepsilon_B} V\, e^{-\frac{t}{\tau}} \tag{5.4}$$

$$E_B^c = \frac{\varepsilon_A}{d_{Sb}\varepsilon_A + d_{Sa}\varepsilon_B} V e^{-\frac{t}{\tau}} \tag{5.5}$$

The accumulated surface charges σ_c^+ and σ_c^- , due to E_x^c, in both electrode/sample-A and sample-B/electrode interfaces, can be calculated as:

$$\sigma_c^+ = \varepsilon_A E_A^c = \frac{\varepsilon_A \varepsilon_B}{d_{Sb}\varepsilon_A + d_{Sa}\varepsilon_B} V e^{-\frac{t}{\tau}} \tag{5.6}$$

$$\sigma_c^- = \varepsilon_B E_B^c = \frac{\varepsilon_B \varepsilon_A}{d_{Sb}\varepsilon_A + d_{Sa}\varepsilon_B} V e^{-\frac{t}{\tau}} \tag{5.7}$$

where, in ε_A and ε_B the vacuum permittivity ε_0 is taken into account.

Whereas, if t tends to infinity, the second terms of equations (5.1) and (5.2) tend to zero and

---

[2] The apex *c* is referred to the capacitive distribution of electric field.

the electric field E_x^r is resistive distributed[3]:

$$E_A^r = \frac{\gamma_B}{d_{Sb}\gamma_A + d_{Sa}\gamma_B} V \left(1 - e^{-\frac{t}{\tau}}\right) \tag{5.8}$$

$$E_B^r = \frac{\gamma_A}{d_{Sb}\gamma_A + d_{Sa}\gamma_B} V \left(1 - e^{-\frac{t}{\tau}}\right) \tag{5.9}$$

In this case the accumulated surface charges σ_r^+ and σ_r^- are given by:

$$\sigma_r^+ = \varepsilon_A E_A^r = \frac{\varepsilon_A \gamma_B}{d_{Sb}\gamma_A + d_{Sa}\gamma_B} V \left(1 - e^{-\frac{t}{\tau}}\right) \tag{5.10}$$

$$\sigma_r^- = \varepsilon_B E_B^r = \frac{\varepsilon_B \gamma_A}{d_{Sb}\gamma_A + d_{Sa}\gamma_B} V \left(1 - e^{-\frac{t}{\tau}}\right) \tag{5.11}$$

According to Gauss' law, the accumulated interfacial charge σ_{int} at sample-A/sample-B interface, can be written as follows:

$$\sigma_{r,c}^- - \sigma_{r,c}^+ = \sigma_{int} \tag{5.12}$$

where $\sigma_{r,c}$ is a term that includes both σ_r and σ_c.

During the capacitive distribution of electric field the difference between the surface charges σ_c is zero. Therefore, in equation (5.12) only the surface charges σ_r, due to the resistive distribution of electric field, should be taken into account. However, in the sample-A/sample-B interface of the Maxwell capacitor, due to Maxwell-Wagner effect, the accumulated charge $k(t) = \sigma_{int}$ is given by:

$$k(t) = \left(\frac{\varepsilon_B \gamma_A - \varepsilon_A \gamma_B}{d_B \gamma_A + d_A \gamma_B}\right) V \left(1 - e^{-\frac{t}{\tau_{MW}}}\right) \tag{5.13}$$

where the Maxwell-Wagner time constant, τ_{MW}, is the same of τ described in equation (5.3) [133-134].

---

[3] The apex r is referred to the resistive distribution of electric field.

5.2 Reflections of acoustic waves in a two layers specimen

In case of a free space charge two layers specimen, the main output signal is constituted by three peaks due to the accumulated surface charges in the three interfaces, such as electrode/sample-A, sample-A/sample-B and sample-B/electrode interfaces. As in the case of a single layer specimen, reflections in a two layer specimen may overlap the main output signal of the PEA cell if the ground electrode and the absorber are not properly sized [134].

5.2.1 Acoustic wave reflections within the ground electrode in a two layers specimen

In the situation depicted in Figure 5.2, for two layers specimen, the generated acoustic wave $p_+(t)$, in the HV-electrode/sample-A interface, needs a time $\tau_{\mathrm{Sa}} + \tau_{\mathrm{Sb}} + \tau_{\mathrm{GR}}$ to reach the transducer. As previously explained in Paragraph 2.4, when $p_+(t)$ passes through the different interfaces, it is partially transmitted and partially reflected. The reflected portion of $p_+(t)$, named $p_+^{R-A}(t)$ in Figure 2.3, is not considered in the following, because it needs a time greater than $p_+(t)$ itself to reach the transducer, and thus it does not cause overlap in the main signal. However, $p_+(t)$ is described by:

$$p_+(t) = K_{TOT}\left[\sigma^+ + \frac{1}{2}\varepsilon e_p(t - \tau_{\mathrm{Sa}} - \tau_{\mathrm{Sb}} + \tau_{\mathrm{GR}})\right] e_p(t - \tau_{\mathrm{Sa}} - \tau_{\mathrm{Sb}} - \tau_{\mathrm{GR}}) \quad (5.14)$$

where $K_{TOT} = K_{AL-A}^{G}\, K_{A-B}^{T}\, K_{B-AL}^{T}\, K_{AL-PVDF}^{T}$, in which K_{A-B}^{T} is the transmission coefficient of the sample-A/sample-B interface.

The equation describing the propagated acoustic wave $p_{int}(t)$, due to the sample-A/sample-B interfacial charge, is given by the following equation:

$$p_{int}(t) = K_{A-B}^{G}\, K_{B-AL}^{T}\, K_{AL-PVDF}^{T}\left[\sigma^+ + \frac{1}{2}\varepsilon e_p(t - \tau_{\mathrm{Sb}} + \tau_{\mathrm{GR}})\right] e_p(t - \tau_{\mathrm{Sb}} - \tau_{\mathrm{GR}}) \quad (5.15)$$

where K_{A-B}^{G} is the generation coefficient in the sample-A/sample-B interface.

While, $p_-(t)$ and its reflection $p_-^{R_G}(t)$ within the ground electrode, have been already given in equations (2.32) and (2.37).

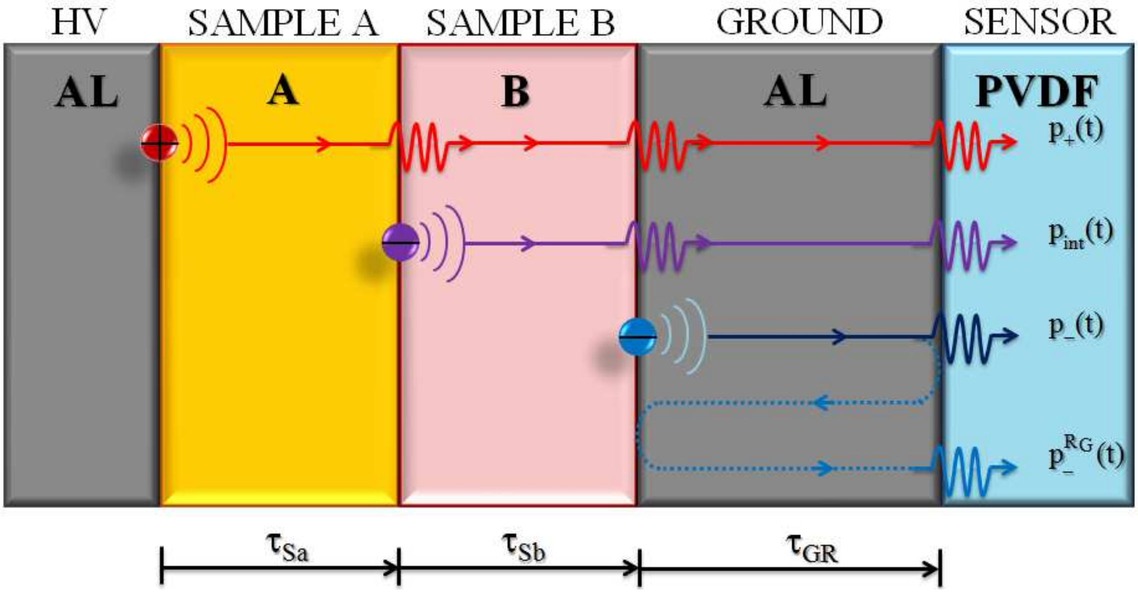

Figure 5.2. *Reflection of acoustic waves in a free space charge two layers specimen. The effect of ground electrode thickness.*

However, if $p_-^{R_G}(t)$ reaches the transducer before than $p_+(t)$ a reflection occurs in the main signal. In order to avoid this problem, the ground electrode should be sized according to the following relationship:

$$d_{GR} > \frac{1}{2}\left(d_{Sa}\frac{v_{AL}}{v_A} + d_{Sb}\frac{v_{AL}}{v_B}\right) \tag{5.16}$$

where v_A and v_B are the speed of sound of materials A and B, respectively.

5.2.2 Acoustic wave reflections within the absorber in a two layers specimen

As in the case of one layer, for a two layers specimens, also the absorber plays an important role in the reflections phenomenon. With respect to Figure 5.3, the expressions of the waves that propagate up to the sensor, such as $p_+(t)$, $p_-(t)$ and $p_{int}(t)$, have been already reported in equations (5.14) (2.32) and (5.15), as well as the reflected acoustic wave within the absorber $p_-^{R_{ABS}}(t)$, described in equation (2.40). The reflections phenomenon within the absorber has been widely analyzed for one layer specimen in the Paragraph 2.4 and it was found that only $p_-^{R_{ABS}}(t)$ could anticipate $p_+(t)$. The latter wave, in case of two layers specimen, takes more time to reach the sensor and therefore the absorber thickness should be greater than that found for one layer specimen. However, the following relationship must be satisfied:

$$d_{ABS} > \frac{1}{2}\left(d_{Sa}\frac{v_{PVDF}}{v_A} + d_{Sb}\frac{v_{PVDF}}{v_B}\right) \tag{5.17}$$

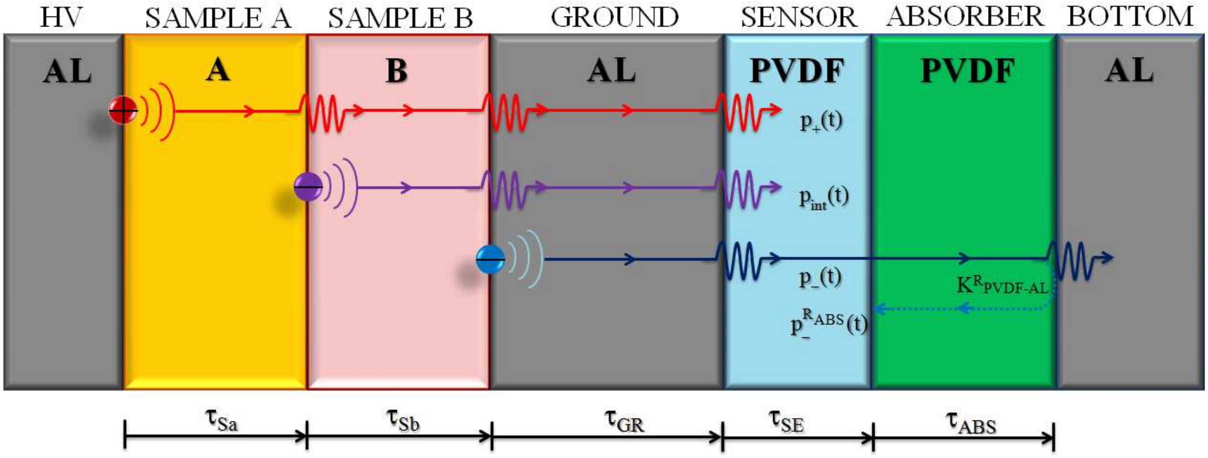

Figure 5.3. *Reflection of acoustic waves in a free space charge two layers specimen. The effect of absorber thickness.*

5.3 Equivalent circuit of the PEA cell for a two layers specimen

The simulated electrical equivalent circuit of the PEA cell, in case of a two layers specimen, is shown in Figure 5.4. Compared to the circuit for one layer, reported in Figure 4.1, a further pulse source is inserted between the transmission lines referred to the two samples. This source is used to simulate the acoustic wave generated by the interfacial charge deposited in the sample-A/sample-B interface. The polarity of the interfacial charge depends on the features of the materials in contact. In particular, if the conductivity of sample B (which is in contact with the negative ground electrode) is greater than conductivity of sample A, the interfacial charge sign is negative. However, both polarity and amount of this charge can be easily calculated by using the Maxwell-Wagner theory (equation (5.13)).

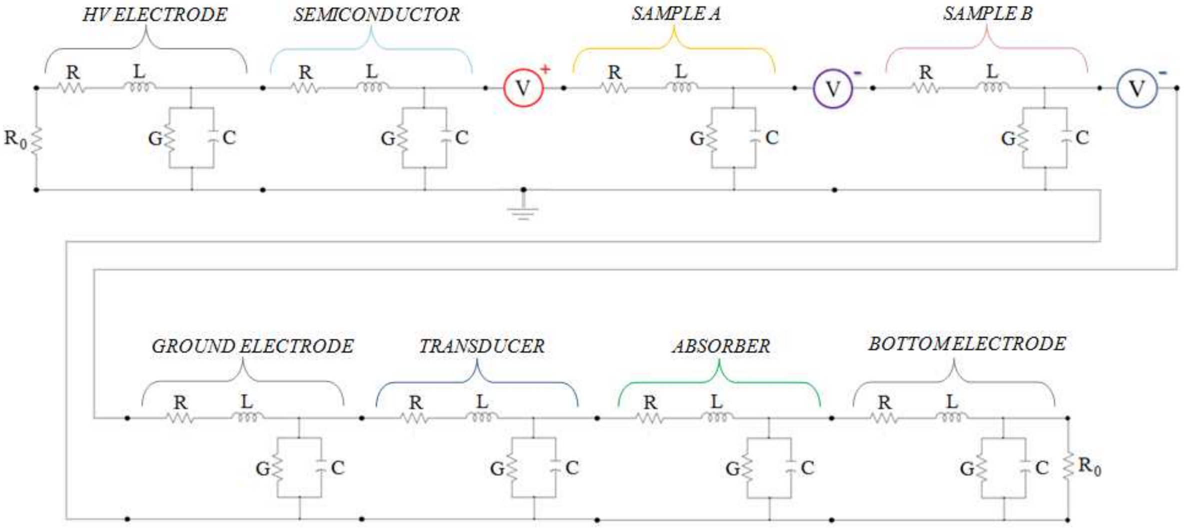

Figure 5.4. *Equivalent electric circuit of the PEA cell for two layers specimen.*

5.4 Evaluation of accumulated surface and interfacial charges in a two layers specimen

Considering the sample A made of XLPE with thickness 280 μm and the sample B made of LDPE with thickness 180 μm, their physical properties and transmission line parameters are the same as those reported in the previous Tables 4.3 and 4.4. The electrical properties useful to calculate the interfacial charge due to the Maxwell-Wegner effect are reported in table 5.1.

Table 5.1. *Electrical properties of the LDPE and XLPE*

Material	Relative permittivity ε_r	Conductivity γ [S/m]
XLPE	2.3	$5 \cdot 10^{-16}$
LDPE	2.2	$7 \cdot 10^{-17}$

For a DC stress equal to 2 kV, the electric field behavior in the XLPE and LDPE samples, calculated by using equations (5.1) and (5.2) is shown in Figure 5.5. According to equations (5.6 - 5.7) and (5.10 - 5.11), the surface charges behavior, during the capacitive and resistive distribution of electric field, is shown in Figure 5.6. In the same figure, the interfacial charge profile (k) calculated by using equation (5.13) is also reported. As it can be noted, in the steady state, the accumulated surface charges in correspondence of the HV-electrode/XLPE and LDPE/ground-electrode interfaces result $\sigma^{+}= 0.27 \cdot 10^{-4}$ C/m² and $\sigma^{-}= - 1.67 \cdot 10^{-4}$ C/m². Whereas, the interfacial charge in the XLPE/LDPE interface is calculated as $k = 1.40 \cdot 10^{-4}$.

The magnitudes of the pulse sources, inserted in the equivalent electric circuit shown in Figure 5.4, are chosen proportionally to the amount of surface and interfacial charges. In particular, the magnitude of the blue generator, which simulates the acoustic wave generated by σ^{-}, is chosen as 600 V. While, because σ^{+} is around 6 times smaller than σ^{-}, the magnitude of the red generator is selected to 100 V. As regard the interfacial charge k, which is 1.2 times smaller than σ^{-}, the magnitude of its corresponding generator (the violet one) is calculated equal to 500 V.

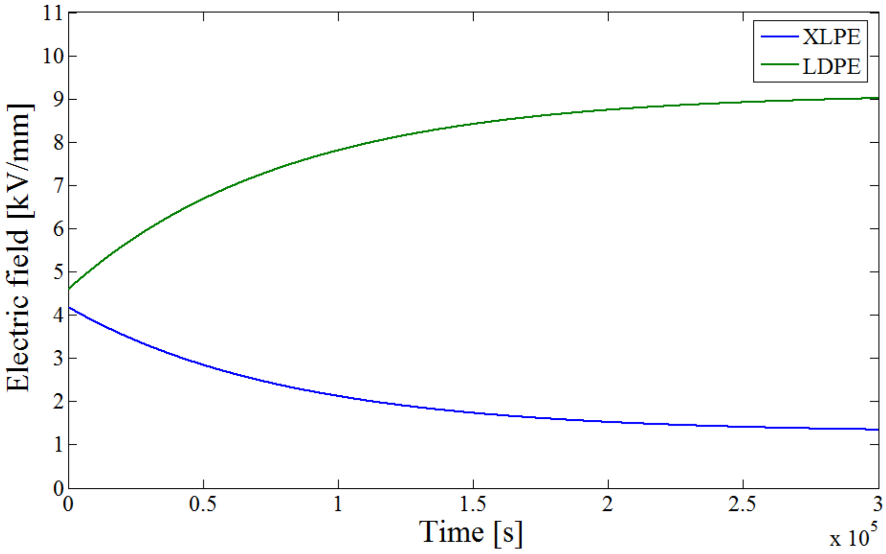

Figure 5.5. *Electric field profiles in XLPE and LDPE samples.*

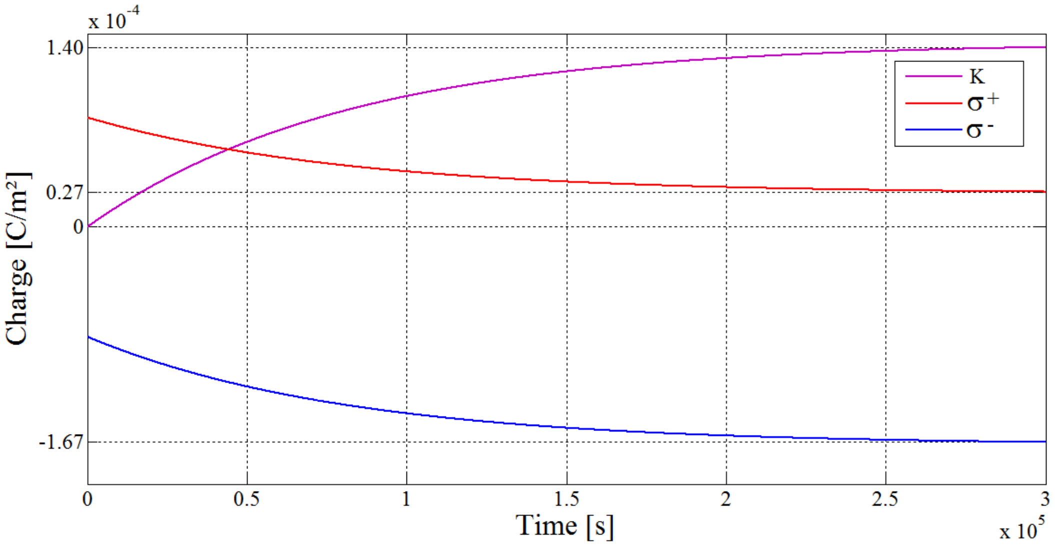

Figure 5.6. *Surface and interfacial charges profiles in the XLPE-LDPE specimen.*

5.5 Simulations results for a two layers specimen

Simulations are carried out by implementing the same PEA cell described in Paragraph 4.3. In Table 4.4 of the previous chapter, the transmission lines parameters useful to simulate the equivalent circuit of Figure 5.4, are also reported.

As regards the pulse sources, for a 2 kV DC stress the magnitudes of these generators have been already calculated: blue generator 600 V, violet generator 500 V, red generator 100 V.

5.5.1. Importance of ground electrode thickness in a two layer specimen

In the first simulation, the reflections phenomenon due to the incorrect sizing of the ground electrode is analyzed. As explained in Paragraph 5.2, if the thickness of the ground electrode does not fulfill equation (5.16), the reflection due to $p_{-}(t)$ anticipates the main peak $p_{+}(t)$.
Considering the samples A made of XLPE and the sample B made of LDPE, with thicknesses 280 μm and 180 μm, respectively, and same sound velocity $v_{XLPE} = v_{LDPE} = 2200$ m/s, equation (5.16) can be rewritten as follows:

$$d_{GR} > \frac{1}{2}\left(d_{Sa}\frac{v_{AL}}{v_{XLPE}} + d_{Sb}\frac{v_{AL}}{v_{LDPE}}\right) \tag{5.18}$$

In this situation, the thickness of the ground electrode, d_{GR}, must be greater than 0.64 mm. In fact, if d_{GR} is chosen 0.5 mm, $p_{+}(t)$ reaches the transducer after 0.285 μs, while the reflected wave $p_{-}^{R_G}(t)$ after 0.231 μs (see also Figure 5.2). Therefore, a reflection occurs before the peak due to the positive surface charge, as shown in Figure 5.7.
On the contrary, if d_{GR} is equal to 0.80 mm, $p_{+}(t)$ and $p_{-}^{R_G}(t)$ reach the transducer after 0.332 μs and 0.372 μs, respectively. Therefore, no reflection occurs in the main signal.

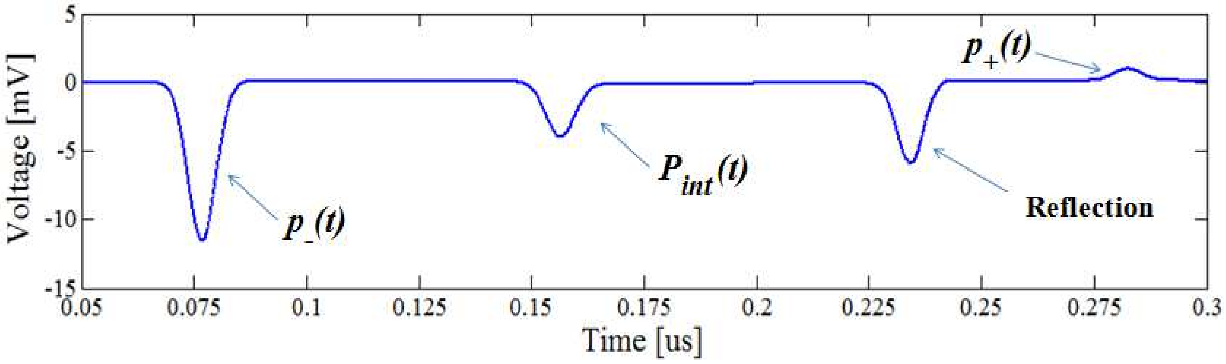

Figure 5.7. *Output of the PEA cell. A reflection is present in the original signal due to the incorrect thickness of the ground electrode*

5.5.2. Importance of absorber thickness in a two layer specimen

As regard the correct sizing of the absorber, equation (5.17) must be satisfied in order to avoid that reflections are present in the main signal. In case of the same two layers specimen used in the previous simulation test, the absorber thickness must be greater than 0.23 mm. In fact, as described for the Figure 5.3, if the ground electrode thickness is properly sized (d_{GR} = 2 mm, which is the thickness of the real PEA cell employed for the experimental tests) the acoustic wave $p_{+}(t)$ reaches the sensor after 0.519 μs, while $p_{-}(t)$ and $p_{int}(t)$ after 0.311 μs and 0.392 μs, respectively. In this case no reflection occurs if the absorber is properly sized as well. While, if the thickness of the absorber is smaller than 0.23 mm and chosen, for example, 0.18 mm, the reflected wave $p_{-}^{R_{ABS}}(t)$ reaches the sensor after 0.469 μs. Therefore a reflection occurs in the main signal, as shown in Figure 5.8.

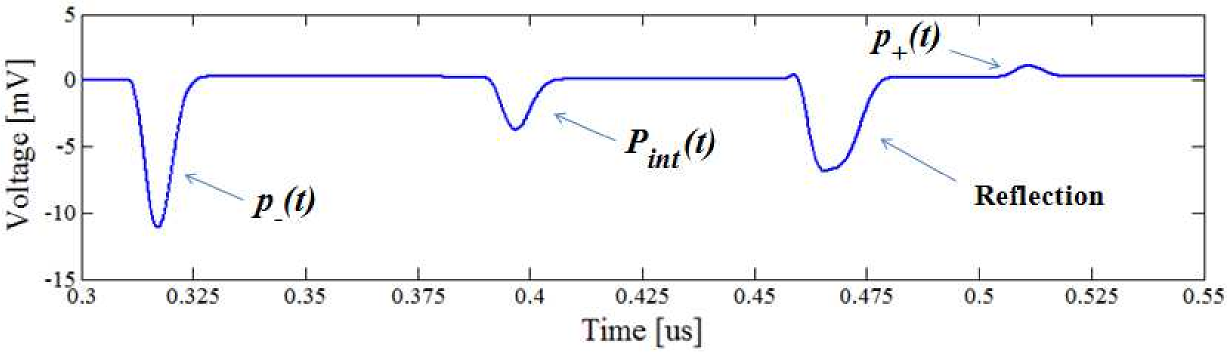

Figure 5.8. *Output of the PEA cell. A reflection is present in the original signal due to the incorrect thickness of the absorber*

5.6 Experimental validation of the two layers specimen model

In order to validate the two layers specimen model, the real PEA cell of the TDHVL, with component dimensions and transmission line parameters reported in Table 4.4, is used for both simulation and experimental tests. The specimen is constituted by the same materials previously described and employed in the simulations, such as 280 μm tick XLPE and 180 μm tick LDPE. By stressing the specimen with 2 kV DC voltage supply, the amount of surface charges and interfacial charge in the steady state have been already calculated in Paragraph 5.4.

Considering that the space charge accumulation phenomenon depends also on the voltage application time, the latter should be small in order to avoid the presence of space charges in the insulation bulk. For this reason, the test time is chosen 5 minutes (300 s). For this time interval, the electric field behavior in the XLPE and LDPE samples is shown in Figure 5.9.

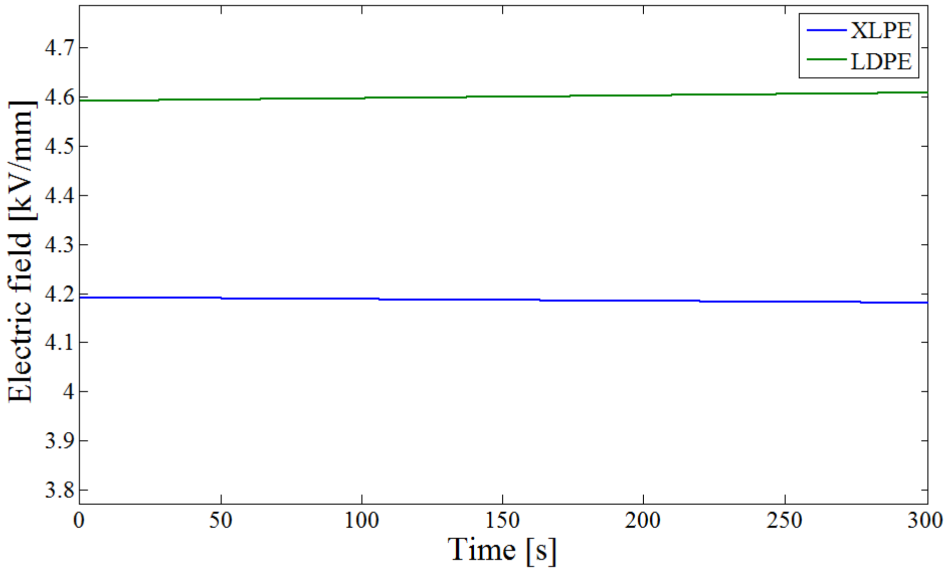

Figure 5.9. *Electric field profiles in XLPE and LDPE samples during 5 minutes of applied voltage.*

While, the accumulated surface and the interfacial charges are reported in Figure 5.10.

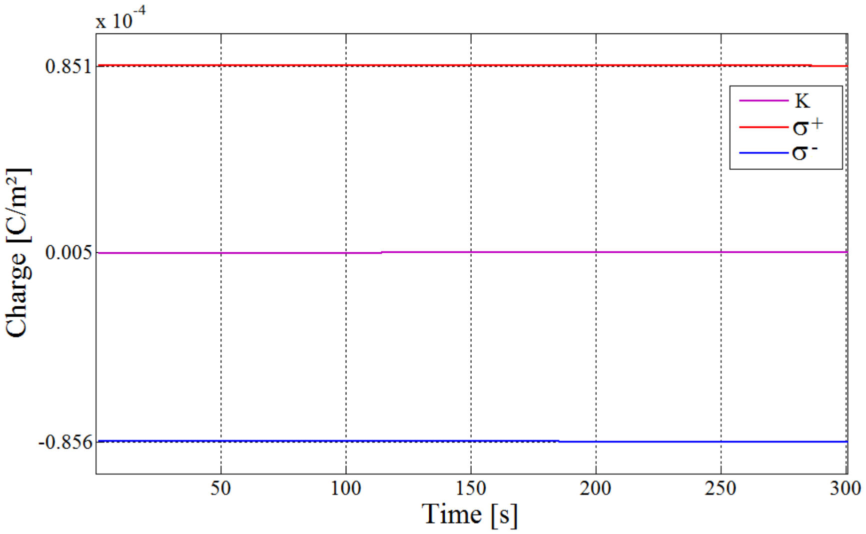

Figure 5.10. *Surface and interfacial charges profiles in the XLPE-LDPE specimen during 5 minutes of applied voltage.*

As it can be seen, after 5 minutes, the accumulated surface charge σ^+ in the HV-electrode/XLPE interface is equal to $0.851 \cdot 10^{-4}$ C/m², whereas the negative surface charge σ^- in the LDPE/ground-electrode interface is equal to $-0.856 \cdot 10^{-4}$ C/m². Instead, in the XLPE/LDPE interface, the accumulated charge k results $0.005 \cdot 10^{-4}$ C/m². According to the found charge values, and observing the equivalent electric circuit of Figure 5.4, the blue generator (which is referred to σ^-) is assigned a magnitude of 600 V. While, considering that σ^+ is 1.006 times smaller than σ^-, the magnitude of the red generator is calculated 596 V (that is 1.006 times smaller than 600 V). Finally, the interfacial charge k is 171 times smaller than

σ^-, therefore the magnitude of the violet generator results 3.5 V.

Considering that the PEA cell described in Table 4.4 is properly sized (d_{GR} = 2 mm and d_{ABS} = 0.45 mm), no reflections occur, and therefore only three peaks due to $p_+(t)$, $p_-(t)$ and $p_{int}(t)$ are present in the main PEA cell output signal. By taking into account a time delay equal to 0.022 µs, present in the output signal of the experimental PEA cell, $p_-(t)$ reaches the sensor after 0.333 µs, $p_{int}(t)$ after 0.414 µs and $p_+(t)$ after 0.541 µs.

Introducing the time delay in the model, simulation result is shown in Figure 5.11. The charge distribution obtained by experimental test is shown in Figure 5.12. Also in this case the calibration technique has been applied in the experimental pattern and therefore the y-axis represents a charge signal. Unlike the pattern obtained by simulation in which the y-axis represents a voltage signal. As previously explained, the times in which the peaks occur remain unchanged and therefore the comparison can be made.

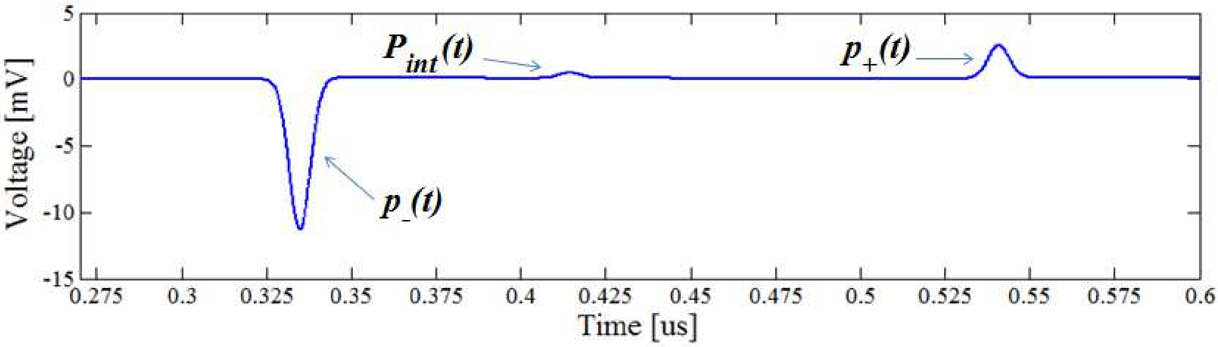

Figure 5.11. *Output of the PEA cell obtained by simulation test for XLPE-LDPE specimen.*

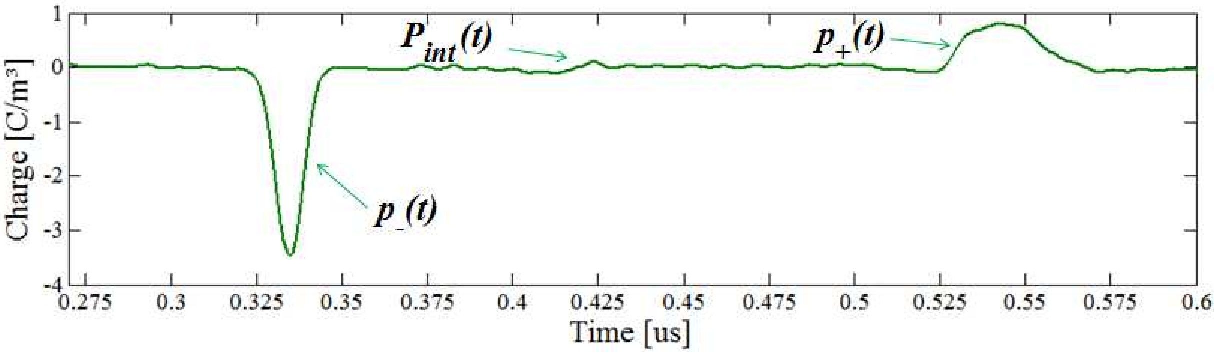

Figure 5.12. *Charge pattern obtained by experimental test for XLPE-LDPE specimen.*

Chapter 6
Recommendations

Research results show that each different PEA cell is able to provide a main output signal without reflections only if the thickness and speed of sound of the sample under test fall within a certain range of values.

On the basis of the results achieved in this thesis work, important recommendations useful to avoid reflections within the main PEA cell output signal are presented in the following for both an already built PEA cell and for a new PEA.

This Chapter, as well as the main part of this thesis, focuses only on the ground electrode and absorber components sizing, because only these parts are responsible of the reflections within the main output signal, which is the most relevant issue in the PEA technique deployment.

6.1 Existing PEA cell

When we have an already built PEA cell, it is not possible to change any component of the PEA cell and therefore the types of dielectric samples that are to be tested are limited. Before each space charge measurement, we recommend to use the following procedure:

1) Measure the thickness of ground electrode d_{GR}, if it is not reported in the operating manual of the used PEA cell. This measurement can be easily made by using some mechanical tool, e.g. caliber or meter. After that, calculate the maximum sample thickness that can be tested in order to avoid reflections in the main output signal, due to the ground electrode thickness. This value can be calculated by the relationship $d_{Sa} < 2\, d_{GR} v_A / v_{AL}$, which is derived from equation (2.38). Where, the speed of sound of the aluminum v_{AL} is typically 6420 m/s, while the speed of sound of the sample v_A is different for each type of dielectric material.

   Based on the above, in order to quickly evaluate the maximum sample thickness d_{Sa}, with sound velocity ranging from 1200 to 3600 m/s (typical values of sound velocity in dielectric materials), that can be tested in a PEA cell with a certain ground electrode thickness value d_{GR}, the graph of Figure 6.1 can be used.

   For example, for the PEA cell of the LEPRE lab, with d_{GR}= 10 mm (pink line of Figure 6.1), if a sample of XLPE material (with sound velocity v_A= 2200 m/s) is to be tested, its maximum thickness d_{Sa} must be lower than 6.9 mm. While, if v_A is lower and equal to 1800 m/s, the maximum d_{Sa} that can be tested in the same PEA cell, without reflections in the main output signal, must be lower than 5.6 mm.

In case of the PEA cell of the TDHVL lab, with d_{GR}= 2 mm, the maximum XLPE sample thickness that can be tested must be no greater than 1.4 mm.

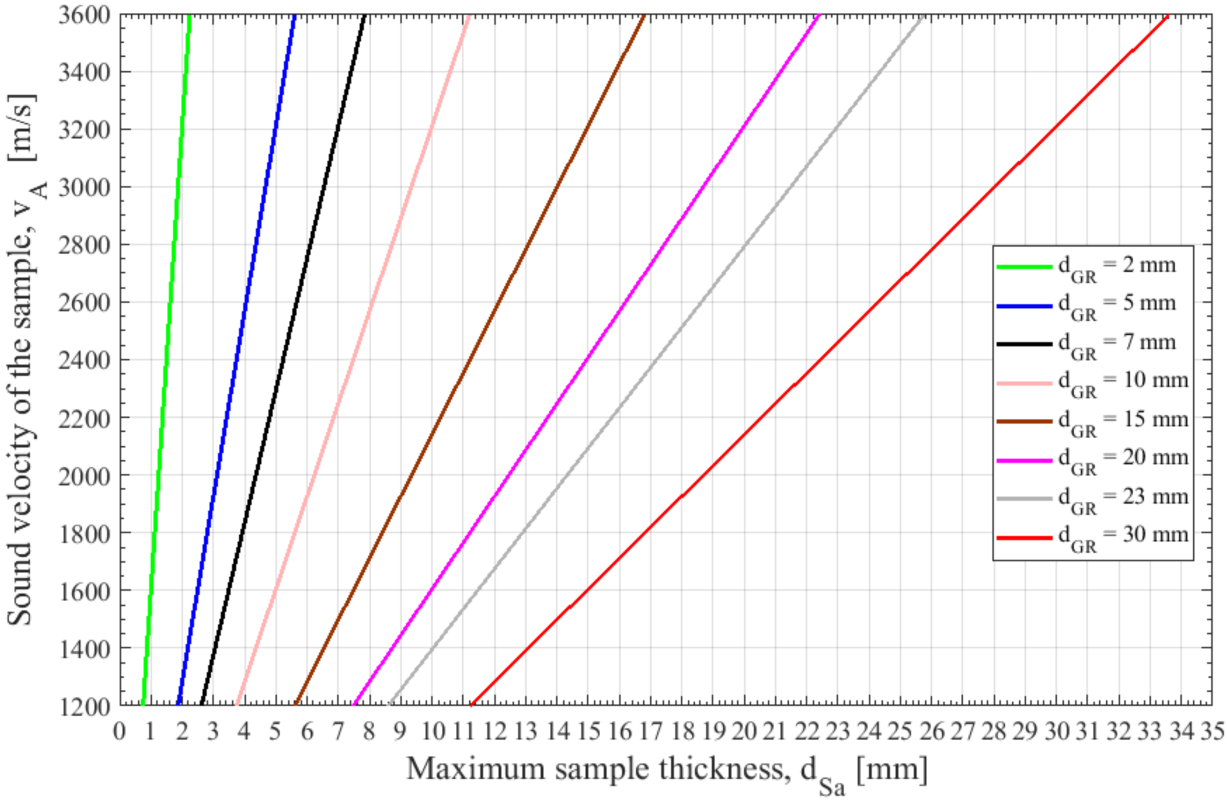

Figure 6.1. *Evaluation of the maximum sample thickness that can be tested, based on the ground electrode thickness of a PEA cell already built.*

2) Measure the thickness of the absorber, if it is not reported in the operating manual of the used PEA cell. In this case, instead, because it is usually placed within an aluminum block and thus it is not easily accessible, the manual measurement of its thickness results difficult. However, its thickness can be evaluated by observing the output signal of the PEA cell displayed into the oscilloscope, by following the procedure below:

- Choose a sample that has both a high speed of sound and the smallest thickness (in the range of μm), among those available in the laboratory. In this way, the possibility of reflections in the main output signal should be avoided.
- Provide both high voltage and pulse voltage to the PEA cell, in which the previous chosen sample has been inserted, as a normal space charge measure.
- Observe the PEA output signal in the oscilloscope. If the chosen sample is correct, no reflections occur in the main signal and thus the first and the second peak displayed in the oscilloscope will be the signals due to the negative and positive charges, respectively.

- In the oscilloscope, move along the positive direction of time axis, until the first reflection of the negative main peak. This reflection could be that within the ground electrode or that within the absorber. It will be that within the ground electrode if the temporal distance between it and the main negative peak is equal to $3\tau_{GR}$ (where $3\tau_{GR}$ is the needed time for an acoustic wave to reach the sensor after being reflected within the ground electrode, calculated as $3\tau_{GR} = 3\,d_{GR}/v_{AL}$, see Figure 2.3.). While, if this temporal distance is different from $3\tau_{GR}$, it means that the first reflected wave after the main signal is the one within the absorber. Therefore, the absorber thickness d_{ABS}, neglecting the sensor effect, can be calculated as:

$$d_{ABS} = \frac{t_{P\_^{R_{ABS}}} - t_{p\_}}{2} v_{PVDF} \tag{6.1}$$

Where $t_{p\_}$ and $t_{P\_^{R_{ABS}}}$ are the corresponding times of the main negative peak and its first reflection, respectively. While, the sound velocity of the absorber made of PVDF material is always v_{PVDF} = 2260 m/s.

To better understand what above explained, in Figure 6.2 an example is reported. The signal in the figure is the same of that previously obtained by simulation in Chapter 4, which results very similar to that displayed in the oscilloscope. As it can be seen, $t_{p\_}$ is equal to 3.58 μs, while $t_{P\_^{R_{ABS}}}$ is around 3.8 μs. Therefore, by means of equation (6.1), the absorber thickness is calculated $d_{ABS} \approx 250$ μm.

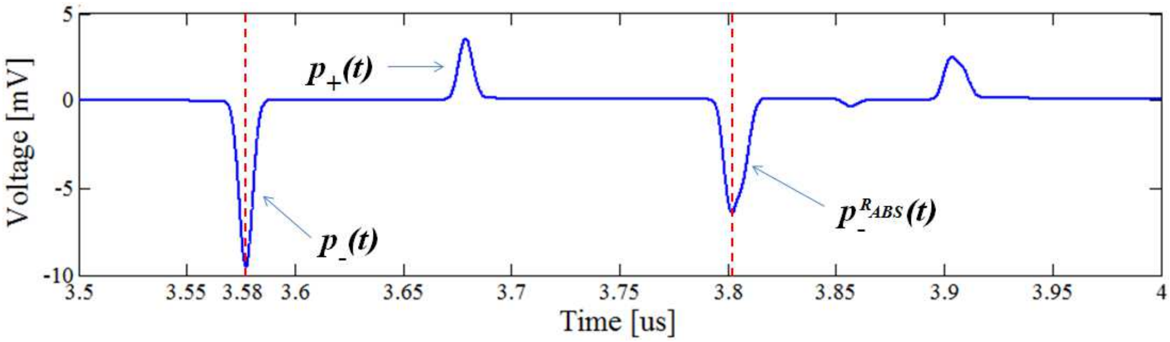

Figure 6.2. *Evaluation of the absorber thickness by means of PEA cell output signal.*

- After having obtained the absorber thickness, calculate the maximum sample thickness that can be tested in order to avoid reflections in the main output signal, due to the absorber thickness. This value can be calculated by the relationship $d_{Sa} < 2\,d_{ABS} v_A / v_{PVDF}$ which is derived from equation (2.41).

Also in this case, a graph can be used in order to quickly evaluate the maximum sample thickness d_{Sa} that can be tested in a PEA cell with a certain absorber thickness value d_{ABS}. For example, for the PEA cell of the LEPRE lab, with d_{ABS}= 250 µm, the maximum sample thickness d_{Sa} that can be tested must be lower than 0.49 mm, if its sound velocity v_A is equal to 2200 m/s. While, if v_A= 3000 m/s, for the same d_{ABS} value, d_{Sa} must be lower than 0.67 mm.

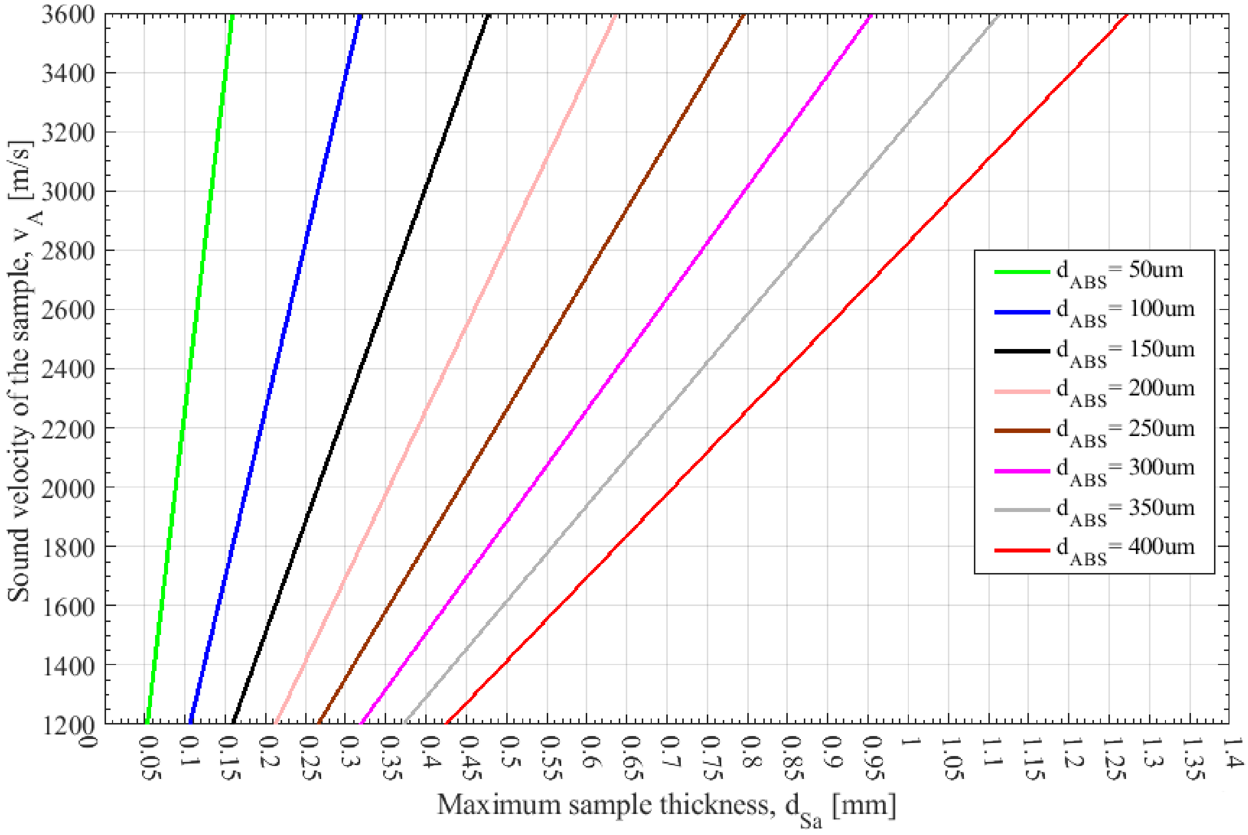

Figure 6.2. *Evaluation of the maximum sample thickness that can be tested, based on the absorber thickness of a PEA cell already built.*

6.2 PEA cell design

A PEA cell is designed on the basis of the specimen's features (thickness and sound velocity). Based on the results obtained in this thesis, in order to avoid reflection in main PEA cell output signal, we recommend to use the equations already given in Chapter 2, and again reported below in equation (6.2) for the ground electrode sizing, and in equation (6.3) for the absorber sizing.

$$d_{GR} > \frac{1}{2} d_{Sa} \frac{v_{AL}}{v_A} \qquad (6.2)$$

$$d_{ABS} > \frac{1}{2} d_{Sa} \frac{v_{PVDF}}{v_A} \tag{6.3}$$

Based on the above equations, two graphs have been realized in order to facilitate the design. The graph referred to the ground electrode thickness, is shown in Figure 6.3. Where, each line with different color is referred to a maximum sample thickness value that should be tested. While, in the y-axis the typical range of dielectric materials sound velocity values is reported. Therefore, after having chosen the maximum sample thickness value and knowing its sound velocity, the minimum ground electrode thickness is provided by the x-axis. For example, if the PEA cell must be used to test specimens with maximum thickness d_{Sa} = 800 µm (black line of Figure 6.3) and sound velocity v_A = 2400 m/s, the thickness of the ground electrode,d_{GR} must be greater than 1.1 mm. While, if d_{Sa} = 2 mm and v_A = 2000 m/s, d_{GR} must be at least 3.2 mm. In case of two layers specimens, the minimum ground electrode thickness is given by the sum of each d_{GR} calculated separately for each sample composing the specimen. Therefore, considering the examples above, in which d_{GR} has been calculated 1.1 and 3.2 mm for the two different samples, if both samples are placed in contact to each other in order to be tested, the minimum d_{GR} value must be greater than the sum of 1.1 and 3.2 mm, and thus d_{GR} > 4.3 mm.

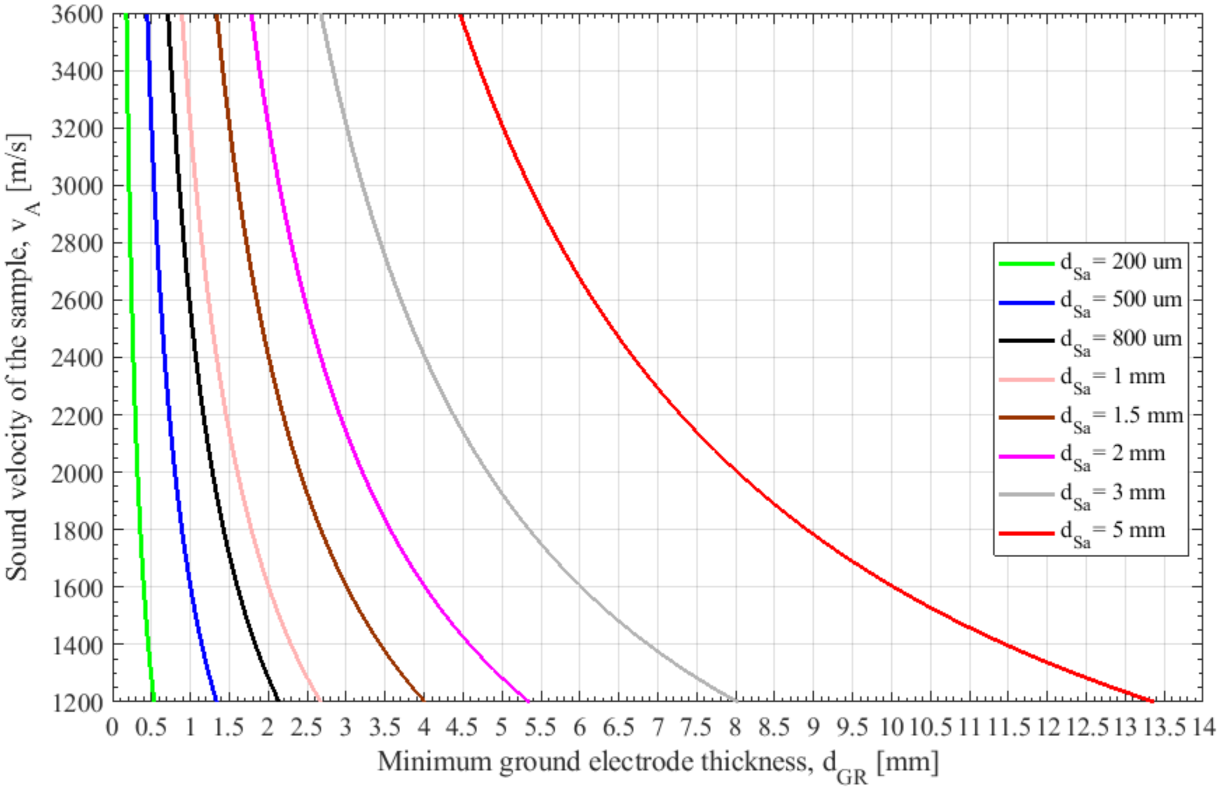

Figure 6.3. *Sizing of the ground electrode thickness, based on the specimen features that should be tested.*

In Figure 6.4, instead, the graph referred to the sizing of the absorber thickness is shown. As in the previous graph of Figure 6.3, after having chosen the maximum sample thickness, based on its sound velocity, the minimum absorber thickness value is given in the x-axis. In this case, if for example d_{Sa} = 2 mm and v_A = 2000 m/s, the minimum absorber thickness that must be used is equal to d_{ABS} = 1.1 mm. For another sample, with d_{Sa} = 500 µm and v_A = 1800 m/s, d_{ABS} minimum results 0.31 mm. If this latter sample is placed in contact to the previous one, for this two layers specimen, the minimum absorber thickness must be greater than 1.1 + 0.31 mm, and thus d_{ABS} > 1.41 mm.

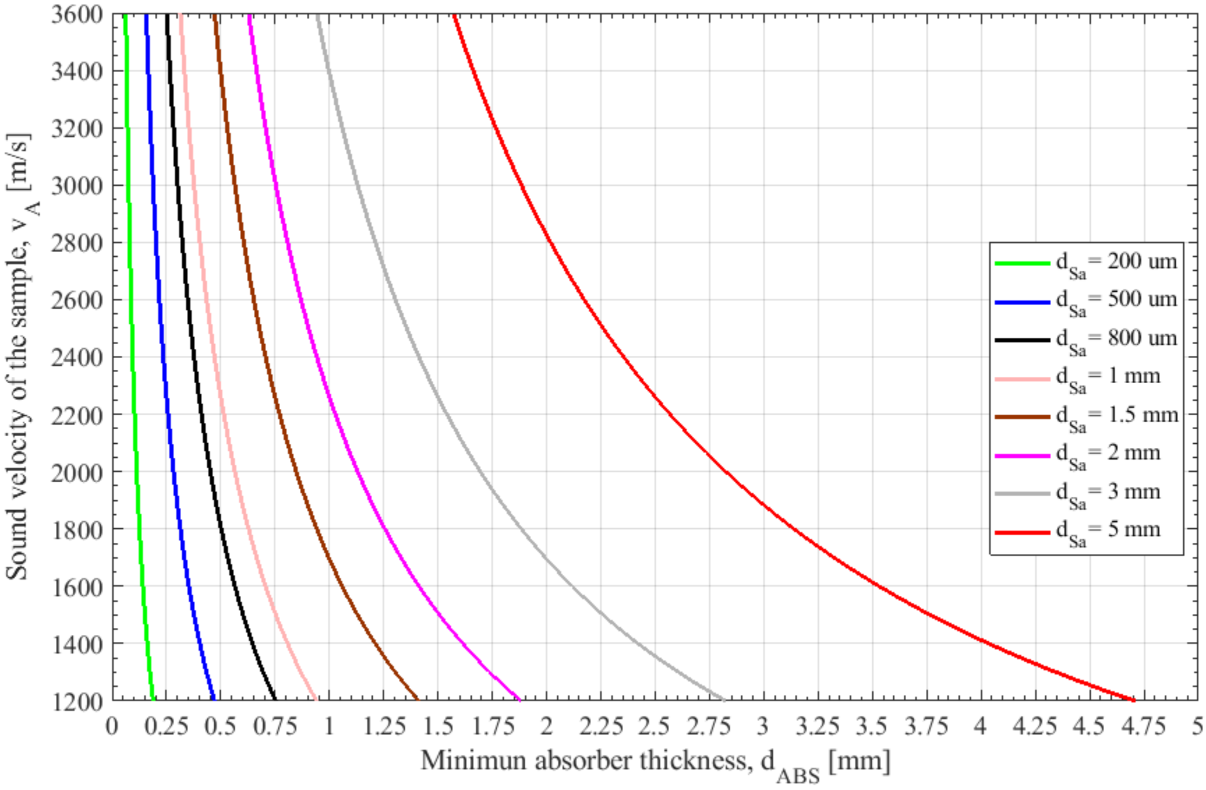

Figure 6.4. *Sizing of the absorber thickness, based on the specimen features that should be tested.*

Chapter 7
Conclusion and future works

The purpose of this work was to develop a simulation model of the PEA method in order to establish the correct sizing of the PEA cell components, with the aim to avoid reflections of acoustic waves within the main output signal.

The employed modeling approach follows the suggestions of a work found in literature in which PSpice software was used to simulate the acoustic waves behavior within the PEA cell. Here, instead, Matlab environment was chosen in order to have a more versatile software in which it was also possible to manage the mathematical equations and study coupled phenomena and parametric variations more easily than in PSpice environment.

The initial simulations have been carried out considering only one dielectric layer in the sample and the presence of only surface charges in the HV-electrode/sample and sample/ground-electrode interfaces. In these simulations, in order to have a better output charge profiles (without overlapping reflections on the main signal) the correct thicknesses of ground electrode and absorber were found.

Initially, the validation of the software was made by comparing the results with those proposed in the referred article. Subsequently, by using the PEA cell of the TDHVL lab, the comparison between simulated and experimental results confirmed the good performance of the developed model.

In addition, the model has also been validated by means of the PEA cell of the LEPRE lab. In this case, a dielectric layer with material properties that fall outside the range allowed by the PEA cell, has been used as a sample. In this way, a reflection coming from the absorber layer and located within the main output signal has been observed in both experimental and simulation test.

As an evolution of the model, specimens made of two different dielectric layers were implemented into the model. Furthermore, the Maxwell-Wagner theory was been used in order to evaluate the amount of interfacial charge interposed between the dielectric/dielectric interfaces. Also in this case simulation results have been confirmed by experimental tests.

In the final part of this thesis, some recommendations have been given. In particular, the provided graphs could be very useful to establish, in an easy and fast way, the sample types that may be tested with a PEA cell already built. Moreover, in case of a PEA design, further graphs were realized in order to evaluate the correct thickness of ground electrode and absorber, on the basis of the specimens that are to be tested. However the limitations of the developed PEA cell model, that will be addressed in future works, are reported in the following:

- The PEA cell output signal obtained by simulations is the one detected by the sensor, without considering the amplifier effect. Therefore, the amplitude of the signal provided by the model is different from that displayed in the oscilloscope during experimental measures. In future works, an amplifier with the same features of those used in the PEA cells will be inserted in the output of the Leach’s impedance-type transducer model implemented in Simulink environment.
- The validation of the model was made by comparing simulation and experimental results, and the latter were obtained after the application of the calibration and deconvolution techniques. Therefore, signals in C/m^3 (in the experimental test) and in mV (in the simulation test) were compared. Despite in the developed model, the axis of interest is that of the time (which remains unchanged), the implementation of the calibration technique in order to obtain a charge signal as a final results can be useful.
- An ideal Gaussian pulse was used as a pulse generator. In future works, an equation able to generate a real pulse generator shape will be implemented into the model.
- The model simulates the presence of only surface charges deposited in correspondence of the sample interfaces. However, if an amount of space charge accumulates in the sample bulk, the related acoustic waves generated by their vibration, after being reflected within the ground electrode or in the absorber, could cause reflections within the main output signal. Therefore, simulations consisting of a specimen containing accumulated space charges will be carried out and the equations providing the minimum thickness of ground electrode and absorber must be revised accordingly.
- The model simulates the PEA cell for flat specimens. In future works, a PEA cell for cables will be studied and implemented into the model, and thus cylindrical geometries simulating a cable will be considered as a sample.

Thanks to the advantages provided by Matlab software, further research work can be carried out, in particular:

- simulations of a three different dielectric layers samples, as it is more relevant to the cable/cable joints.
- simulations of acoustic waves behavior within the PEA cell, for both flat and cable specimens, under different temperature gradient.

APPENDIX

A. Pseudocode of the developed PEA cell model

In this appendix, the pseudoce for a single layer specimen, theoretically described in Chapter 3 of this thesis, is reported.

```
Input the thickness of all PEA cell components (d_component): HV electrode, semiconducting layer, sample, ground electrode, sensor absorber and bottom electrode.

Set spatial step: dz.

Calculate M dimensions for each PEA cell component:
   M_component = round (d_component/dz)

Create and Initialize voltage and current vectors for each PEA cell component (V_component, I_component).

Create and Initialize the transmission line parameter vectors for each PEA cell component: (R_component, L_component, C_component, G_component).

Input the material properties of each PEA cell component: density ($\rho$), acoustic velocity ($v$), attenuation coefficients ($\alpha$) and ($\alpha_{tc}$).

Calculate the transmission line parameters of each PEA cell component: resistance (R), capacitance (C), inductance (L) and conductance (G):
  R_material = 2*$\rho$_material*v_material*area*$\alpha$_material;
  L_material = area*$\rho$_material;
  C_material = 1/area*$\rho$_material*v_material ^2);
  G_material = 2/$\rho$_material*v_material*area)*($\alpha_{tc}$_material);

Set the time step for each PEA cell component:
   dt_material = dz/v_material;

Calculate the parameters P, Q, Y, S (see pag.64) for each PEA cell component:
  P_component = (2*L_component - dt_material* *R_component)./(2*L_component + dt_material* *R_component);
  Q_component = (2*dt_material)./(dt_material*dz*R_component + + 2*dz*L_component);
  Y_component = (2*C_component -G_component* *dt_material)./(2*C_component + G_component *dt_material);
  S_component = (2*dt_material)./(dt_material*dz*G_component + 2*dz*C_component);

Calculate the parameters Y, S of the nodes between two PEA cell components named $i$ (before the node) and $i+1$ (after the node):
  Y_component$^{i}$ - component$^{i+1}$ = (2*(C_ component$^{i}$ (1)+ +C_component$^{i+1}$ (1))/2 (G component$^{i}$ (1)+ G component$^{i+1}$ (1))/2* dt_material)./(2*(C component$^{i}$ (1)+C component$^{i+1}$ (1))/2+(G component$^{i}$ (1)+G component$^{i+1}$ (1))/2*dt_material);
```

```
    S_component$^{i}$- component$^{i+1}$= (2*dt_material)./(dt_material*
    *dz*(G component$^{i}$ (1)+G component$^{i+1}$ (1))/2 + 2*dz*
    *(C_component$^{i}$ (1)+C_component$^{i+1}$ (1))/2);

Set the simulation time: N dimension
//*Create a loop to solve the Telegraphist's equations by means
of the FDTD method:

For n = 1: N
     Input: Pulse generators:
     Vpulse_positive(n)= 600*(exp(-((n-8)^2)/20));
     Vpulse_negative(n)= - 600*(exp(-((n-8)^2)/20));

     Insert the pulse source in correspondence of the sample
     interfaces:
     V_Sample(1) = V_Sample(1) + Vpulse_positive(n);
     V_Sample(M_Sample) = V_Sample(M_Sample) +
     Vpulse_negative(n);

           For m = 2 : M_component - 1, update of the voltage
               V_compoent (m)= Y_compoent (m).*V_compoent(m)+
               +S_compoent (m).*(I_compoent (m-1)-IHV(m));
           end for loop;

           if m == M_component, solve the node equation
               V_component$^{i}$ (M_component$^{i}$) = Y_component$^{i}$ -
               component$^{i+1}$ * V_component$^{i}$ (M_component$^{i}$) +
               S_component$^{i}$ - component$^{i+1}$ *(I_component$^{i}$
               (M_component$^{i}$ -1) -I_component$^{i+1}$ (1));
           end if

     Set the continuity of voltage between the nodes:
     V_component$^{i+1}$(1) = V_component$^{i}$(M_component$^{i}$)

           For m = 1 : M_component - 1, update of the current:
                I_component$^{i}$(m) = P_component$^{i}$(m).*
                *I_component$^{i}$(m)+ Q_component$^{i}$(m).*
                *(V_component$^{i}$ (m)-V_component$^{i}$ (m+1));
           end for loop

     Set the continuity of current between the nodes:
     I_component$^{i}$(M_component$^{i}$)= I_component$^{i+1}$(M_component$^{i+1}$);

     Record the voltage and the current values;

     Show the dynamic simulation of wave behavior within the
     PEA cell;

end for loop

Save Input and Output current of the transmission line simulating
the Sensor;

Comunication with Simulink in which the Leach's Trasducer model
is implemented;

Display the final wave pattern.
```

References

[1] G. Ala, M. Caruso, V. Cecconi, S.Ganci, A. Imburgia, R. Miceli, P. Romano, F. Viola, "Review of acoustic methods for space charge measurement," *2015 AEIT International Annual Conference (AEIT),* Naples, Italy, 2015, pp. 1-6.

[2] A. Imburgia, R. Miceli, E. R. Sanseverino, P. Romano and F. Viola, "Review of space charge measurement systems: acoustic, thermal and optical methods," in *IEEE Transactions on Dielectrics and Electrical Insulation*, vol. 23, no. 5, pp. 3126-3142, October 2016.

[3] A. Imburgia, P. Romano, M. Caruso, F. Viola, R. Miceli, E. Riva Sanseverino, A. Madonia, and G. Schettino, “Contributed Review: Review of thermal methods for space charge measurement”, Review of Scientific Instruments Vol.87, 111501(2016).

[4] G. Mazzanti and M. Marzinotto, “Space charge in HVDC extruded insulation: Storage, effect, and measurement methods,” in Extruded Cables for High Voltage Direct Current Transmission: Advances in Research and Development, Power Engineering Series (Wiley-IEEE Press, New York, USA, 2013), pp. 99–207.

[5] K. R. Bambery and R. J. Fleming, “Space charge accumulation in two power cable grades of XLPE,” IEEE Trans. Dielectr. Electr. Insul. 5(1), pp. 103–109, 1998.

[6] C. Filloy-Corbrion, C. Boue, E. Geron, T. Ditchi, J. Lucas, S. Hole, P. Notingher, S. Agnel, D. Marty-Dessus, L. Berquez, and G. Teyssedre, “Surface temperature measurement for space charge distribution measurements with thermal methods,” IEEE Trans. Dielectr. Electr. Insul. 22(3), pp. 1506–1511, 2015.

[7] R. E. Collins, “Analysis of spatial distribution of charges and dipoles in electrets by a transient heating technique,” J. Appl. Phys. 47, pp. 4804–4808, 1976.

[8] R. E. Collins, “Practical application of the thermal pulsing technique to the study of electrets,” J. Appl. Phys. 51, pp. 2973–2986, 1980.

[9] F. I. Mopsik and A. S. DeReggi, “Numerical evaluation on the dielectric polarization distribution from thermal pulse data,” J. Appl. Phys. 53(6), 4333–4339 (1982).

[10] F. Zheng, Y. Zhang, Z. An, C. Liu, J. Dong, and C. Lin, “Thermal pulse method with an applied field,” in IEEE International Conference on Solid Dielectrics (ICSD) (IEEE, 2013), pp. 427–430.

[11] H. Amjadi, “Thermal-pulse investigation of thermally grown silicon dioxide electrets,” in 9th International Symposium on Electrets (ISE 9) (IEEE, Shanghai, 1996), pp. 259–264.

[12] S. Baudon, P. Notingher, S. Agnel, and S. Hole, “Advances in electric charge measurements in semi-conducting structures by non-destructive thermal methods,” in IEEE Industry Applications Society Annual Meeting October 2014 (IEEE, 2014), pp. 1–7.

[13] S. Aryal and A. Mellinger, “Resolution-enhanced polarization imaging with focused thermal pulses,” J. Appl. Phys. 114, 109–154 (2013).

[14] A. Mellinger, R. Singh, M. Wegener, W. Wirges, R. F. Suarez, S. B. Lang, L. F. Santos, and R. Gerhard-Multhaupt, “High-resolution threedimensional space-charge and polarization mapping with thermal pulses,” in 12th International Symposium on Electrets, ISE-12 (IEEE, 2005), pp. 212–215.

[15] A. Toureille and J. P. Reboul, “The thermal-step-technique applied to the study of charge decay in polyethylene thermoelectrets,” in Proceedings of 6th International Symposium on Electrets (ISE 6) (IEEE, 1988), pp. 23–27.

[16] A. Toureille, P. Notingher, N. Vella, S. Malrieu, J. Castellon, and S. Agnel, “The thermal step technique: An advanced method for studying the properties and testing the quality of polymers,” Polym. Int. 46(2), 81–92 (1998).

[17] P. Notingher, S. Agnel, and A. Toureille, “Recent advances in calculating space charge distribution by processing the signals obtained using the thermal step method,” in Annual Report, Conference on Electrical Insulation and Dielectric Phenomena (IEEE, 1998), Vol. 1, pp.154–157.

[18] G. M. Sessler, “Charge distribution and transport in polymers,” IEEE Trans. Dielectr. Electr. Insul. 4(5), 614–628 (1997).

[19] P. Notingher, S. Hole, S. Baudon, O. Fuchier, L. Boyer, and S. Agnel, “Toward non destructive high resolution thermal methods for electric charge measurements in solid dielectrics and components,” in (ESA) Electrostatics Joint Conference, Cambridge, June 2012.

[20] L. Boyer, O. Fruchier, P. Notingher, S. Agnel, A. Toureille, B. Rousset, and J. Sanchez, “Analysis of data obtained using the thermal step method on a MOS structure—An electrostatic approach,” in IEEE Industry Applications Society Annual Meeting (IAS), pp. 1–6, 2008.

[21] G. Dagher, S. Hole, and J. Lewiner, “A preliminary study of space charge distribution measurements at nanometer spatial resolution,” IEEE Trans. Dielectr. Electr. Insul. 13, pp. 1036–1041, (2006).

[22] C. Stancu et al., “Electric field computation in water treed polyethylene with space charge accumulation,” in Conference Record of the 2006 IEEE International Symposium on Electrical Insulation (IEEE, Toronto, Ontario, 2006), pp. 186–189.

[23] P. Notingher, S. Agnel, and A. Toureille, “Thermal step method for space charge measurements under applied dc field,” IEEE Trans. Dielectr. Electr. Insul. 8(6), pp. 985–994, 2001.

[24] S. Agnel, P. Notingher, and A. Toureille, “Space charge measurements under applied DC field by the thermal step method,” in Annual Report Conference on Electrical Insulation and Dielectric Phenomena (IEEE, 2000), Vol. 1, pp. 166–170.

[25] A. Cherifi, M. A. Dakka, and A. Toureille, “The validation of the thermal step method,” IEEE Trans. Electr. Insul. 27(6), 1152–1158 (1992).

[26] J. Laurentie, H. Yahyaoui, P. Notingher, J. Castellon, and S. Agnel, “Contactless electric field and space charge measurement across solid dielectrics: A fully non-intrusive thermal technique,” in IEEE Industry Applications Society Annual Meeting (IEEE, 2014), pp. 1–4.

[27] A. Hascoat et al., “Study and analysis of conduction mechanisms and space charge accumulation phenomena under high applied DC electric field in XLPE for HVDC cable application,” in 2014 IEEE Conference on Electrical Insulation and Dielectric Phenomena (CEIDP) (IEEE, Des Moines, IA, 2014), pp. 530–533.

[28] J. Castellon, P. Notingher, S. Agnel, A. Toureille, J. Matallana, H. Janah, P. Mirebeau, and D. Sy, “Industrial installation for voltage-on space measurements in HVDC cables,” in Industry Applications Conference, Fourtieth IAS Annual Meeting, Conference Record of the 2005 (IEEE, 2005), Vol. 2, pp. 1112–1118.

[29] P. Notingher, A. Toureille, S. Agnel, and J. Castellon, “Determination of electric field and space charge in the insulation of power cables with the thermal step method and a newmathematical processing,” IEEE Trans. Ind. Appl. 45(1), 67–74 (2009).

[30] G. Platbrood, S. Agnel, A. Toureille, and P. Bulens, “Comparison of new cables and aged cables out of the grid by the Thermal Step Method,” in Annual Report Conference on Electrical Insulation and Dielectric Phenomena (IEEE, 2002), pp. 396–399.

[31] J. Castellon et al., “A new diagnosis of the XLPE insulation with water treeing by space charge measurements with the thermal step method and water nuclear magnetic resonance imaging,” in 2005 Annual Report Conference on Electrical Insulation and Dielectric Phenomena, CEIDP’05 (IEEE, 2005), pp. 536–539.

[32] A. Darkawi, P. Notingher, T. Martire, J. Huselstein, and F. Forest, “Portable installation for space charge measurements on full-size high voltage cable loops based on a multicell power converter,” in Annual Report Conference on Electrical Insulation and Dielectric Phenomena (CEIDP) (IEEE, 2012), pp. 499–502.

[33] G. Mazzanti, G. Chen, J. C. Fothergill, N. Hozumi, J. Li, M. Marzinotto, F. Mauseth, P. Morshuis, C. Reed, A. Tzimas, and W. Kai, “A protocol for space charge measurements in full-size HVDC extruded cables,” IEEE Trans. Dielectr. Electr. Insul. 22(1), 21–34 (2015).

[34] J. M. Reboul, A. Cherifi, and R. Carin, “A new method for space charge measurements in dielectric films for power capacitors,” IEEE Trans. Dielectr. Electr. Insul. 8(5), 753–759 (2001).

[35] J. M. Reboul, F. Mady, M. Rouff, and R. Carin, “A new technique for a complete study of space charge,” in Proceedings of the 7th International Conference on Properties and Applications of Dielectric Materials (IEEE,2003), Vol. 2, pp. 514–517.

[36] J. M. Reboul, “Thermal waves interferences for space charge measurements in dielectrics,” in 14th International Symposium on Electrets (ISE) (IEEE, 2011), pp. 63–64

[37] S. B. Lang and D. K. Das-Gupta, “A technique for determining the polarization distribution in thin polymer electrets using periodic heating,” Ferroelectrics 39, 1249–1252 (1981).

[38] S. B. Lang and D. K. Das Gupta, “A new technique for determination of the spatial distribution of polarization in polymer electrets,” Ferroelectrics 60, 23–36 (1984).

[39] T. Pawlowski, R. J. Fleming, and S. B. Lang, “LIMM study of space charge in crosslinked polyethylene,” IEEE Trans. Dielectr. Electr. Insul. 13(5), 1023–1029 (2006).

[40] S. B. Lang and R. Fleming, “A comparison of three techniques for solving the Fredholm integral equation of the laser intensity modulation method (LIMM),” IEEE Trans. Dielectr. Electr. Insul. 16(3), 809–814 (2009).

[41] V. Griseri, S. Bouchareb, and L. Berquez, “Adaptation of the LIMM technique data treatment to perform measurements in vacuum,” in Annual Report Conference on Electrical Insulation and Dielectric Phenomena (CEIDP) (IEEE, 2012), pp. 491–494.

[42] S. Bouchareb, V. Griseri, and L. Berquez, “In situ space charge profile measurements on electronic irradiated material by LIMM,” in IEEE International Conference on Solid Dielectrics (ICSD) (IEEE, 2013), pp. 776–779.

[43] T. Pawlowski, S. B. Lang, and R. J. Fleming, “Space charge and polarization in crosslinked polyethylene,” in Annual Report Conference on Electrical Insulation and Dielectric Phenomena (CEIDP) (IEEE, 2004), pp. 93–96.

[44] R. J. Fleming, S. B. Lang, and T. Pawlowski, “Space charge in XLPE near the electrode Interfaces,” in IEEE Conference on Electrical Insulation and Dielectric Phenomena (IEEE, 2006), pp. 69–72.

[45] D. Marty-Dessus, L. Berquez, A. Petre, M. Mousseigne, and J. L. Franceschi, “Three-dimensional cartography of space charge by FLIMM,” in Annual Report Conference on Electrical Insulation and Dielectric Phenomena (IEEE, 2002), pp. 602–605.

[46] C. Pham, A. Petre, L. Berquez, R. Flores-Suarez, A. Mellinger,W.Wirges, and R. Gerhard, "3D high-resolution mapping of polarization profiles in thin poly(vinylidenefluoride-trifluoroethylene) (PVDF-TrFE) films using two thermal techniques," IEEE Trans. Dielectr. Electr. Insul. 16(3), 676–681 (2009).

[47] T. T. Anh, L. Berquez, L. Boudou, and J. Martinez-Vega, "Space charge and induced mechanical deformation cartographies by FLIMM and digital image correlation on electron irradiated PTFE thin film," in 14th International Symposium on Electrets (ISE) (IEEE, 2011), pp. 39–40.

[48] T. T. Anh, L. Berquez, L. Boudou, and J. Martinez-Vega, "Effect of trapped space charge on mechanical deformation induced by electric field," IEEE Trans. Dielectr. Electr. Insul. 18(5), 1416–1422 (2011).

[49] D. Marty-Dessus, A. C. Ziani, A. Petre, and L. Berquez, "Space charge distributions in insulating polymers: A new non-contacting way of measurement," Rev. Sci. Instrum. 86(4), 043905 (2015).

[50] T. Takada, T. Maeno, H. Kushibe,"An Electric Stress-Pulse Technique for The Measurement of Charges in A Plastic Plate Irradiated by an Electron Beam," *Electrical Insulation, IEEE Transactions on*, vol.EI-22, no.4, pp.497-501, Aug. 1987.

[51] Y. Li, M. Yasuda, T. Takada,"Pulsed electroacoustic method for measurement of charge accumulation in solid dielectrics," *Dielectrics and Electrical Insulation, IEEE Transactions on*, vol.1, no.2, pp.188-195, Apr. 1994.

[52] K. Kumaoka, T. Kato, H. Miyake and Y. Tanaka, "Development of space charge measurement system with high positional resolution using pulsed electro acoustic method," Int'l. Sympos. Electr. Insulating Materials (ISEIM), pp. 389-392, 2014.

[53] H. Kitajima, Y. Tanaka and T. Takada, "Measurement of space charge distribution at high temperature using the pulsed electro-acoustic (PEA) method," 7th Int'l. Conf. Dielectric Materials, Measurements and Applications, Conf. Publ. No. 430, pp. 8-11, 1996.

[54] M. Wadamori, M. Fukuma, T. Maeno, K. Fukunaga, and M. Nagao, "Proposal of numerical analysis model of acoustic wave propagation and generation on PEA method", IEEE 7th Int'l. Conf. Propertiea Appl. Dielectr. Materials (ICPADM), pp. 863–866, 2003.

[55] S. Hóle, V. Griseri, L. A. Dissado, and J. C. Fothergill, "Improvement of PEA signal analysis using simulations for complex geometry samples,", J. Physica D., Vol. 35, pp. 19–24, 2002.

[56] S. Hóle, A. Sylvestre, and S. Rowe, "The influence of filler particles on space charge measurement," J. Phys. D, Vol. 37, pp. 1869–1876, 2004.

[57] S. Hóle, A. Sylvestre, O. Gallot-Lavallee, C. Guillermin, P. Rain, and S.Rowe, “Space charge distribution measurement methods and particle loaded insulating materials,” J. Phys. D, Vol. 39, pp. 950–956, 2006.

[58] Y. Imaizumi, K. Suzuki, Y. Tanaka and T. Takeda, "Three-dimensional space charge distribution measurement in solid dielectrics using pulsed electroacoustic.

[59] K. Fukunaga, "Innovative PEA space charge measurement systems for industrial applications," IEEE Electr. Insul. Mag., Vol. 20, No. 2, pp.18-26, 2004.

[60] T. Maeno, "Three-dimensional PEA charge measurement system," IEEE Trans. Dielectr. Electr. Insul., Vol. 8, No. 5, pp. 845-848, 2001.

[61] R. J. Fleming, "Space charge profile measurement techniques: recent advances and future directions," IEEE Trans. Dielectr. Electr. Insul., Vol.12, No.5, pp.967-978, Oct. 2005.

[62] H. Tanaka, K. Fukunaga, T. Maeno and Y. Ohki, "Three-dimensional Space Charge Distribution in Glass Fiber/Epoxy Composites," IEEE 8th Conf. Properties Applications Dielectr. Materials, pp.69-72, 2006.

[63] K. Fukunaga, T. Maeno, V. Griseri, K. Okamoto,"Three-dimensional space charge measurements of printed circuit boards," IEEE Conf. Electr. Insul. Dielectr. Phenomena, pp. 465-468, 2001.

[64] K. Okamoto, K. Fukunaga, T. Maeno, and T. Tsukui, “Observation of copper ionic migration in insulation layer by pulsed electroacoustic method,” IEEE Trans. CPMT, Vol. 25, No. 2, pp. 239–243, 2002.

[65] K. Fukunaga, T. Maeno, and K. Okamoto, “Three-dimensional space charge observation of ion migration in a metal-base printed circuit board,” IEEE Trans. Dielectr. Electr. Insul., Vol. 10, No. 3, pp. 458–462, 2003.

[66] M. Fukuma, T. Maeno, K. Fukunaga,"Cross-section space charge measurement system," IEEE Conf. Solid Dielectr., (ICSD), Vol.1, pp. 182-185, 2004.

[67] M. Fukuma, N. Masuda and K. Fukunaga, "Development of sensor scanning type space charge measurement system," IEEE Conf. Electr. Insul. Dielectr. Phenomena (CEIDP), 2010.

[68] M. Fukuma, K. Fukunaga, C. Laurent,"Packet-like space charge in polyethylene probed with a 2D-spatial resolution," *Electrical Insulation and Dielectric Phenomena, IEEE Conference on*, pp.748-751, Oct. 2006.

[69] S. Imai, Y. Tanaka, T. Fukao, T. Takada, T. Maeno, "Development of new PEA system using open upper electrode" *Electrical Insulation and Dielectric Phenomena, (CEIDP)2004 Annual Report Conference on*, pp.61-64, 17-20 Oct. 2004.

[70] C. Perrin, V. Griseri, C. Laurent,"Measurement of internal charge distribution in dielectrics using the pulsed electro-acoustic method in no contact mode," IEEE Trans. Dielectr. Electr. Insul., Vol. 15, No. 4, pp.958-964, 2008.

[71] V. Griseri, J. Riffaud, T. Maeno and L. Berquez, "Preliminary measurements on dielectric materials by the pulsed electro-acoustic method using a ring electrode," Int'l. Sympos. Electr. Insulating Materials (ISEIM), pp.112-115, 2014.

[72] J. Riffaud, V. Griseri and L. Berquez, "New design of the Pulsed Electro-Acoustic upper electrode for measurements under irradiation," IEEE Conf. Electr. Insul. Dielectr. Phenomena (CEIDP), pp. 614-617, 2014.

[73] T. Maeno, "Portable space charge measurement system using the pulsed electrostatic method," IEEE Trans. Dielectr. Electr. Insul., Vol.10, No.2, pp.331-335, 2003.

[74] K. Fukunaga, "Progress and Prospects in PEA Space Charge Measurement Techniques," IEEE Electr. Insul. Mag., Vol. 24, No. 3, pp.26-37, 2008.

[75] K. Fukunaga, H. Miyata, M. Sugimori, T. Takada, "Measurement of Charge Distribution in the Insulation of Cables using Pulsed Electroacoustic Method", *Trans.IEE japan,* Vol. 110-A, No. 9, pp. 647-648, 1990.

[76] N. Hozumi, T. Okamoto and T. Imajo, "Space charge distribution measurement in a long size XLPE cable using the pulsed electroacoustic method," IEEE Int'l. Sympos. Electr. Insul., pp. 294-297, 1992.

[77] N. Hozumi, T. Takeda, H. Suzuki and T. Okamoto, "Space charge behavior in XLPE cable insulation under 0.2-1.2 MV/cm dc fields," IEEE Trans. Dielectr. Electr. Insul., Vol. 5, No. 1, pp. 82-90, 1998.

[78] M. Fu, G. Chen, A.E. Davies, J.G. Head,"Space charge measurements in power cables using a modified PEA system," *Dielectric Materials, Measurements and Applications, 2000. Eighth International Conference on (IEE Conf. Publ. No. 473),* pp.74-79, 2000

[79] M. Fu, G. Chen, A.E. Davies, Y. Tanaka, T. Takada,"A modified PEA space charge measuring system for power cables," *Properties and Applications of Dielectric Materials, Proceedings of the 6th International Conference on,* vol.1, pp.104-107, 2000

[80] M. Fu, G. Chen, A.E. Davies, J. Head,"Space charge measurements in cables using the PEA method:-signal data processing considerations," *Solid Dielectrics, (ICSD), Proceedings of the 2001 IEEE 7th International Conference on,* pp.219-222, 2001

[81] M. Fu, G. Chen,"Space charge measurement in polymer insulated power cables using flat ground electrode PEA system," *Science, Measurement and Technology, IEE Proceedings* , vol.150, no.2, pp.89-96, March 2003.

[82] T. Takeda, N. Hozumi, H. Suzuki, K. Fujii, K. Terashima, M. Hara, Y. Mutrata, K. Wantanabe and M. Yoshida, "Space charge behavior in fullsize 250 kV DC XLPE cables," IEEE Trans. Power Delivery, Vol.13, No.1, pp.28-39, 1998.

[83] A. R. A. Raja, B. Vissouvanadin, T. T. N. Vu, G. Teyssedre and N. I. Sinisuka, “Space Charge Measurement on XLPE Cable for HVDC Transmission using PEA Method”, Procedia Technology, Vol. 11, pp. 327-333, 2013.

[84] X. Wang, D. Tu, Y. Tanaka, T. Muronaka, T. Takada, C. Shinoda and T. Hashizumi, "Space charge in XLPE power cable under dc electrical stress and heat treatment," IEEE Trans. Dielectr. Electr. Insul., Vol. 2, No.3, pp.467-474, 1995.

[85] I. A. Tsekmes, D. van der Born, P. H. F. Morshuis, J. J. Smit, T. J. Person and S. J. Sutton, "Space charge accumulation in polymeric DC minicables," IEEE Int’l. Conf. Solid Dielectrics (ICSD), pp. 452-455, 2013.

[86] W.Le, D. Fabiani, G. C. Montanari and U. H. Nilsson, "Study of the space charge measurement results on two kinds of extruded XLPE minicables," IEEE Int’l. 9th Conf. Properties and Applications of Dielectr. Materials, (ICPADM), pp.918-921, 2009.

[87] D. Van Der Born, , I. A. Tsekmes; T. J. Person, S. J. Sutton, P. H. F. Morshuis and J. J. Smit, "Evaluation of space charge accumulation processes in small size polymeric cable models," IEEE Conf. Electr. Insul. Dielectr. Phenomena (CEIDP), pp. 669-672, 2012.

[88] H. Zheng, S. J. Dodd, L. A. Dissado, J. C. Fothergill, A. Allais and L. Kebbabi, "Feasibility of using a flat bottom electrode for PEA space charge measurement on mini-cables under high temperatures," IEEE Conf. Electr. Insul. Dielectr. Phenomena (CEIDP), pp.1109-1112, 2013.

[89] G. C. Montanari, L. A. Dissado and S. Serra, "The hidden threat to HVDC polymeric insulation at design field: Solitonic conduction," IEEE Electr. Insul. Mag., Vol. 30, No. 4, pp. 39-50, 2014.

[90] G. C. Montanari, D. Fabiani and L. A. Dissado, "Fast charge pulses: The evidence and its interpretation," IEEE Conf. Solid Dielectrics (ICSD), pp.10-14, 2013.

[91] D. Fabiani, G. C. Montanari and L. A. Dissado, "Measuring a possible HVDC insulation killer: fast charge pulses," IEEE Trans. Dielectr. Electr. Insul., Vol. 22, No.1, pp.45-51, 2015.

[92] P. Laurenceau, J. Ball, G. Dreyfus, and J. Lewiner, “Une nouvelle method de détermination de la distribution spatiale des potentiels dans les diélectriques”. C. R. Acad. Sci. Ser. B 283, pp. 135-138, 1976.

[93] F. Chapeau, C. Alquie, J. Lewiner, H. Auclair, Y. Pelet and R. Jocteur, "The Pressure wave Propagation Metod for the Analysis of Insulating Materials: Application to LDPE Used in HV Cables," IEEE Trans.. Electr. Insul., Vol. 21, No. 3, pp. 405-410, 1986.

[94] S. Mahdavi, Y. Zhang, C. Alquie and J. Lewiner, "Determination of space charge distributions in polyethylene samples submitted to 120 kV DC voltage," IEEE Trans. Electr. Insul., Vol. 26, No. 1, pp.57-62, 1991.

[95] S. Mahdavi, C. Alquie and J. Lewiner, "Measurement of charge distributions in coaxial structures-application to high voltage cables," IEEE Conf. Electr. Insul. Dielectr. Phenomena, pp. 296-302, 1989.

[96] W. Eisenmenger and M. Haardt, “Observation of charge compensated zones in polyvinylidenefluoride (PVDF) films by piezoelectric acoustic step-wave response,” Solid State Commun., Vol. 41, pp. 917–920, 1982.

[97] M. Haardt and W. Eisenmenger, “High resolution technique for measuring charge and polarization distributions in dielectrics by piezoelectrically induced pressure step waves (PPS)”, IEEE Conf. Electr. Insul. Dielectr. Phenomena, pp. 46–51, 1982.

[98] R. Gerhard-Multhaupt, G. M. Sessler, J. E. West, K. Holdik, M. Haardt, and W. Eisenmenger, “Investigation of piezoelectricity distributions in poly(vinylidene fluoride) by means of quartz or laser generated pressure pulses,” J. Appl. Phys., Vol. 55, pp. 2769–2775, 1984.

[99] G. M. Sessler, J. E. West, and R. Gerhard-Multhaupt, “Measurement of charge distribution in polymer electrets by a new pressure-pulse method,” Polym. Bull., Vol. 6, pp. 109–111, 1981.

[100] T. Takada, "Acoustic and optical methods for measuring electric charge distributions in dielectrics," IEEE Trans. Dielectr. Electr. Insul., Vol. 6, No. 5, pp.519-547, Oct. 1999.

[101] L. Cheng, L. Zhong, Y. Zhang, S. Tan and J. Chen, "A Piezo-PWP method for charge measurement of the cell suspension," IEEE Int’l. Conf. Properties and Applications of Dielectr. Materials (ICPADM), pp. 907-910, 2009.

[102] Y. Tian, G. Chen, A. E. Davies,"Development of a three dimensional space charge measurement system for dielectrics using PWP method," IEEE Conf. Electr. Insul. Dielectr. Phenomena, pp.644-647, 2002.

[103] T. Takada, H. Miyake and Y. Tanaka, "Pulse Acoustic Technology for Measurement of Charge Distribution in Dielectric Materials for Spacecraft," IEEE Trans. Plasma Sci., Vol. 34, No.5, pp. 2176-2184, 2006.

[104] G. M. Sessler, R. Gerhard-Multhaupt, H. Seggern and J. E. West, “Charge and Polarization Profiles in Polymer Electrets”, IEEE Trans. Electr. Insul., Vol. 21, No. 3, pp. 411-415, 1986.

[105] G. M. Sessler, ”Charge Storage in Dielectrics”, IEEE. Trans. Electr. Insul., Vol. 24, No. 3, pp. 395-402,1989.

[106] L. Tingji and G. M. Sessler, “An Experimental Study of Charge Distribution in Electron Beam Irradiated Polypropylene Films”, IEEE Trans. Electr. Insul., Vol. 26, No. 2, pp. 228-235, 1991.

[107] G. M. Sessler, R. Gerhard-Multhaupt, J. E. West and H. Seggern, “Optoacoustic Generation and Electrical detection of Subnanosecond Acoustic Pulses”, J. Appl. Phys., Vol. 58, No. 1, pp. 119-121,1985.

[108] K. R. Bambery and R. J. Fleming, "Space charge accumulation in two power cable grades of XLPE," IEEE Trans. Dielectr. Electr. Insul., Vol. 5, No. 1, pp.103-109, 1998.

[109] S. HoIé, "Recent developments in the pressure wave propagation method," IEEE Electr. Insul. Mag., Vol. 25, No. 3, pp.7-20, 2009.

[110] H. Tran Van, J. L. Auge and P. Rain, "Study of the generation of the pressure pulse in the laser induced pressure pulse method: Optimization of the process," IEEE 10th Int’l. Conf. Solid Dielectrics (ICSD), pp.1-4, 2010.

[111] J. E. West and G. M. Sessler, "Charge distribution in electron-beam irradiation polymers," IEEE 7th Int’l. Sympos. Electrets (ISE 7) (Cat. No.91CH3029-6), Berlin, Germany, pp. 371-376, 1991.

[112] G. M. Sessler, "Charge dynamics in irradiated polymers," IEEE Trans. Electr. Insul., Vol. 27, No. 5, pp. 961-973, 1992.

[113] P. Blob, M. Steffen, H. Schäfer, G. M. Yang and G. M. Sessler, “A comparison of space-charge distributions in electron-beam irradiated FEP obtained by using heat-wave and pressure-pulse techniques” J. Appl. Phys., Vol. 30, pp. 1668–1675, 1997.

[114] A. Ustundag, T. J. Gung and M. Zahn, "Kerr electro-optic theory and measurements of electric fields with magnitude and direction varying along the light path," IEEE Trans. Dielectr. Electr. Insul., Vol. 5, No. 3, pp. 421-442, 1998.

[115] A. Ustundag and M. Zahn, "Finite element based Kerr electro-optic reconstruction of space charge," IEEE Trans. Dielectr. Electr. Insul., Vol.8, No. 4, pp. 612-628, 2001.

[116] K. Kato, T. Nara, H. Okubo, F. Endo, A. Yamazaki, H. Koide, Y. Hatta and T. Hikosaka, "Space charge behavior in palm oil fatty acid ester (PFAE) by electro-optic field measurement," IEEE Trans. Dielectr. Electr. Insul., Vol. 16, No. 6, pp. 1566-1573, 2009.

[117] H. Saito, T. Urabe, Y. Tanaka, T. Takada, Y. Murooka and N. Tomita,"Monitoring system for high energy cosmic ray observation in space environment using advanced electro-optic Pockels techniques," IEEE Conf. Electr. Insul. Dielectr. Phenomena, Vol. 2, pp. 694-697, 2000.

[118] Y. Tanaka, Y. Usui, K. Umemura, T. Takada, R. Watanabe and N. Tomita,"Optical measurement techniques for surface and bulk charge distribution," IEEE Conf. Solid Dielectr. (ICSD), Vol. 2, pp. 959-962, 2004.

[119] F. Long, J. Zhang, C. Xie and Z. Yuan, "Application of the Pokels Effect to High Voltage Measurement," Int'l. 8th Electronic Measurement and Instruments, (ICEMI), pp. 4-495,4-499, 2007.

[120] F. Cecelja, M. Bordovsky and W. Balachandran, "Electro-optic sensor for measurement of DC fields in the presence of space charge," IEEE 17th Conf, Instrumentation Measurement Technology (IMTC), Vol. 1, pp. 74-78, 2000.

[121] Z. Gao, Z. Yu, R. Zeng, F. Tian, J. Yu, M. Dai, B. Niu, M. Li, L. Liu, R. Li and Y. Liao, "Research on measuring methods and sensors of high voltage DC electric field," Int'l. Conf. Information Science, Electronics and Electr. Eng. (ISEEE), Vol.2, pp.850-854, April 2014.

[122] R. Bodega, P. H. F. Morshuis and J. J. Smit, "Space charge measurements on multi-dielectrics by means of the pulsed electroacoustic method," in *IEEE Transactions on Dielectrics and Electrical Insulation*, vol. 13, no. 2, pp. 272-281, April 2006.

[123] M. J. P. Jeroense, "Charges and discharges in hvdc cables," Ph.D. dissertation, Delft University of Technology, 1997.

[124] J. S. Chahal and C. C. Reddy, "Modeling and Simulation of Pulsed Electroacoustic Measurement Method," in *IEEE Systems Journal*, vol. 8, no. 4, pp. 1283-1292, Dec. 2014.

[125] B. Bauer, "Equivalent circuit analysis of mechano. Acoustic structures," in *Transactions of the IRE Professional Group on Audio*, vol. AU-2, no. 4, pp. 112-120, July-August 1954.

[126] P. Kundur, "Power system stability and control", Mc Graw-Hill, 2004

[127] F. Viola, P. Romano and R. Miceli, "Finite-Difference Time-Domain Simulation of Towers Cascade Under Lightning Surge Conditions," in *IEEE Transactions on Industry Applications*, vol. 51, no. 6, pp. 4917-4923, Nov.-Dec. 2015.

[128] http://www.ece.utah.edu/~ece6340/LECTURES/lecture%2014/FDTD.pdf, "The Finite-Difference Time- Domain Method (FDTD)".

[129] Felipe Faria Da Silva, Claus Leth Bak,"Electromagnetic Transients in Power Cables", Power Systems, Springer-Verlag London 2013

[130] http://www.fast.u-psud.fr/~martin/acoustique/support/r%C3%A9flection r%C3%A9 fraction pdf, “Reflection and transmission of ultrasonic waves”.

[131] J. van Deventer, T. Lofqvist and J. Delsing, "PSpice simulation of ultrasonic systems," in *IEEE Transactions on Ultrasonics, Ferroelectrics, and Frequency Control*, vol. 47, no. 4, pp. 1014-1024, July 2000.

[132] R. S. Dahiya, M. Valle and L. Lorenzelli, "SPICE model for lossy piezoelectric polymers," in *IEEE Transactions on Ultrasonics, Ferroelectrics, and Frequency Control*, vol. 56, no. 2, pp. 387-395, February 2009.

[133] F. H. Kreuger, “*Industrial high DC voltage*”, Delft University Press, The Netherlands,1995.

[134] R. Bodega, P. H. F. Morshuis and J. J. Smit, "Electrostatic force distribution in a multi-layer dielectric tested by means of the PEA method," *Proceedings of the 2004 IEEE International Conference on Solid Dielectrics, 2004. ICSD 2004.* 2004, pp. 264-267 Vol.1.

Acknowledgement

First of all I would like to express my gratitude to my supervisor Prof. Pietro Romano. Despite his enormous family and work commitments, he has been always available to help me not only for difficulties related to the research activity, but also for personal problems. I will never forget what he did for me. He has always believed in me, and thanks to him this PhD work has been completed.

I would also like to thank my further supervisor Prof. Eleonora Riva Sanseverino. She has been always patient in helping me, in particular for the corrections of all of the works that I made in my PhD activity, including the revision of this thesis. She has been always very enthusiastic when I showed her all of my works, and thanks to this, she gave me the charge to always do better.

I am thankful to Prof. Fabio Viola for his guidance and training in the use of Matlab software. I thank him for providing me the basic code for the development of the PEA cell model.

Many thanks to my colleague and friend Massimo Caruso, for everything. In particular, for his English support. Thanks to him, my oral presentation at the CEIDP conference in Toronto was full of satisfactions.

A particular gratitude for Prof. George Chen who offered me the opportunity to study at the University of Southampton. Many thanks for his spontaneous guidance and encouragements in this work. Thanks to his knowledge, has contributed greatly to the realization of this thesis. He gave me the passion for the topic treated in this work, in particular, he gave me the inspiration for the developed of the PEA cell model. He was always excited when I showed him the simulation results, I will never forget his happiness when we realized good performance of the developed model.

My sincere thanks to all of the TDHVL researchers, in particular Bo Huang, Zhiqiang Xu, Miao Hao, Churui Zhou and my brother Yunpeng Zhan (Chris). When I arrived at Southampton, each of them treated me like a friend. Thanks to their hospitality, the experience in Southampton has been something special. I enjoyed their company very much and their original Chinese humor and sympathy.

I also like to thank Prof. Naohiro Hozumi and Shosuke Morita from the University of Tecnology, Japan. Thanks to them I had the possibility, for the first time, to carry out measurements of space charge in cable specimens.

Many thanks to Prof. Sombel Diaham and Prof. Jerome Castellon for the beautiful days spent together during the CEDIP conferences.

My special thanks go to Prysmian Group for the financial support of this work. In particular, Ing. Marcelo Andrade, Ing. Roberto Candela, Ing. Luca De Rai, Ing. Stefano Franchi and Ing. Ivan Troia. I thank all of them for giving me this fantastic opportunity.

Thank you so much to my special friends Vincenzo and Giuseppe for the beautiful moments that we spent together, for their moral support and for everything else.

Many thanks to my extraordinary family for sticking by me all these years. My father Nino, my mom Grace, my sister Chiara, my brother in law Francesco, my brother Don Alessandro, my little goddaughter Sofia, my grandmothers Margherita and Chiara, my grandfathers Tony and Nino, my godfather Gaetano, my aunt Mariella and my godsons Baldo and Nino.

Finally, the most important gratitude for my girlfriend Chiara. She stayed near me throughout the PhD period, enduring my absence for a lot of times. I apologize for the time that I did not dedicate to her, and I thank her for understanding me. As well as, I would like to thank her parents Pino and Margherita, for the organization of the trips and for everything else.

Pietro Romano and Antonino Imburgia during the CEIDP conference at Toronto.

Prof. Giovanni Mazzanti, Antonino Imburgia, Prof. Peter Morshuis, Prof. Tatsuo Takada (the inventor of the PEA technique) and Prof. Pietro Romano.

Prof. George Chen and its research team.

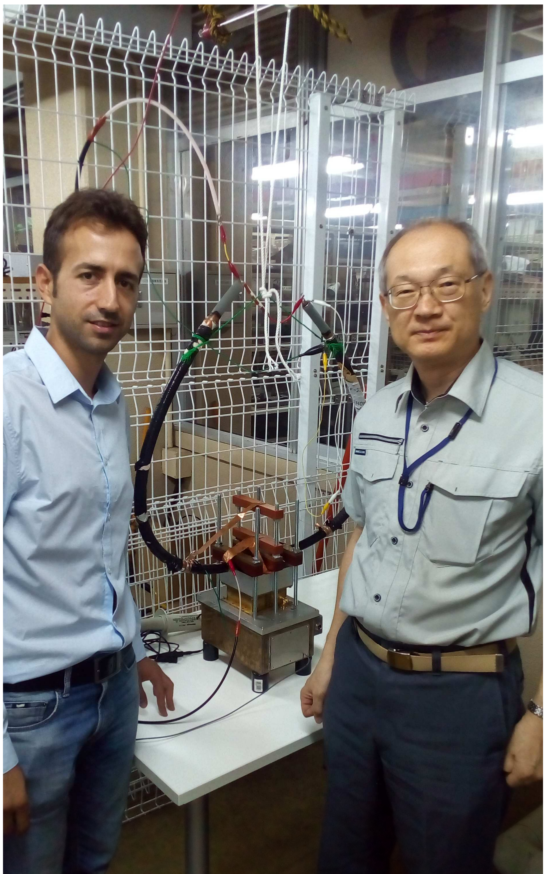

Prof. Naohiro Hozumi, Antonino Imburgia and a PEA system for mini-cables. University of Technology, Toyohashi, Japan.

The PEA system for full-size cable. Prysmian Group, Milan.